

ALMA MATER STUDIORUM · UNIVERSITÀ DI BOLOGNA

---

SCUOLA DI SCIENZE

Corso di Laurea Magistrale in Fisica Applicata

**The effect of diffusion gradient  
direction number  
on tractography of corticospinal tract  
in human brain:  
an along-tract analysis**

**Relatore:**  
Dott.ssa  
CLAUDIA TESTA

**Presentata da:**  
MARIAGRAZIA POPEO

**Correlatore:**  
Prof.ssa  
PAOLA FANTAZZINI

**Sessione I**  
**Anno Accademico 2015-2016**



# Abstract

Nel presente lavoro di tesi ho sviluppato un metodo di analisi di dati di DW-MRI (Diffusion-Weighted Magnetic Resonance Imaging) cerebrale, tramite un algoritmo di trattografia, per la ricostruzione del tratto corticospinale, in un campione di 25 volontari sani. Il diffusion tensor imaging (DTI) sfrutta la capacità del tensore di diffusione  $D$  di misurare il processo di diffusione dell'acqua, per stimare quantitativamente l'anisotropia dei tessuti. In particolare, nella sostanza bianca cerebrale la diffusione delle molecole di acqua è direzionata preferenzialmente lungo le fibre, mentre ostacolata perpendicolarmente ad esse. La trattografia utilizza le informazioni ottenute tramite il DW imaging per fornire una misura della connettività strutturale fra diverse regioni del cervello. Nel lavoro si è concentrata l'attenzione sul fascio corticospinale, che è coinvolto nella motricità volontaria, trasmettendo gli impulsi dalla corteccia motoria ai motoneuroni del midollo spinale. Il lavoro si è articolato in 3 fasi. Nella prima ho sviluppato il pre-processing di immagini DW acquisite con un gradiente di diffusione sia a 25 che a 64 direzioni in ognuno dei 25 volontari sani. Si è messo a punto un metodo originale ed innovativo, basato su "Regions of Interest" (ROIs), ottenute attraverso la segmentazione automatizzata della sostanza grigia e ROIs definite manualmente su un template comune a tutti i soggetti in esame. Per ricostruire il fascio si è usato un algoritmo di trattografia probabilistica che stima la direzione più probabile delle fibre e, con un numero elevato di direzioni del gradiente, riesce ad individuare, se presente, più di una direzione dominante (seconda fibra). Nella seconda parte del lavoro, ciascun fascio è stato suddiviso in 100 segmenti (percentili). Sono stati stimati anisotropia frazionaria (FA), diffusività media, probabilità di connettività, volume del fascio e della seconda fibra con un'analisi quantitativa "along-tract", per ottenere un confronto accurato dei rispettivi percentili dei fasci nei diversi soggetti. Nella terza parte dello studio è stato fatto il confronto dei dati ottenuti a 25 e 64 direzioni del gradiente ed il confronto del fascio fra entrambi i lati. Dall'analisi statistica dei dati inter-subject e intra-subject è emersa un'elevata variabilità tra soggetti, dimostrando l'importanza di parametrizzare il tratto.

I risultati ottenuti confermano che il metodo di analisi trattografica del fascio corticospinale messo a punto è risultato affidabile e riproducibile. Inoltre, è risultato che un'acquisizione con 25 direzioni di DTI, meglio tollerata dal paziente per la minore durata dello scan, assicura risultati attendibili. La principale applicazione clinica riguarda patologie neurodegenerative con sintomi motori sia acquisite, quali sindromi parkinsoniane sia su base genetica o la valutazione di masse endocraniche, per la definizione del grado di contiguità del fascio. Infine, sono state poste le basi per la standardizzazione dell'analisi quantitativa di altri fasci di interesse in ambito clinico o di studi di ricerca fisiopatogenetica.



# Contents

|  |           |
|--|-----------|
| <b>Introduction</b>  | <b>1</b>  |
| <b>1 Diffusion Tensor Imaging and Tractography</b>                           | <b>3</b>  |
| 1.1 Diffusion . . . . .  | 3         |
| 1.1.1 Hindered and Apparent Diffusion Coefficients . . . . .                 | 4         |
| 1.1.2 Water diffusion in neural tissue . . . . .                             | 6         |
| 1.2 Diffusion MRI . . . . .  | 8         |
| 1.2.1 Spin-Echo Sequence . . . . .   | 8         |
| 1.2.2 Magnetic field gradients . . . . .                                     | 9         |
| 1.2.3 Pulsed Gradient Spin-echo sequence and diffusion-weighted MR . . . . . | 9         |
| 1.3 Diffusion Tensor Imaging . . . . .                                       | 11        |
| 1.3.1 Parameters derived from the diffusion tensor . . . . .                 | 13        |
| 1.3.2 Number of diffusion gradient directions . . . . .                      | 15        |
| 1.4 Tractography . . . . .   | 16        |
| 1.4.1 Deterministic tractography . . . . .                                   | 17        |
| 1.4.2 Probabilistic tractography . . . . .                                   | 20        |
| 1.4.3 Application and future directions . . . . .                            | 24        |
| <b>2 Corticospinal Tract</b>   | <b>25</b> |
| 2.1 The motor cortex . . . . .   | 25        |
| 2.2 Anatomy of the corticospinal tract . . . . .                             | 27        |
| <b>3 Materials and methods</b>   | <b>29</b> |
| 3.1 Participants . . . . .   | 29        |
| 3.2 Data acquisition . . . . .   | 31        |
| 3.3 Data preprocessing . . . . .   | 32        |

|          |  |           |
|----------|--|-----------|
| 3.4      | Tractography of corticospinal tract . . . . .                      | 35        |
| 3.4.1    | State of art . . . . .   | 36        |
| 3.4.2    | Tract drawing: PROBTRACKX algorithm . . . . .                      | 37        |
| 3.4.3    | ROIs definition and tracking the CST . . . . .                     | 39        |
| 3.5      | Data analysis . . . . .  | 46        |
| 3.5.1    | State of art . . . . .   | 46        |
| 3.5.2    | Parameterization . . . . .   | 49        |
| 3.5.3    | Statistical analysis . . . . .                                     | 53        |
| <b>4</b> | <b>Results</b>   | <b>57</b> |
| 4.1      | CST reconstruction . . . . .                                       | 57        |
| 4.2      | Statistical analysis . . . . .                                     | 57        |
| 4.2.1    | Intrasubject and intersubject variability . . . . .                | 67        |
| 4.2.2    | Side and number of diffusion gradient directions effects . . . . . | 68        |
| 4.2.3    | Along-tract analysis . . . . .                                     | 72        |
| 4.2.4    | Spatial distribution of the tract . . . . .                        | 73        |
| 4.2.5    | Crossing fibers analysis . . . . .                                 | 73        |
| <b>5</b> | <b>Discussion</b>  | <b>89</b> |
|          | <b>Conclusions</b>   | <b>95</b> |
|          | <b>Bibliography</b>  | <b>97</b> |

# Introduction

Diffusion Weighted Imaging (DWI) is a magnetic resonance imaging (MRI) method that allows an in vivo and non-invasively description of the diffusion process of molecules in biological tissues. This is based on the evidence that, during their random diffusion-driven displacements, molecules probe tissue structure at a microscopic scale. Brain water diffusion is a three-dimensional phenomenon and it is not free, but reflects interactions with many obstacles, like macromolecules, fibers or membranes: molecular mobility in tissues may be anisotropic, as in brain white matter. Diffusion anisotropy in white matter is due to its specific organization in bundles of axonal fibers which run in parallel: diffusion in the direction of fibers results faster than in perpendicular direction and the direction of the fastest diffusion indicates the overall orientation of the fibers. DWI uses diffusion-encoding gradients, applied in different directions, to estimate the diffusion tensor and measurements of diffusion parameters. The use of more than six directions (required as minimum) can provides better estimation of diffusion indices as fractional anisotropy (FA) and mean diffusivity (MD).

The process of using DWI data to estimate white matter fibers bundles is commonly known as tractography. MRI tractography is a unique imaging technique that identifies and measures these pathway in vivo; the study of the boundles is essential to our understanding of function of brain regions in normal and pathological brain and permits to trace maps of brain connectivity. In order to reconstruct fiber bundles, tractography procedure aims to find paths through the data field along which diffusion is least hindered. Strategies for achieving this goal vary greatly depending on the used algorithm. The present work adopts the probabilistic tractography algorithm, that estimates at each voxel the most likely fiber orientations. The traced connections represent a measure of the probability and form a connectivity map. The great advantage of probabilistic algorithm is the ability to identify, if present, more than one dominant direction in each voxel also with standard DWI acquisitions. This allows to reconstruct the tract of interest in

a detailed way.

The present thesis work deals with the analysis of DWI data and tractographic reconstruction, obtained at 25 and 64 directions of diffusion gradient, of 25 healthy subjects. Data were acquired at RM Functional Unit at DIBINEM (Department of Biological and Neuromotor Sciences) in Policlinico S.Orsola. The aim of the project is to develop a reliable along-tract procedure to reconstruct the corticospinal tract using a probabilistic algorithm and to investigate the distribution of the most important diffusion parameters in order to realize a comparison between data obtained with different number of diffusion gradient directions. It is important to specify that the corticospinal tract (CST) is one of the most important tract in the central nervous system and it is responsible for various motor functions for voluntary movements. Its description can have an important role in many neurodegenerative disorders.

A reproducible method to parameterize each delineated tract has been developed, by dividing each tract into 100 equal segments (percentiles). In this way, it is possible to obtain values of diffusion parameters in each percentile and to conduct spatial-specific precise comparisons between different subjects. Diffusion parameters value were investigated in dependence of side of brain and the number of diffusion gradient directions. This thesis is organized as follows. The first chapter introduces the physical basis of diffusion and DTI, to explain how tissue anisotropy can be evaluated. The tractography method is presented, examining the difference between probabilistic and deterministic algorithms. The second chapter reports a brief overview of the anatomy and structure of the corticospinal tract, the white matter bundle of interest. In the third chapter the method of reconstruction of the tract, its parameterization and the statistical analyses are described. Results are reported in the fourth chapter and discussed in the fifth. Finally, our conclusions and future research developments are outlined in the sixth chapter.

# Chapter 1

## Diffusion Tensor Imaging and Tractography

### 1.1 Diffusion

Diffusion is a spontaneous phenomenon in any fluid characterized by a temperature greater than absolute zero (0 Kelvin). Molecules are constantly moving with a random direction, that changes regularly as molecules collide with one another. This phenomenon, known as "Brownian motion", was first described in 1828 by Robert Brown, a botanist working on the mechanism of fertilization in flowering plants, who noticed the perpetual motion of pollen grains suspended in water. Diffusion can be considered the macroscopically observable effect of the microscopic Brownian motion of particles. The physical law that explains this process is called Fick's first law [1] and relates the diffusive flux to any molecular concentration difference through the relation:

$$\mathbf{J} = -D\nabla C \quad (1.1)$$

where  $\mathbf{J}$  is the net particle flux ( $\text{mol}/m^2 s$ ),  $C$  is the particle concentration ( $\text{mol}/m^3$ ), and  $D$  is the diffusion coefficient (or *diffusivity*,  $m^2/s$ ). The minus sign in (1.1) embodies the notion that particles move from regions of high concentration to regions of low concentration. The rate of this flux is proportional to the concentration gradient and to the diffusion coefficient. Unlike the flux vector or the concentration gradient, the diffusion coefficient is an intrinsic property of the medium, and its value is determined by the size of the diffusing molecules, the temperature and microstructural features of

the environment. Diffusion is a thermally driven process and the trajectory of each water molecule, at temperatures above zero degrees kelvin, can be described by a *random walk*: the molecule stays in a particular place for a fixed time  $t$  before moving to a random, new location in space. Considering every molecule, a random path can be drawn out in three-dimensional space. It is possible to study the behaviour of a large number of water molecules introducing a probabilistic framework. In 1905 Einstein considered  $\langle r^2 \rangle$  ( $m^2$ ), which represents the squared displacement of molecules from their starting point over a time  $t$ , averaged over all the molecules in the sample. Supposing that the number of molecules is sufficiently large and that they are free to diffuse, Einstein proved that  $\langle r^2 \rangle$  is directly proportional to observation time,  $t$ . The relationship is known as "Einstein's equation":

$$\langle r^2 \rangle = 6Dt \quad (1.2)$$

The distribution of squared displacements takes a Gaussian form, with the peak at zero displacement. The probability of walk through a given distance from the origin is the same, irrespective of direction in which it is measured. For a cube of water at body temperature the diffusion coefficient for water is  $3 * 10^{-3} \text{mm}^2 \text{s}^{-1}$  [2].

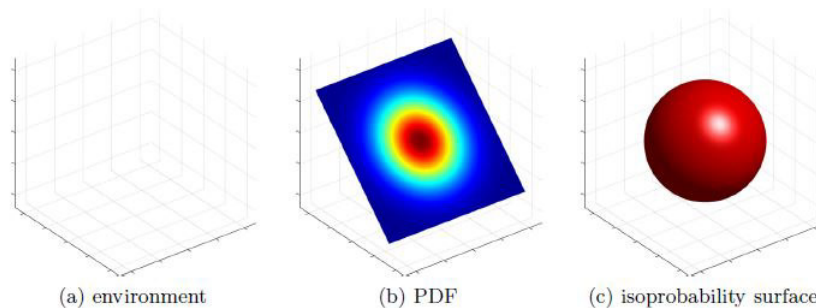


Figure 1.1: Free isotropic diffusion in a general environment. The panel (b) represents the probability density function (PDF). The image is taken by Jeurissen [3].

### 1.1.1 Hindered and Apparent Diffusion Coefficients

If the diffusing water molecules encounter any hindrances along their random walk (i.e. cell membranes and macromolecules), the mean squared displacement per unit time will be lower than when observed in "free" water. Thus, diffusion coefficient, obtained

with equation (1.2), will appear lower. Therefore, the diffusion coefficient that we measure in a biological sample, is usually referred to the *apparent diffusion coefficient* (ADC). This is an important property of diffusion to obtain information about the structural features of biological tissues.

Unordered tissue microstructure gives rise to isotropic diffusion, in which ADC is the same in every direction it is measured. This kind of diffusion can be described using a single ADC. The Gaussian distribution has a spherical isoprobability surface.

On the other hand, well ordered hindrances may induce the diffusion to become anisotropic: the ADC becomes dependent on the orientation in which it was measured. In this case, water molecules diffuse more freely parallel to the hindrances, than perpendicular to them. The diffusion can not be described with a single diffusion coefficient. For a single bundle (that is made up of a great number of tightly packed fibers), Gaussian distribution has an ellipsoidal isoprobability surface.

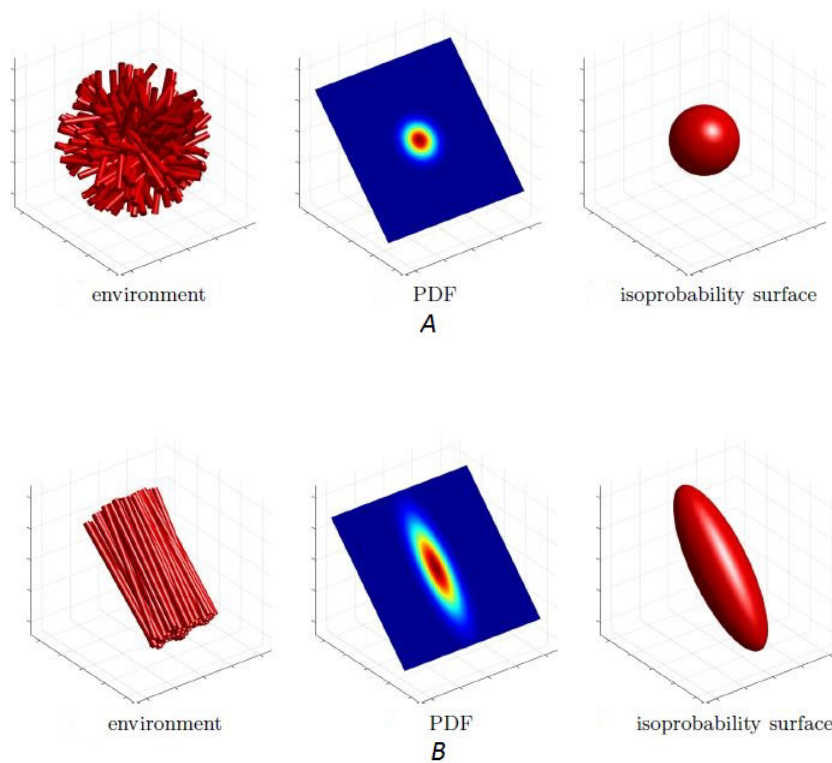


Figure 1.2: Hindered, isotropic (A) and anisotropic diffusion (B). Images are taken from Jeurissen [3].

### 1.1.2 Water diffusion in neural tissue

At a microscopic level, the neural tissue of brain is composed of neurons. A neuron is an electrically excitable cell that processes and transmits information through electrical and chemical signals. A typical neuron is mainly constituted by a cell body (or soma), dendrites (that extend in great number from the soma) and axon (see Figure 1.3). The soma and dendrites receive chemical signals from other neurons and process the information that is transmitted toward other nerve cells by the axons. These are surrounded several times by an insulating lipid-rich myelin sheath, that wraps around the axon to form a sort of capsules known as internode. Internodes are separated from each other by small amyelinated regions, called node of Ranvier. This organization of myelin sheaths allows a saltatory way of conduction whereby electrical impulses jump from node to node as they pass along the axon.

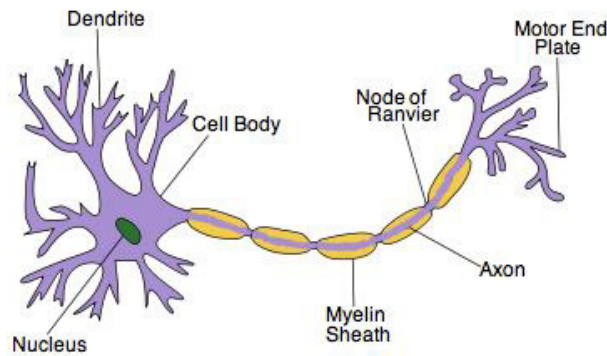


Figure 1.3: Schematic representation of a typical neuron.

At the macroscopic level, the brain can be characterized by four major components: grey matter (GM), white matter (WM), cerebrospinal fluid (CSF) and blood (see Figure 1.4). GM is mainly composed of neuronal cell bodies and unmyelinated axons. In the grey matter the glial cells and capillaries are also found. On the other hand, WM is made up of long-range myelinated axons and very few neuronal cell bodies; it is found hidden in the inner layer of brain's cortex, while the grey matter is mainly located on surface of the cerebral hemispheres (or cerebral cortex). Apart from myelin, that is responsible of the white color of WM visible in post-mortem dissections, axons contain an axonale membrane, neurofilaments and microtubules, all oriented along the same direction that

is the major axis of the axon (see Figure 1.5). Moreover, axons are organized and tightly packed together into nerve bundles. For all these reasons, water diffusion in many regions of the white matter is highly anisotropic; in particular, diffusion is less restricted parallel to the axon bundles than perpendicular to it. In this way, we can obtain important information about the structure, dimension and preferential orientation of WM fiber bundles.

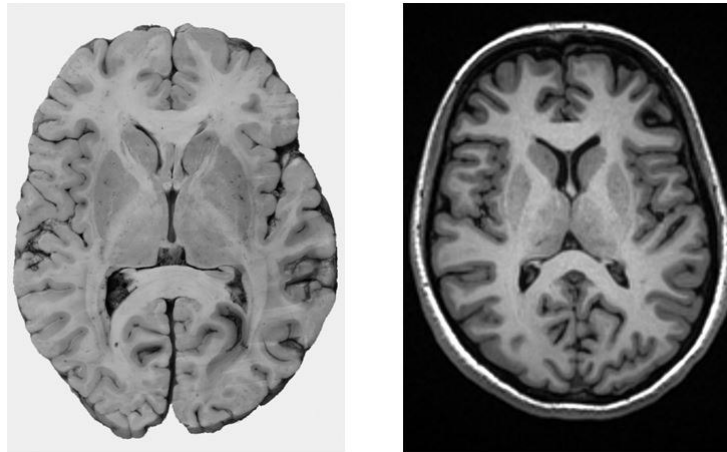


Figure 1.4: Formalin fixed 10-mm-thick brain slice from a male subject [34] (on the left) and axial MR image obtained with a spin-echo sequence (on the right): grey and white matter can be discerned.

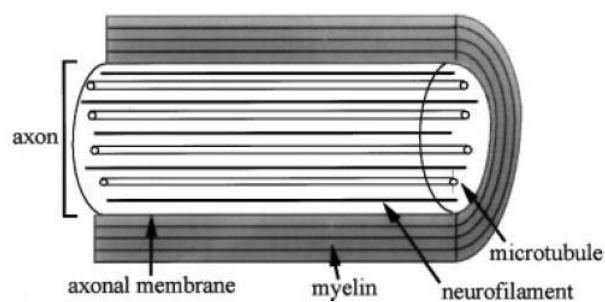


Figure 1.5: Schematic representation of a single axon, surrounded by myelin and axonal membrane.

## 1.2 Diffusion MRI

MRI is an imaging technique that detects proton signals from water molecules. Images thus reflect water density and properties as a function of position in space and allow the study of anatomy *in vivo* [4]. MRI works perturbing with electromagnetic waves the magnetization of water hydrogen nuclei induced in a strong and homogenous magnetic field. Water magnetization returns to the equilibrium state with a speed that is influenced by the nature of the biological tissues. This property, called the relaxation time, is the basis for the contrast of anatomical MRI. For detailed information about basic principles of nuclear magnetic resonance and magnetic resonance imaging, we refer to [5] and [6].

### 1.2.1 Spin-Echo Sequence

A Spin-echo (SE) sequence starts with the excitation of the hydrogen nuclei with a  $90^\circ$  radiofrequency (RF) pulse. This flips the magnetization vector into horizontal x-y plane (the normal of this plane is along the main magnetic field  $B_0$ ). The spins precess around the magnetic field: this phenomenon is known as Larmor precession. The angular frequency of this precession is given by

$$\omega = \gamma B_0 \tag{1.3}$$

where  $\gamma$  is the gyromagnetic ratio, a specific characteristic of the nucleus under examination. At the beginning, the spins are coherent, but they start dephasing due to various factors (i.e. magnetic field inhomogeneities and dipolar interactions). The dephasing of the spins determines a decrease of the signal ( $T_2^*$  decay). As proposed by Edwin Hann, the dephasing can be reversed through an application of a  $180^\circ$  RF pulse; in this way, the signal is refocused. The time between the first RF pulse and the echo is called TE and is twice the time between the two RF pulses. The generated echo is detected by a receiver coil. In Figure 1.6 a schematic Spin-echo sequence is shown.

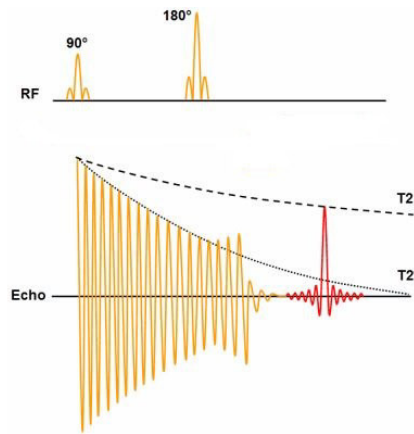


Figure 1.6: Spin-echo (SE) sequence.

### 1.2.2 Magnetic field gradients

Hann realized that the spin-echo MR signal could be useful to describe molecular diffusion and explained the reduction of signal in terms of the dephasing of spins caused by translational diffusion within an inhomogeneous magnetic field. Later, thanks to the studies of Carr and Purcell in 1954 [7], it was obtained a complete mathematical and physical description of diffusion measurements. In effect, considering that the spin's precession frequency is determined by the local magnetic field, if a magnetic field gradient is applied, spins at different locations experience different magnetic fields, therefore they precess at different Larmor frequencies. After a certain time, spins assume different phase shift, depending on their locations. Stronger gradients induce a more acute phase changes, permitting a higher sensitivity on diffusion.

### 1.2.3 Pulsed Gradient Spin-echo sequence and diffusion-weighted MR

In 1965 Stejskal and Tanner introduced innovations that made modern diffusion MRI measurements possible. They introduced the pulsed gradient spin-echo sequence (PSGE), which replaces the sequence of Carr and Purcell's constant field gradient with short duration gradient pulses [8]. It is important to make a distinction between the encoding time (pulse duration,  $\delta$ ) and the diffusion time (separation of the two pulses,

$\Delta$ ). The basic idea is to define the spatial position of water molecules (spin) at  $t=0$ , invert the spin phase with a  $\pi$ -pulse and decode the spin position after time  $\tau$ . After the application of a  $90^\circ$  rf pulse, a magnetic field gradient with amplitude  $G$  and duration  $\delta$  is turned on. The phase change induced is given by

$$\phi_1 = -qx_1 \quad (1.4)$$

where  $x_1$  is the position of the particle during the application of the first pulse and  $q = \gamma\delta G$ . A  $180^\circ$  rf pulse reverses the spins' phase. A second magnetic field gradient, with the same characteristics as the first one and a separation of time  $\Delta$ , causes non-moving spins to re-gain their original phase. The phase change due to this second pulse is given by

$$\phi_2 = -qx_2 \quad (1.5)$$

The global phase change that the particle experiences is given by

$$\phi_1 - \phi_2 = -q(x_1 - x_2) \quad (1.6)$$

It is evident that if the particles remained stationary during the time between the two magnetic field gradients, the phase shift would vanish and the magnitude of the echo will not change. On the other hand, if particles diffuse randomly through the excited volume, the spins will not re-phase completely and the overall signal, given by the sum of the magnetic moments of all spins, is attenuated due to incoherence in the orientation of the individual magnetic moments. It can be observed that the field gradients are applied linearly in one dimension, providing diffusion sensitization only to spin moving in that direction.

The development of the phase dispersion depends on the strength and duration of gradient and the time interval between application of the first and second gradients. The b-factor describes this degree of diffusion weighting and is proportional to the square of the gradient strength; for PSGE sequence, the b-factor is given by

$$b = \gamma^2 G^2 \delta^2 \left( \Delta - \frac{\delta}{3} \right) \quad (1.7)$$

where  $\gamma$  is the gyromagnetic ratio and  $G$  the amplitude of the magnetic field gradient pulses.

The signal can be acquired through a spin-echo, calculated for each pixel in an image as

$$f(x, y) = M_0 \left( 1 - e^{-TR/T_1} \right) e^{-TE/T_2} \quad (1.8)$$

where  $M_0$  is the "spin density" in that pixel, T1 and T2 reflect the time constants of spins in the tissue at that location. If we applied gradients, the signal of (1.8) is attenuated by the product of the diffusion coefficient  $D$  and the factor  $b$

$$f(x, y) = M_0 (1 - e^{-\text{TR}/T1}) e^{-\text{TE}/T2} e^{-bD} \quad (1.9)$$

It is convenient to introduce the MR signal attenuation quantity,  $E(q)$  that is given by

$$E(q) = \frac{S(q)}{S_0} \quad (1.10)$$

where  $S_0=S(0)$  indicates the signal in the absence of any gradients and  $S(q)$  is the diffusion-attenuated signal. As relaxation-related signal attenuation is approximately independent from the applied diffusion gradients, dividing  $S(q)$  by  $S_0$  eliminates the effects of relaxation and  $q$  dependence of  $E(q)$  is attributed to diffusion.

The diffusion gradients can be applied along any direction. The diffusion coefficient for any direction is estimated by collecting two sets of data: one,  $S_0$ , with the diffusion-weighting gradient amplitude set to 0 ( $b=0$ ), and the second,  $S_D$ , with a non zero diffusion-weighting gradient in the desired direction of measurement. Diffusion coefficient can be estimated as

$$D = \frac{\text{Log}[S_0/S_D]}{b} \quad (1.11)$$

When the displacement of water molecules is Gaussian and behaves according to (1.2), the relation expressed by (1.11) returns the ADC value. In this way, it is possible to quantify the apparent diffusion coefficient within each voxel of the imaged volume; thus, one can obtain quantitative maps of the ADC [9].

### 1.3 Diffusion Tensor Imaging

When there is an ordered tissue in our volume, it is not possible to characterize the behaviour of water molecules with a single diffusion apparent coefficient. Indeed, the ADC depends on the direction in which it is measured. For this reason, it was introduced the diffusion tensor  $\underline{D}$ , a more complex model to describe Gaussian diffusion in which the displacements per unit time are not the same in all directions [10].

$$\underline{D} = \begin{matrix} D_{xx} & D_{xy} & D_{xz} \\ D_{yx} & D_{yy} & D_{yz} \\ D_{zx} & D_{zy} & D_{zz} \end{matrix} \quad (1.12)$$

The diagonal element of this matrix correspond to diffusivity along three ortogonal axes, while the off-diagonal elements correspond to the correlation between displacements along those orthogonal axes. The tensor is simmetric ( $D_{ij}=D_{ji}$ , with  $i,j=x, y, z$ ). In a reference frame  $[x', y', z']$  that coincides with the principal direction of diffusivity, the tensor is reduced only to its diagonal terms  $D_{x'x'}$ ,  $D_{y'y'}$ ,  $D_{z'z'}$ . The echo attenuation becomes:

$$E(q) = \exp(-b_{x'x'}D_{x'x'} - b_{y'y'}D_{y'y'} - b_{z'z'}D_{z'z'}) \quad (1.13)$$

where  $b_{ii}$  are the elements of the  $\underline{b}$  matrix, which now replaces the  $b$  factor. In practice, measurements are made in the reference frame  $[x, y, z]$  of the MRI scanner gradients, which usually does not coincide with the diffusion frame of the tissue. Therefore, one must consider also the coupling of non diagonal terms of the diffusion tensor which reflect correlation between molecular displacements in perpendicular direction:

$$E(q) = \exp\left(-\sum_{i=x,y,z} \sum_{j=x,y,z} b_{ij}D_{ij}\right) \quad (1.14)$$

Diffusion tensors can be estimated from a minimal set of seven diffusion-weighted image. The set of diffusion-weighted images should include at least one non-diffusion-weighted images whose gradient directions are noncollinear and non-coplanar. In clinical scanners, imaging protocols that acquires diffusion-weighted images along multiple directions (more than 7) are commonly used [11]. Because it is symmetric, we only need to know the diagonal elements and three off-diagonal elements. When all off-diagonal elements are zero, we say that the tensor is diagonalized and its diagonal elements correspond to its eigenvalues. They are denoted as  $\lambda_1, \lambda_2, \lambda_3$  (ordered as  $\lambda_1 \geq \lambda_2 \geq \lambda_3$ ) and correspond to the three diffusivities along the principal axes of the diffusion tensor. The orientation of the principal axes is given by the three eigenvectors (denoted by  $\epsilon_1, \epsilon_2, \epsilon_3$ ), which are mutually ortogonal by definition. The orientation of the tensor is taken to be parallel to the principal eigenvector  $\epsilon_1$ , that is associated with the largest eigenvalue.

One way to visualize diffusion tensor is to use a *diffusion ellipsoid*. This is a representation of the diffusion distance covered in space by molecules in a given diffusion time. The three eigenvectors represent the three axes of the ellipsoid, and the lenght of each axis is the eingenvalue of the corresponding eigenvector; the eccentricity of the ellipsoid provides information about the degree of anisotropy and its simmetry. When the three eigenvalues have similar values ( $\lambda_1 \approx \lambda_2 \approx \lambda_3$ ) the shape of the ellipsoid is spherical; the diffusion ellipsoid of a voxel that contains a single population of axonal fibers appears

elongated along the orientation of the fiber trajectory ( $\lambda_1 \gg \lambda_2$ ) (see (a) in Figure 1.7); if a voxel contains two groups of crossing neuronal fibers there may be two or more orientations within a plane that show the maximal diffusion coefficient, so the diffusion ellipsoid has a planar shape (see b in Figure 1.7).

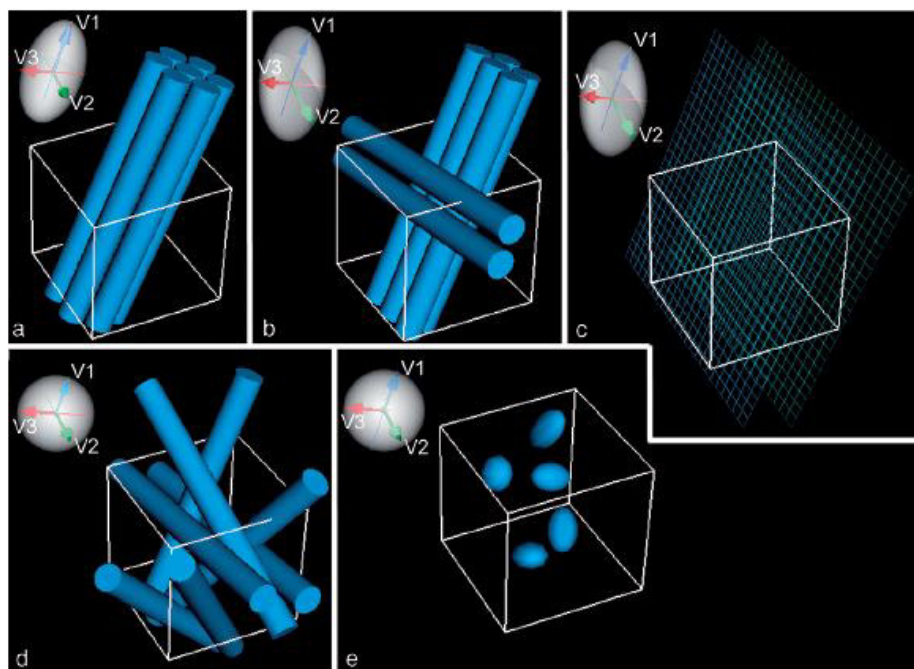


Figure 1.7: The shape of diffusion tensors related to local tissue microstructures voxel, in the case of (a) only one group of fibers, (b,c) two crossing fibers or surfaces and (d,e) multiple crossing fibers or no fibers. The image is taken from [11]

### 1.3.1 Parameters derived from the diffusion tensor

Diffusion ellipsoid permits to visualize tensor data in three dimensions, but it is convenient to have scalar measurements that can be used for easy quantification of information on tissue microstructure and architecture for each voxel.

### Mean diffusivity, axial and radial diffusivity

Mean diffusivity (MD) characterizes the overall mean-squared displacement of molecules (average ellipsoid size) and the overall presence of obstacles to diffusion. To obtain an overall evaluation of the diffusion in a voxel, it is important to consider an invariant measure (independent by the orientation of the reference frame). This measure is given by

$$\frac{\text{Tr}(\underline{D})}{3} = \frac{D_{xx} + D_{yy} + D_{zz}}{3} \quad (1.15)$$

where  $\text{Tr}(\underline{D})$  is the trace of the diffusion tensor.

We usually referred to  $\lambda_1$  as the axial diffusivity (or parallel diffusivity); it describes the diffusivity along the principal axis.

The radial diffusivity (RA) is instead obtained averaging the diffusivities in the two minor axes:

$$\text{RA} = \frac{\lambda_2 + \lambda_3}{2} \quad (1.16)$$

This parameter can be interpreted in terms of underlying biophysical properties since it is linked to myelin content and has an important role in the characterization of some neurological disorders [14].

### Diffusion anisotropy indices

To describe diffusion anisotropy, invariant indices must be found to provide an objective information, independent on the choice of directions made for measurements. The most used invariant indice is the fractional anisotropy (FA), defined as [12]:

$$\text{FA} = \sqrt{\frac{3}{2}} \sqrt{\frac{(\lambda_1 - \langle \lambda \rangle)^2 + (\lambda_2 - \langle \lambda \rangle)^2 + (\lambda_3 - \langle \lambda \rangle)^2}{\lambda_1^2 + \lambda_2^2 + \lambda_3^2}} \quad (1.17)$$

where  $\langle \lambda \rangle$  is the mean diffusivity. FA measures the fraction of the tensor that can be assigned to anisotropic diffusion. FA varies between 0 (isotropic diffusion) and 1 (or  $\sqrt{2}$ ) (infinite anisotropy).

### Fiber orientation mapping

Other information can be extracted from the mapping of the orientation in space of tissue structure by DTI images. It is believed that the directions of the fibers is colinear

with the direction of the eigenvector associated with the largest eigenvalue. One of the most intuitive approach is to use various primary colors to represent the orientation of the white matter tracts [13]. One can view fiber orientation in one voxel and, following a path of smooth transition in color from one voxel to the next, he can have an impression of the trajectory of the major white matter pathways (Figure 1.8).

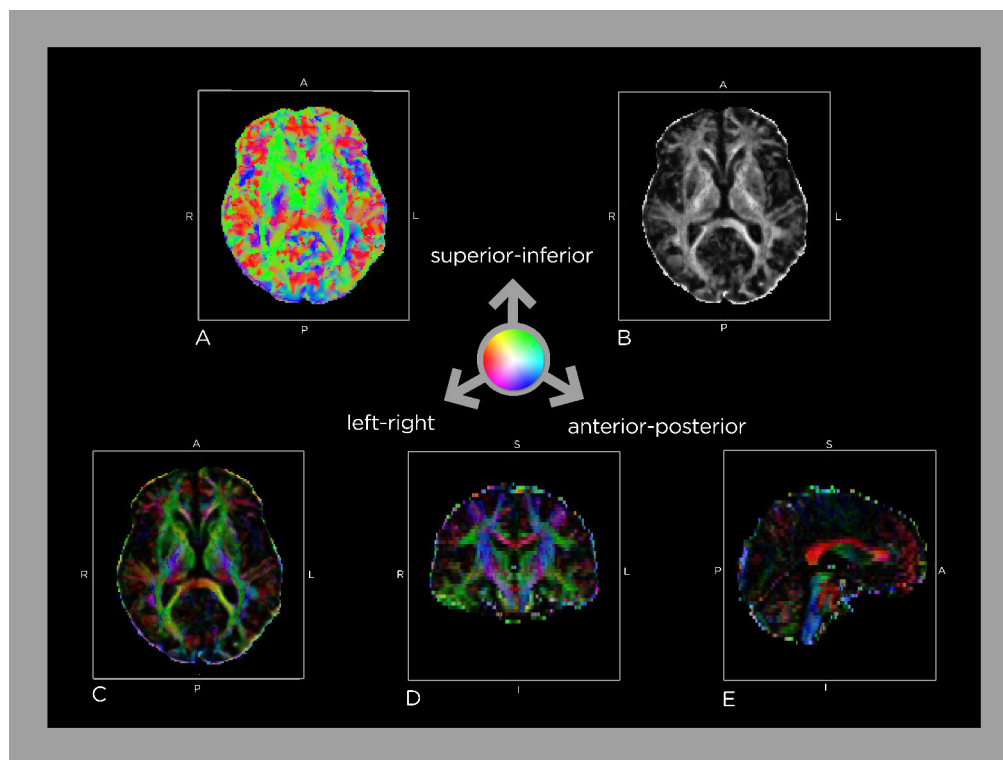


Figure 1.8: The x, y and z components of the principal eigenvector are mapped to the red, green and blue components of a full color image (a), To highlight areas of high anisotropy, the color map is multiplied by some anisotropy map, i.e FA (b). The resulting color map shows the three dimensional orientation of the tissue, regardless of the orientation of the slice (c-e).

### 1.3.2 Number of diffusion gradient directions

As underlined previously, diffusion-encoding gradients applied in different directions are used in DTI to estimate the diffusion tensor and measurements of parameters that

indirectly reflect brain microstructure. The diffusion tensor has six independent elements, and therefore, at least six non-collinear DW directions must be applied (plus one nondiffusion-weighted acquisition). On the other hand, it is important to achieve adequate signal-to-noise ratio (SNR) for diffusion parameter estimation [18]. To improve the estimation of diffusivity parameters (increasing the SNR), in particular way of eigenvalues if we have high anisotropy, two options can be used: either to add diffusion-weighting directions or repeat existing diffusion-weighting directions, performing several acquisitions. Recently, various studies have shown that using more than six directions provides better estimates (so reduced measurement error) of FA and MD, as compared to the results of application of six directions alone [15] [16]. Moreover, results suggest that multiple gradient directions reduce the uncertainty of the primary eigenvector direction and limit the potential bias as a function of tract orientation. This is an important issue for reconstruction of white matter tract starting from DTI data: a great number of gradient diffusion directions can assure a higher resolution and a more detailed final tract. However, the proposed numbers of DW directions vary greatly in the literature and are arbitrary [17].

## 1.4 Tractography

The local white matter orientation information, provided with the diffusion tensor imaging, can be used to reconstruct the pathways of major white matter bundles through the brain. The technique that allows to trace maps of brain connectivity is called *tractography*. To date, tractography is the only available tool for identifying and measuring white matter pathways non-invasively and in vivo. It is able to produce lines or trajectories capturing orientations of diffusion that are likely to represent real axonal trajectories, assuming that orientation of the largest component of the diagonalized diffusion tensor represents the orientation of dominant axonal tracts [20]. The great extent of the specialized literature concerning tractography demonstrates the great interest raised in the scientific community and the variety of strategies proposed to extract information from the diffusion MR images. Indeed, nowadays one of the most challenges in neuroscience is the determination of the wiring diagram of the human brain. Tractography is able to approach this goal at the macro-scale, because it investigates connections between brain areas using MRI-based techniques. This allows the possibilities to characterize the wiring diagram also in a systematic way across multiple individuals [21]. This is the

aim of a large-scale connectome project such as the Human Connectome Project (HCP), an initiative aiming to realize a comprehensive map of human brain connections in 1200 healthy adults using advanced neuroimaging methods [22]. Tractography has a central role and it is helping to establish the structural basis of the human connectome.

In order to reconstruct fiber bundles, tractography algorithms aim to find paths through the data field along which diffusion is least hindered. While this fundamental objective is common throughout diffusion tractography, strategy for achieving it vary greatly from algorithm to algorithm. The specific choice between these algorithms impacts on the interpretation of the reconstructed white matter pathways. Two main approach to generate the different trajectories exist: deterministic and probabilistic techniques.

### 1.4.1 Deterministic tractography

Deterministic (or streamline) tractography is the most intuitive and the most commonly used approach to represent the orientation of dominant axonal tracts. One can reduce DTI data set into a simple vector field, capturing in each voxel the main orientation of diffusion. Within a vector field, a streamline is any line whose tangent is parallel to the vector field. The methods of reconstruction consists in choosing a seed point and let the fiber expand following the local vector information on a step-by-step process. So as soon as the fiber reaches the boundary with a new voxel, the orientation is updated to match the local orientation (Figure 1.9). This process continues until a termination criterion is met, and is repeated in the opposite direction from the seed point.

The linear propagation approach is able to achieve high-resolution three-dimensional tracking of axonal projections [24]. In this particular approach, all the voxels in the data set that show an FA value above a certain threshold are chosen as seeds and each line is propagated according to the respective eigenvector. Every time the line reaches a new voxel, FA value and eigenvector are estimated: if the FA value is below a stopping threshold (similar to the starting threshold), or if the angle at which it would turn is too large to be biologically adequate, the streamline is truncated. Finally, the algorithm runs a second time in the opposite direction. The right choice of the threshold is a critical point: if FA threshold is too high the error propagation is reduced but less tracts are obtained; on the other hand, a lower threshold could force the algorithm to start the propagation in areas where the direction of principal diffusivity could be meaningless. Similarly, it is not trivial to decide when the line propagation process is terminated. To

this purpose, the FA is widely used because allows to distinguish easily between white matter and gray matter. Another criterion is the maximum angle between two successive steps. The curvature threshold is often made very strict when analyzing tract with minimal curvature, like the corticospinal tract. In general, it is widely assumed that the trajectories of the main fibers tracts in the brain are relative smooth.

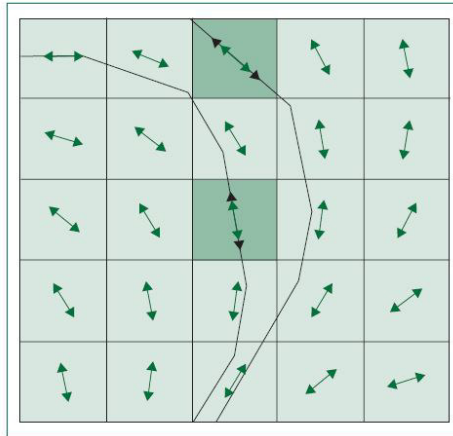


Figure 1.9: Streamlines are generated by connecting adjacent pixels on the basis of directional similarity of their maximum diffusional direction. Arrows show maximum diffusion direction at each voxel. The picture is taken from [23].

Deterministic tractography allows to isolate and visualize many different white matter pathways with precise results, with the help of a prior anatomical knowledge of the trajectories [25]. Two different approaches are used for in vivo dissection. A "one-region of interest" method is used for bundles whose boundaries are clearly delineated on the FA image (i.e central portion of the corpus callosum because in the neighborhood there are no other fasciculi). However, the majority part of cerebral white matter is composed of different bundles that run closely to one other and it is difficult to choose a single region of interest that includes only the fibers of one bundle. "Two-region of interest" approach tries to overcome this problem defining a second ROI that contains at least a section of the desired tract but not contains fibers of different fasciculi that pass through the first ROI.

Despite the success of in vivo dissection techniques in segmenting and visualizing major white matter pathways, streamline tractography (like other tractography approaches) is

susceptible to errors. The principal causes of errors are:

- Imaging noise that causes poor estimation of dominant diffusion directions;
- Modeling error, because the microscopic anatomy of the white matter tract can be more complex of the representation with a model;
- Integration error introduced with the mathematical description of the method.

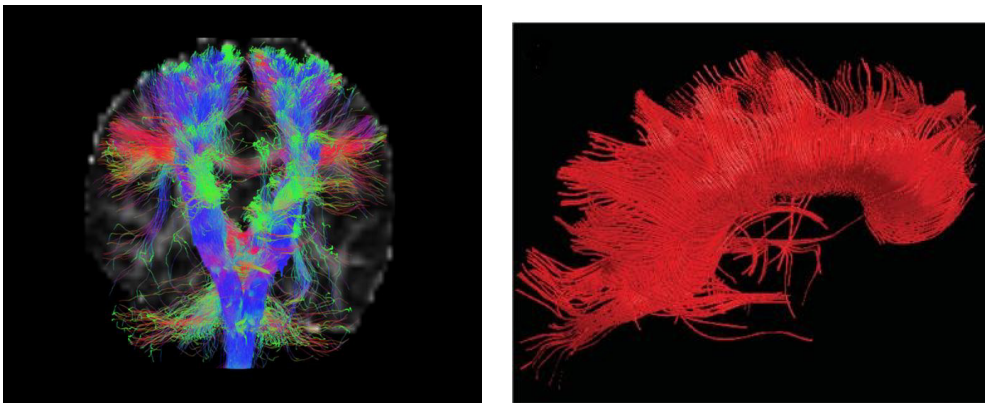


Figure 1.10: Example of streamlines reconstruction of the corticospinal tract (blue tract, on the left) and corpus callosum (on the right). The images were taken respectively from <http://www.healthcare.philips.com> and from Lazar [26]

In general, errors in streamline-based tractography accumulate along the streamline and could have a notable effect on reconstructed pathways. The most important limitation of deterministic tractography is due to the fact that running the streamlines following the route of the minimum hindrance to diffusion do not mean following the route of the axon. This means that it is hard to distinguish branching from merging or kissing axons and, in general, do not allow to intercept more than one fiber in a voxel. This is a strong limitation to a complete map of connectivity description.

On the other hand, deterministic tractography permits to obtain useful and impressive 3D representations of white matter tracts, with a level of details that matches the results of white matter dissection studies (see Figure 1.10. Moreover it is a procedure that involves a lower computation cost, with respect to other approaches.

## 1.4.2 Probabilistic tractography

Deterministic tractography algorithm considers, in each voxel, one fiber orientation estimate and provides a single pathway from each seed point. However, as previously explained, this approach is subject to errors and uncertainty and can not detect more than a fiber in each voxel. Probabilistic tractography aims to characterize this uncertainty, generating a large collection (or distribution) of possible trajectories from each seed point. Brain regions that contain higher densities of these trajectories indicate to have a higher probability of connection with the seed point [45]. Treating the problem in this way, the probabilistic tractography permits to delineate the tract through regions of high uncertainty, where deterministic method would usually stop. In effect, the uncertainty in fiber direction is high in areas in which diffusion anisotropy tends to be low; streamline tractography shows a limit in reconstructing pathways in low anisotropy areas.

The first step is to define a function that characterizes the uncertainty: an uncertainty orientational density function (uODF) is built and it describes the probability density on the true fiber orientation. The uncertainty is embodied in the line propagation process. At each step of the line propagation, instead of propagating along the principal eigenvector of the tensor, the orientation is drawn from a specific uODF. In general, one can imagine an orientation density function as a sphere whose surface value changes as a function of latitude and longitude. Moreover, it is important to underline that the uODF is not a physical property of the system. The uODF describes the uncertainty, due to noisy data and artifacts in MR scan, by quantifying our confidence that the true parameter of interest lies within any particular area on the surface of the sphere. The difference between the various probabilistic algorithms consists in the construction of the uODF.

### Bootstrapping

The most straightforward way to obtain the uODF would be to acquire multiple data sets for the same subject, reconstruct the fiber orientations and then consider these repeated measurements as samples from the uODF [28]. To build a good representation of uODF, many samples are required; considering that it is not practical to acquire a great number of independent data sets, this method is not feasible.

Bootstrap algorithm allows to obtain a large number of samples from independent data

sets. This is a non parametric statistical methods that helps to estimate the uncertainty of a given statistic: it randomly selects individual measurements from a set of repeated measurements and generates new data sets. This is done since each considered data set contains acquisition along different gradient orientations, so new data sets will build up with each orientation taken from a different data set. The latter procedure has some important disadvantages, in particular each of the new data sets is obtained from the same original data sets. Thus, the bootstrapped data sets are not independent samples and this means an underestimation of uncertainty. To overcome this problem, a *wild* bootstrap method is used [29]. It permits to start from a single original data set. If one fits a diffusion model (i.e. diffusion tensor) to this data set, the predicted signal will not fit the data precisely, due to image noise and modeling error. The difference between the predicted and measured signal are defined as residual. The wild bootstrap generates sample data sets by interchanging these residuals between measurements and by multiplying them randomly by 1 or -1.

### Bayesian Methods

Bayesian technique allows to calculate and represent the uncertainty associated with inference of any parametric model. Uncertainty and belief are represented in the form of posterior probability density functions. Bayes' rule states that the posterior probability of the model parameters  $\omega$  given the data  $s$  and the model  $M$ ,  $P(\omega|s, M)$ , is proportional to the likelihood of seeing this data set given these parameters,  $P(s|\omega, M)$ , multiplied by the prior belief about the model parameters,  $P(\omega|M)$ .

$$P(\omega|s, M) = \frac{P(s|\omega, M)P(\omega|M)}{P(s|M)} \quad (1.18)$$

The likelihood must consider the parametric assumptions between quantity of interest and the data and a parametric assumption about the noise structure (i.e., respectively tensor model and Gaussian distribution [30]). The prior distribution describes information known about the parameters before any data are collected; in this case, it is useful to impose physical constraint on some parameters (i.e in the fitting of the diffusion tensor model, the eigenvalues of the diffusion tensor are constrained to be positive) [30]. After signal and noise model have been established in the likelihood and prior distributions, it is possible to generate samples (i.e a set of orientation that would approximate the uODF) from posterior distribution, once Bayes' equation is solved. One of the most

flexible technique used to solve this equation is the Markov Chain Monte Carlo (MCMC) estimation process; this is a sampling procedure that proposes samples preferentially in areas of high probability.

### **Uncertainty propagation: BEDPOSTX algorithm**

To estimate whether it is possible to connect a region A to region B through the diffusion data using a probabilistic tractography is not a trivial purpose. The reason is that at each voxel, differently from streamline tractography, there are an infinite number of possible orientations we might follow and an infinite number of possible paths, with different probability to be the right one. Then, we must consider all the probabilities associated with each path that connects the two regions. The problem is overcome with the generation of sample streamline from final distribution; after drawing many samples, a spatial probability density function (pdf) is built on the path, leading to the first point A. Finally this distribution is discretized into voxels or brain regions.

An example of algorithm that practises the method described above is BEDPOST (Bayesian Estimation of Diffusion Parameters Obtained using Sampling Techniques) [30], also if in our study we used an extension of it, BEDPOSTX (where X stands for crossing fibers) that works in the same way of the first but can account for more than one fibre orientation in each voxel [31]. The algorithm is able to establish the most appropriate number of fiber orientations for the data at each voxel and carry out the probabilistic tractography. It uses a different model from the standard diffusion tensor model. The new model is a two-compartment partial volume model. The first compartment models diffusion in and around the axons, with diffusion only in the fiber direction. The second models the diffusion of free water in the voxel as isotropic. In this way, the diffusivity in all directions perpendicular to the fiber axis is constrained to be the same. To fit the parameters of this model to signal at each voxel, a Bayesian estimation it is used. In order to avoid to fit a complex model to the data in voxels which support a single fiber orientation, it is introduced a Bayesian procedure known as automatic relevance determination (ARD). ARD fits the more complex model, but excludes from computation of likelihood the parameters that are not supported by data (in the posterior distribution they are forced to assume zero value). The method for tracing probabilistic tracts is similar to the streamline tractography, but instead of considering the most likely principal diffusion direction, it draws a sample from the posterior distribution on principal diffu-

sion directions and progresses along the same direction. The streamline is now sampled from the connectivity distribution; this procedure for generating streamlines is repeated a large number of times (typically 5000). When various streamlines arrive to the same point, each of this will choose different samples from the posterior distribution on local orientation at that specific voxel, accounting for uncertainty in local fiber orientation. The probability of the dominant streamline through any single voxel is estimated dividing the number of streamline that passed through the single voxel by the total samples drawn. In order to recognize fibers different from the dominant one, the algorithm draws a sample from each population that has not been forced to zero by automatic relevance determination and chooses that sample whose orientation is closest to parallel to the orientation of a streamline drawn previously to indicate which population was suitable for a multiple fiber analysis.

The great advantage of the probabilistic tractography is to characterize white matter tracts considering more than one dominant diffusion orientations in each voxel. These technique has revealed large regions of white matter in which a single dominant orientation does not adequately describe the local diffusion profile (i.e in the corticopinal tract) [31].

In general, studies that use tractography to explore brain connectivity and its variations across brain area, subjects or species, extract summary statistics from the tracking process to make quantitative comparisons. In deterministic tracking, the extracted number represents either the number of streamlines from a starting point A to an ending point B, or the proportion of streamlines from A to B among other possible targets. It is important to not confuse the obtained streamlines with the axonal fibers. In facts, the size of an imaging voxel is typically a few millimetres cubed so a single voxel could contain tens of thousand of axons. Furthermore, the number of streamlines is not a direct measure of anatomical connectivity. From this point of view, probabilistic tractography is more quantitative [32]: probabilistic tracking gives us an estimate of our confidence across the direction of minimum hindrance to diffusion. We can say, for example, that we are more confident that A connects to B than A connects to C. Or that A connects to B in one individual than in another. This confidence in the route of diffusion is not a measure that we can get from deterministic number of streamlines approach. But these probabilities can not be considered as direct measurements of connection strenght, since

our confidence level depends on various factors and some of these are not related to the connectivity meaning. For example, the measures can be influenced by the distance between regions, because of the fact that errors and uncertainty accumulate during the tracking process. The confidence estimation could also depend on the size of voxels and brain areas, the noise level or the algorithmic errors.

In conclusion, tractography has many limitation but if we deeply understand them, we could take advantage of this extremely useful tool to investigate white matter connectivity.

### 1.4.3 Application and future directions

White matter tractography has been used to demonstrate the in vivo mapping of the white matter pathways of the brain. Initially, white matter studies replicated the major fiber structure known from classical anatomy. The similarity of the reconstructed tracts to the known anatomy (studied with post-mortem techniques), confirmed the potential of tractography for noninvasive mapping of distinct white matter structures. More recently, tractography studies have generated new information regarding brain organization and development. In recent times, it is used to generate connectivity matrices of the entire brain and to study brain structure at the network level [33]. In this approach, the obtained trajectories are used to define the properties of the connections (or edges) between different nodes of the brain network and node properties, that are integrated to identify relevant network substructures and their interrelations. Moreover, measures describing brain network properties may potentially be useful in understanding physiological disease mechanism and evolution of neurological disorders including epilepsy and neurodegenerative diseases.

# Chapter 2

## Corticospinal Tract

The corticospinal spinal system is one of the most important descending tracts in the central nervous system. It serves various essential motor functions for our voluntary movements, so its pathway is of great interest to neuroscientists and neurologists. One of the earliest studies on corticospinal tract, is that of Turk, in 1851, which identified the fibers and found two separate tracts: the lateral corticospinal tract and the anterior corticospinal tract [35]. Later, it was found that both the lateral and anterior tracts were divisions of the same pathway and it was possible to describe the bundle more accurately. All of these early studies in human were done through the post-mortem work on samples. Recently, a non invasive mapping of the complete tract is possible thanks to the advent of advanced brain neuroimaging techniques, like diffusion tensor imaging.

### 2.1 The motor cortex

All the body's voluntary movements are controlled, planned and executed by the brain. One of the brain areas most involved in controlling these voluntary movements is the motor cortex. It is located in the rear portion of the frontal lobe. The motor cortex is divided into two main Brodmann areas <sup>1</sup>, Area 4 and Area 6. Area 4 is also known as "the primary motor cortex" and forms a thin band along the central sulcus, in

---

<sup>1</sup>In the early 20th century German neurologist Dr. Korbinian Brodmann defined 52 regions of the cerebral cortex of humans and monkeys that appeared to have different cellular morphology and organization, today known as *Brodmann Areas*. Over the past century clinical findings and neurophysiological studies have confirmed that these microstructural differences correlate well with cortical function specialization [41].

particular is the fold of cortex just anterior to the central sulcus. Area 6 lies immediately forward of Area 4. The location of motor cortex was confirmed in the 20-th century in brain operations performed by neurosurgeons such as Dr. Wiler Penfield, in Montreal. During neurosurgical operation on epileptic patients, Penfield stimulated with electrical probes various area of the cortex to assess the eloquent areas of cortex that has not to be removed. He discovered that stimulations applied to the precentral gyrus triggered localized muscle contractions on the contralateral side of the body. In this way, he could develop a complete map of the motor cortex, known as the motor homunculus (see Figure 2.1) [?]. The diagram looks like a grotesque little man and indicates the location and amount of cortex devoted to each part of the body. One of the most important aspects of this representation is that areas assigned to various parts of body on the cortex are proportional not to their size, but rather to the complexity of the movements that they can perform. So the areas related to hands and face are especially large compared with those for the rest of the body: this is because of the fact that humans put great emphasis on speech and manipulating of objects by the hands.

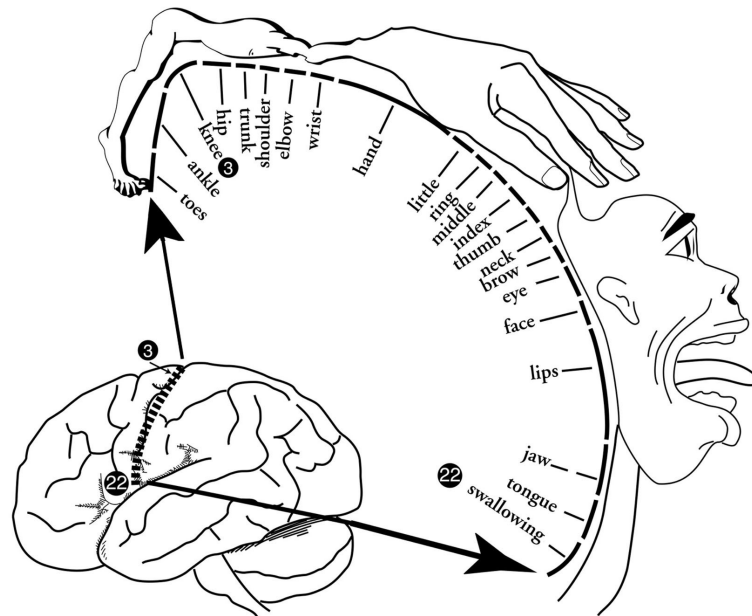


Figure 2.1: The motor homunculus, based on Penfield's classic diagram.

## 2.2 Anatomy of the corticospinal tract

The corticospinal tract represents the highest order of motor function in humans and is most directly involved in control of fine, digital movements. This tract arises in pyramidal neurons of cortex and ends in spine. Specifically, it starts in the precentral gyrus, the "primary motor cortex". There is a motor homonculus in this gyrus, with the feet represented near the superomedial part of the motor cortex and the leg, trunk, arm, hand and head represented progressively further inferior on the lateral side of the brain. Axons arising from neurons in the precentral gyrus exit through the white matter and pass through the internal capsule where they are topographically arranged in the posterior limb. Corticospinal fibers traverse the middle portion of the cerebral peduncle of the midbrain and then the basal pons, with the fibers representing the hand in the anteromedial portion and those representing the foot posterolateral to them [36]. They enter the pyramids of the medulla; in the pyramids over 90% of the axons decussate and become the lateral corticospinal tract, continuing on the contralateral side of the spinal white matter. The other 10% enters the medial (anterior) corticospinal tract (Figure 2.3).

The corticospinal tract is essentially bundles of axons; the cell bodies from which they stem reside in the cerebral cortex. These neurones are known as upper motor neurones (UMN) as they descend from the cortex to synapse on neurones within the brainstem or spinal cord [37]. Damage to UMN's results in the upper motor neurone syndrome, whereby the motor area for which the neurones are responsible exhibits paralysis or spasticity.

Throughtout its course, asymmetry has been described in the corticospinal tract. In particular, it has been observed that this asymmetry is a result of more corticospinal fibers on the right side than those on the left [38]. Moreover, in literature there are different positions respect to the relation between asymmetry and handedness. For example, Herve et al [39] found the existance of an asymmetry that is hand dominance-dependant in the precentral gyri, while other works, like the study of Westerhausen et al [40], showed asymmetry of the corticospinal tract at the level of the internal capsule, but failed to demonstrate a direct correlation to hand dominance.

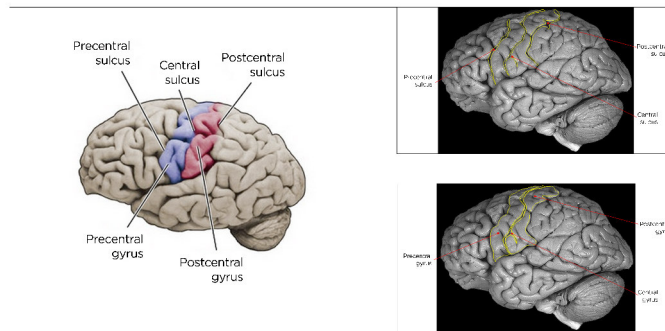


Figure 2.2: Illustration of the precentral gyrus.

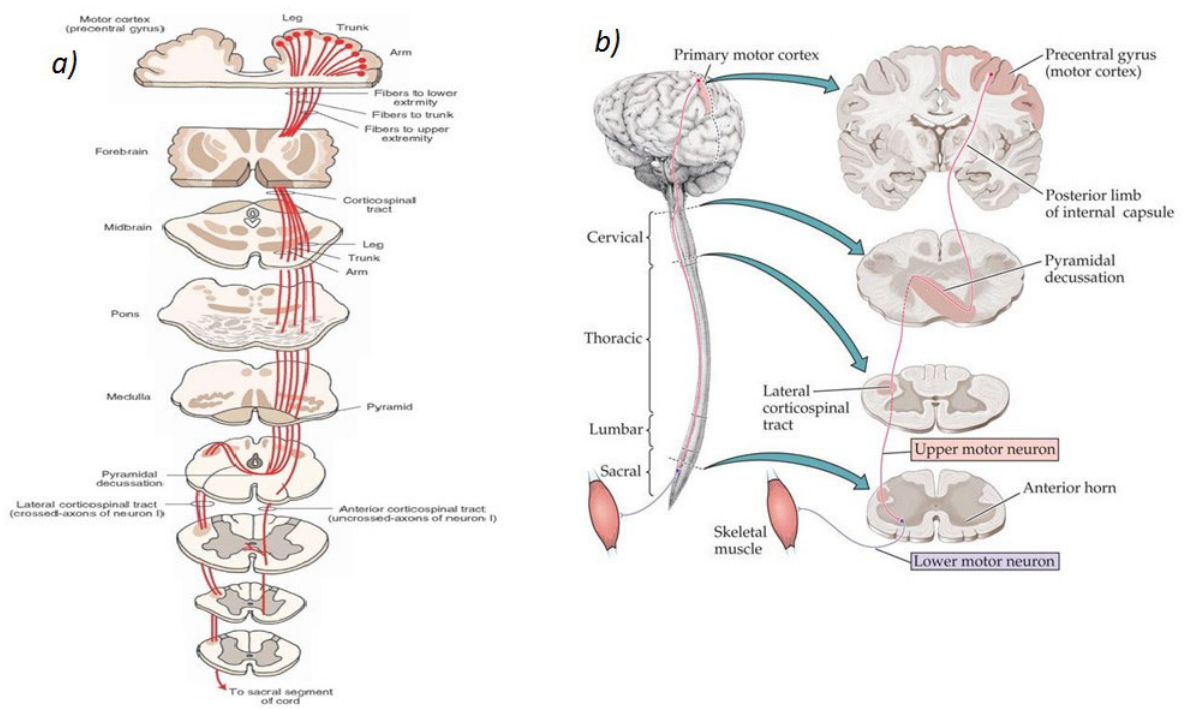


Figure 2.3: Schematic illustration of the main component of the CST pathway throughout its course from its cortical origin.

# Chapter 3

## Materials and methods

We dealt with DW-MRI data from 25 healthy controls, obtained, for each subject, with two different number of diffusion-encoding gradient directions (NDGD). After pre-processing of data, we studied an innovative method to obtain the corticospinal tract using ROIs (Regions of Interest) drawn in a mean template. The novelty of the method is also the use of masks drawn through grey matter parcellation. At a later stage, an along-tract data analysis was performed.

### 3.1 Participants

Twentyfive healthy adult subjects (12 men and 13 women), with a mean age of 38.2 years and standard deviation of 16.3 years (range between 20-83 years), were recruited by the Functional MRI Unit at the Department of Biomedical and Neuromotor Sciences of the University of Bologna (Table 3.1). All acquisitions were performed between July 2009 and March 2012. None of the participants had any history of neurologic or psychiatric disorders or brain injury. The protocol study on healthy volunteers was approved by the local ethics committee, and informed consent was obtained from each subject.

| N  | Age(yrs) | Sex |
|----|----------|-----|
| 1  | 20       | M   |
| 2  | 21       | F   |
| 3  | 22       | M   |
| 4  | 23       | F   |
| 5  | 24       | F   |
| 6  | 24       | F   |
| 7  | 25       | M   |
| 8  | 28       | F   |
| 9  | 28       | F   |
| 10 | 28       | M   |
| 11 | 28       | M   |
| 12 | 29       | M   |
| 13 | 30       | F   |
| 14 | 32       | F   |
| 15 | 32       | M   |
| 16 | 33       | M   |
| 17 | 37       | F   |
| 18 | 41       | M   |
| 19 | 41       | F   |
| 20 | 47       | F   |
| 21 | 50       | M   |
| 22 | 51       | M   |
| 23 | 60       | M   |
| 24 | 73       | F   |
| 25 | 83       | F   |

Table 3.1: Demographic data of healthy subjects recruited for the study

## 3.2 Data acquisition

Brain DW-MRI scans were acquired using a MR medical scanner GE Medical System Signa HDx 15 at Functional MR Unit at S.Orsola Hospital in Bologna. Technical specifications of scanner are the following:

- magnetic field strenght of 1.5 T;
- gradient strenght of 33 mT/m;
- slew rate of 276  $\mu$ s;
- maximum rise time of 120 T/m s;
- head coil.

T1-weighted images were obtained with the Fast Spoiled Gradient Echo Sequence. For each subject, DW data were collected with a single-shot echo-planar sequence, using 25 and 64 directions of diffusion gradient. Acquisitions with the two different NDGD were collected for each subject in the same day. DTI acquisition parameters are listed in Table 3.2

| 25 direction Tensor                 | 64 direction Tensor                 |
|-------------------------------------|-------------------------------------|
| bvalue = 900 $s/mm^2$               | bvalue = 900 $s/mm^2$               |
| 5 volumes with b = 0 $s/mm^2$       | 7 volumes with b = 0 $s/mm^2$       |
| TR = 10000 ms                       | TR=10000 ms                         |
| TE = 91.4 ms                        | TE = 87 ms                          |
| FOV = 32 cm                         | FOV = 32 cm                         |
| NV = 256 x 256                      | NV = 256 x 256                      |
| In-plane resolution: 1.25 x 1.25 mm | In-plane resolution: 1.25 x 1.25 mm |
| Resolution along z-axis: 4 mm       | Resolution along z-axis: 3 mm       |
| Acquisition time: 5 min 10 s        | Acquisition time: 11 min 40 s       |

Table 3.2: Acquisition parameters for the two different NDGD (Number of Diffusion Gradient Direction).

As reported in Table 3.2, the scan time for DTI with 64-NDGD is almost doubled with respect to DTI with 25-NDGD. For this reason, the shorter scan time makes the DTI with 25-NDGD more suitable for clinical acquisitions.

### 3.3 Data preprocessing

Data analysis was carried out using tools of the Brain Software Library from the Oxford Centre for fMRI ([www.fmrib.ox.ac.uk/fsl](http://www.fmrib.ox.ac.uk/fsl)). In particular, the FMRIB Software Library (FSL) is a comprehensive library of analysis tools for functional, structural and diffusion MRI brain imaging data [42][43].

In order to reduce motion and eddy current effects, data preprocessing was performed.

Almost all DTI images are susceptible to artifacts due to eddy currents. In fact, when the diffusion gradient pulses are switched rapidly, the time-varying magnetic field of the gradient results in current induction in the various conducting surfaces of the scanner. These magnetic field gradients may persist after the primary gradients are switched off and induce distortions in diffusion weighted images. To reduce the effects of these artifacts, we run, for each image, the Eddy Current Correction algorithm of the FDT tool (FMRIB's Diffusion Toolbox) of FSL for analysis of diffusion weighted images. Eddy Current Correction corrects for these distortions, and for simple head motion, using affine registration to a reference volume.

Subsequently, DTI images of all subjects were submitted to visual inspection. It was used the *Movie Mode* of FSL, that allows to observe cycles through volumes in multi-volume images and to rapidly notice artefacts due to motion or system malfunctions during acquisitions. In general, images were characterized by an high quality, due to the fact that acquisitions were performed on healthy subjects. Only seven DTI data referring to six subjects (five with 64-NDGD and 1 at both 25- and 64-NDGD) showed a motion artifacts. In order to improve the quality of these data, it was used an algorithm developed at the MR functional Unit at Policlinico S. Orsola, DIBINEM Unibo, called *Uroboro*. *Uroboro* removes slices that show a signal dropout with adjacent slices and interpolates the remaining slices to restore the volume. Enhancements we achieved were often poorly visible to visual inspection since the original images were not too hardly damaged. Anyhow, we consider that the process could be useful for data acquired on patients due a more consistent quantity of artifacts; in this case, the enhancement is

clearly visible.

After correcting eddy current artifacts and applied *Uroboro*, we used for all subjects DTIfit algorithm (within FDT tool) that fits a diffusion tensor model at each voxel. We obtained diffusion maps of FA, MD,  $\lambda_1$ ,  $\lambda_2$ ,  $\lambda_3$  and RA. We also obtained color-coded maps for FA values. In Figure 3.1 mentioned maps are shown for subject N=1.

At a later stage, all images were underwent *Uroboro2* algorithm, implemented at MR functional Unit. This algorithm produces a synthetic EPI image with a contrast created by a non-linear combination of  $\lambda_1$ ,  $\lambda_2$ ,  $\lambda_3$  values and with a spatial resolution equal to the DT-EPI images. Then, volumetric T1-weighted and DTI images, for each subject, were registered to the synthetic EPI one. The first ones were registered using FLIRT, the FSL tool for automated linear inter- and intra-modal brain image registration [44]. The tool calculates the affine transformation that registers the input volume labeled as *source image* to the *target image* (or reference volume). The transformation is saved as 4x4 affine matrix; the default cost function used is the Correlation Ratio. DTI images were registered to the synthetic EPI with a nonlinear transformation, using FNIRT, a tool similar to FLIRT that works for nonlinear transformations. The matrix obtained was stored as  $T1_t o_D TI$ . Co-registration of 3D and DTI images is a non trivial purpose because of the great dissimilarity between them: a direct registration often returns inadequate results. *Uroboro2* takes advantage of an intermediate step due to registration of both images to the synthetic EPI that has the same contrast of the volumetric image and is similar to the DTI one.

To make further data analysis shorter, images were cut out so that zero pixels of background were removed. In particular, diffusion weighted images, all the diffusion maps and the volumetric images were involved in the process. In this way, we reduced computational cost of algorithms applied in following steps.

In order to prepare data for tractography, *BedpostX* algorithm was applied. *BedpostX* stands for Bayesian Estimation of Diffusion Parameters Obtained using Sampling Techniques. The X stands for modelling crossing fibres, because it allows to determine the crossing fibres per voxel [31]. This algorithm builds up distributions on diffusion parameters at each voxel and create files necessary for probabilistic tractography. It runs starting from the following data:

- Diffusion-weighted and no diffusion weighting volumes;

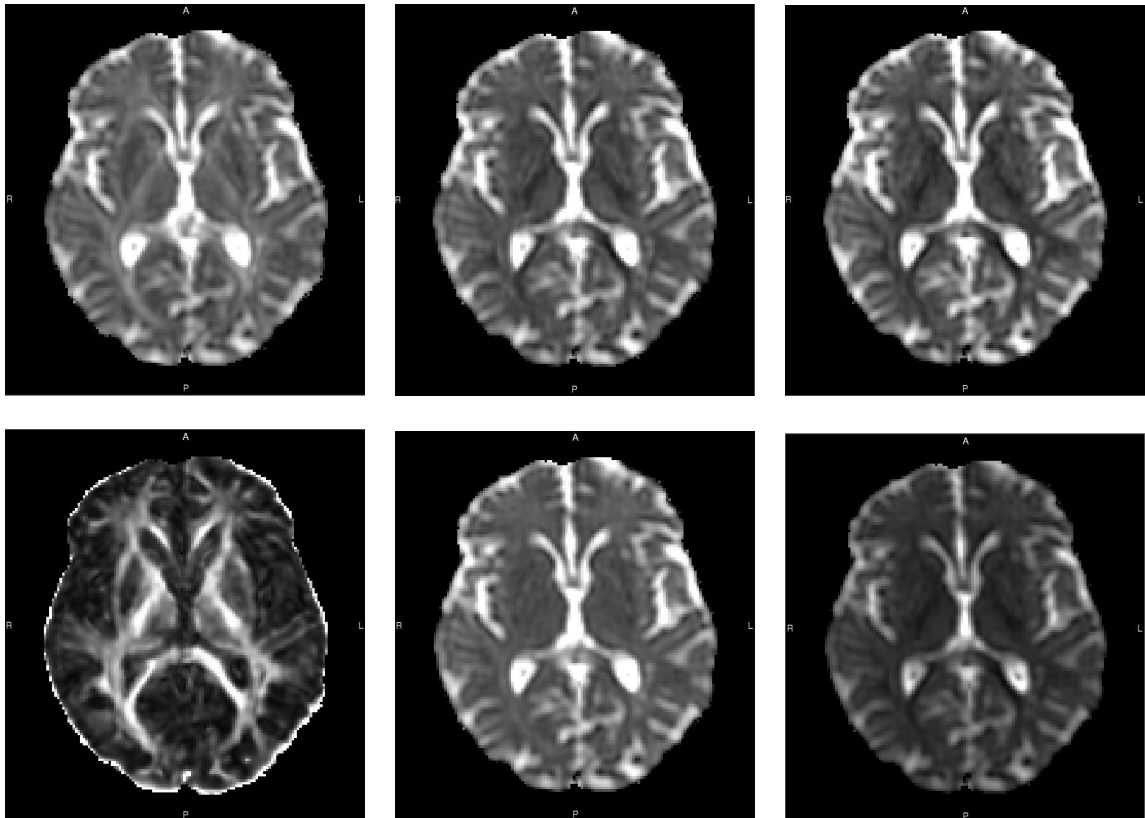


Figure 3.1: Diffusion maps of subject N=1 at 25-NDGD. Top line, from left to right:  $\lambda_1, \lambda_2, \lambda_3$  maps. Bottom line, from left to right: FA, MD, RA maps.

- 3D binary brain mask volume obtained deleting non-brain tissue from an image of the whole head (BET algorithm);
- The list of gradient directions applied during diffusion weighted volumes and the list of bvalues applied during each volume acquisition.

Afterwards, the algorithm creates all files for probabilistic tractography. We reports some important outputs:

- $mean\_th< i > samples$  and  $mean\_ph< i > samples$  that represent the mean of distribution on theta and phi, where theta and phi together represent the principal diffusion direction in spherical polar co-ordinates and  $< i >$  indicates the i-th fibre detected;
- $mean\_f< i > samples$  that is the mean of distribution on FA.

Finally, for each subject, images with 64 NDGD, obtained by Uroboro2, are registered to the corresponding with 25 NDGD, using an affine transformation with 6 DOF. This was an important phase of pre-processing, since the data analysis was mainly performed on images obtained with the smaller direction number of diffusion gradient and successively brought back into the space of 64 NDGD. The matrix of this transformation was stored as *64to25.mat* and it was useful in further steps. The choice has been made taking into consideration one of the aims of the project: understanding how reliable an acquisition with 25 NDGD is.

### 3.4 Tractography of corticospinal tract

The aim of our tractography analysis was to generate measures on the CST (in each subject, for the two different NDGD). In the first phase of our study, we obtained measures of FA, MD and of the connectivity distribution and in a later stage, we conducted an analysis also on other parameters, see section 4.2). In order to compute these metrics, the first step was to use a probabilistic tractography algorithm[45][46]. Therefore, we could estimate at each voxel the probability distribution on the principal diffusion direction. The width in this distribution represents uncertainty in diffusion direction, which is due to factors such as the potential co-existence of many fibre directions within a voxel,

image noise and subject motion in the scanner. These local distributions were later used to estimate the probability that a fiber pathway leaving voxels chosen as "seed" (starting points) will pass through any other voxel.

### 3.4.1 State of art

The practical delineation of the white matter tract, according to the anatomy of corticospinal tract, is a very important step. It is necessary to identify specific landmarks of the tract, or, in other words, anatomical reference points through which the bundle certainly passes. It is a critic phase of the work, since it determines the successful outcome of the results. The first step of the process is to manually draw regions of interest (ROIs) and then propagate lines from the ROI pixels defined as masks. Two main masks have to be drawn:

- a *seed mask*: set of voxels from which fiber pathways start;
- a *target mask*: set of voxels that represent the ending point of the tract.

Other kind of masks can be drawn, to delineate the tract (see section 3.4.2).

To date, the majority of studies on tractography of CST use a 2ROI-method with one mask located in cortical zones [47][48][50]. In particular, Hasina *et al.* delineate the tract under study with a deterministic algorithm using two manually drawn ROIs: a seed ROI placed at the level of the cerebral peduncles and a target ROI (only one for two sides of brain) placed at the level of the precentral gyrus. The team of Hattori *et al.* takes advantage of the same idea but uses it in the opposite way: the CST is obtained with a seed mask in the motor cortex and a target mask at the level of the cerebral peduncle. Also the study conducted by Ciccarelli *et al.* refers to a seed mask composed by seven bilater cortical zones manually outlined for each subject on T1 images (and to a target mask in the posterior limb of the internal capsule). This has been done by using, as a guide, regions of interest derived from Brodmann atlas via MRIcro<sup>1</sup>. In Figure 3.2 ROIs

---

<sup>1</sup>In the early 20th century German neurologist Dr. Korbinian Brodmann defined 52 regions of the cerebral cortex of monkeys and also human that appeared to have different cellular morphology and organization, today known as *Brodmann Areas*. Over the past century clinical findings and neurophysiological studies have confirmed that these microstructural differences correlate with cortical function specialization.

of mentioned studies are shown.

We considered the intuition of placing the seed ROI at the level of cortical zones reliable and appropriate: a tract starting from the precentral gyrus is related to the function of corticospinal tract that conducts impulses from the brain to the spinal cord. In this way, the pathway of the signals is recreated. In our study, we prove the feasibility of this intuition.

### 3.4.2 Tract drawing: PROBTRACKX algorithm

In order to delineate the CST, we used FDT (FMRIB's toolbox). The probabilistic algorithm implemented within FDT is PROBTRACKX (Probabilistic tracking with crossing fibres) that allows to draw the specific white matter tract from user-specified seed voxels. Briefly, it continuously samples from the distributions of voxel-wise principal diffusion directions, each time computing a streamline through these local samples to generate a probabilistic streamline or a sample from the distribution on the location of the true streamline. By taking many such samples FDT is able to build up the histogram of the posterior distribution on the streamline location, or the connectivity distribution[51]. The output is an image in the space of specified seed. All brain voxels will be characterized by a number, representing the connectivity value between that voxel and the seed voxel (number of samples that pass through that voxel). Seed can be specified either as a Single Voxel, a Single mask, or Multiple Masks. In the latter case, the algorithm repeatedly samples tracts from every seed mask in a list, and retains only those tracts that pass through at least one of the other seed masks. The output is the sum of the connectivity distributions from each of the seed masks. PROBTRACKX also allows to specify targets for the tractography:

- *Waypoint masks*: streamlines are only retained if they intersect the mask. If more than one waypoint mask is set, PROBTRACKX will discard from the calculation of the connectivity distribution tracts that do not pass through all these masks;
- *Exclusion masks*: pathways will be discarded if they enter the exclusion mask;
- *Termination masks*: pathways will be terminated as soon as they enter the termination mask. The difference between an exclusion and a termination mask is

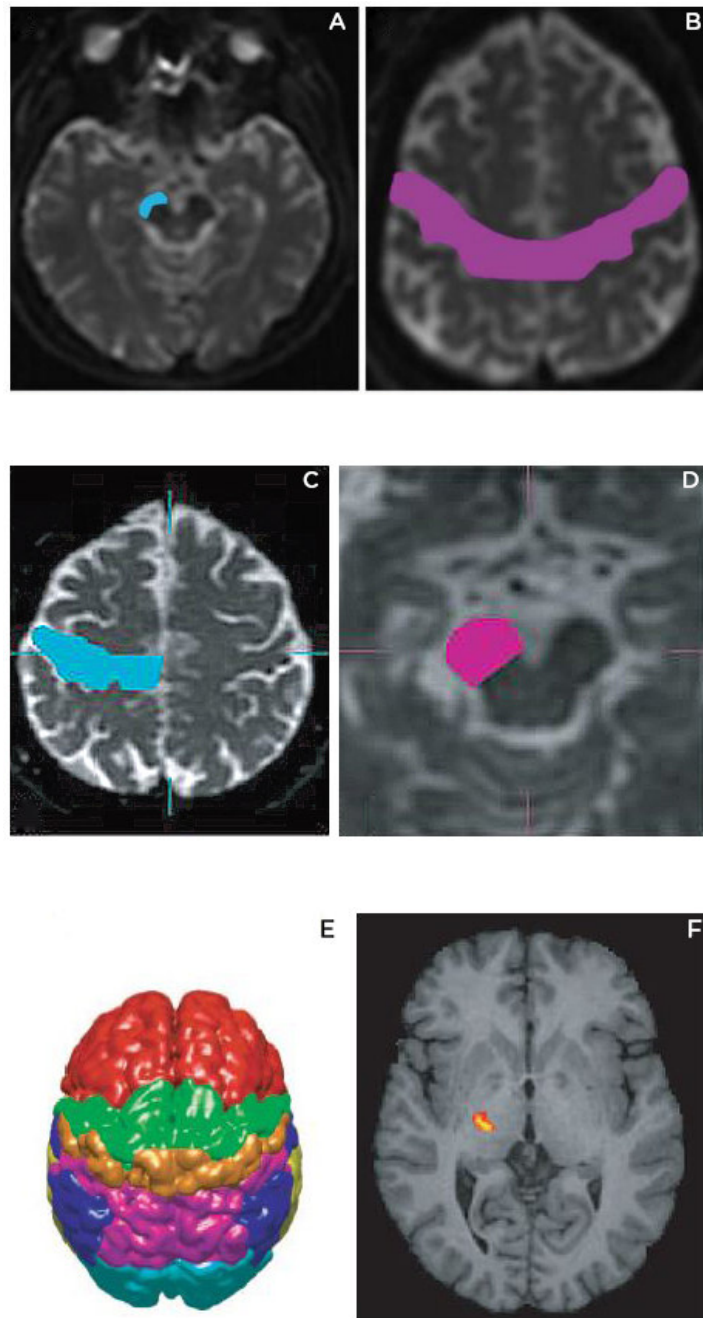


Figure 3.2: Seed masks (on the left) and target ROIs (on the right) used in different studies. (A) and (D) ROIs at the level of the cerebral peduncles; (B)-(C) Seeds at the level of the precentral gyrus and of the motor cortex; (E) Division of the cerebral cortex in seven bilateral cortical regions, outlined according to Brodmann atlas; (F) Region in the posterior limb of the left internal capsule.

Images are taken from Hasina et al. (A-B)[48], Hattori et al. (C-D)[50], Ciccarelli et al. (E-F)[47]

that in the latter case, the tract is stopped at the target mask, but included in the calculation of the connectivity distribution, while in the former case, the tract is completely discarded;

- *Classification targets*: the algorithm will quantify connectivity values between a seed mask and any number of user-specified target masks. This option is only active when the seed mask is a single mask.

It is allowed to specify the number of individual pathways (or samples) that are drawn through the probability distributions on principle fibre direction. We decided to maintain the default number that is set on 5000 for every voxel.

PROBTRACKX returns, as output, *fdt\_paths*, a tridimensional image file containing the output connectivity distribution to the seed mask, and *waytotal*, a text file containing a single number corresponding to the total number of generated tracts that have not been rejected by target masks criteria. The graphical User interface for FDT is shown in Figure 3.3.

### 3.4.3 ROIs definition and tracking the CST

The three main landmarks used to delineate the CST in our study are pons, posterior limb of the internal capsule and precentral gyrus. We chose to use pons since we wanted to investigate the bundle without considering the pyramidal decussation (under the pons). Firstly, we decided to delineated CST only in four subjects, randomly chosen. The aim of this initial analysis is to define the seed mask that assures the best results, and to develop a procedure of tract construction. In order to apply PROBTRACKX algorithm, we manually drew ROIs ,in each subject, on FA maps with 25-NDGD. We obtained masks at the level of pons, posterior limb of the internal capsule, precentral gyrus. Finally, we realized an exclusion mask, identical for all subject: pathways will be discarded if they enter it. The exclusion mask guarantees, for example, that tract delineated for the right side remains in its emisphere: the left side is excluded. To facilitate the detection of the landmarks we used color-coded FA maps in which red indicates that the principle eigenvectors point left-right, green indicates anterior-posterior, and blue indicates inferior-superior[52]. For the precentral gyrus, we used also a second, unconventional, modality to obtain the mask. We performed a grey matter segmentation of 3D-T1 images, using Freesurfer; it is an open source software suitable for processing

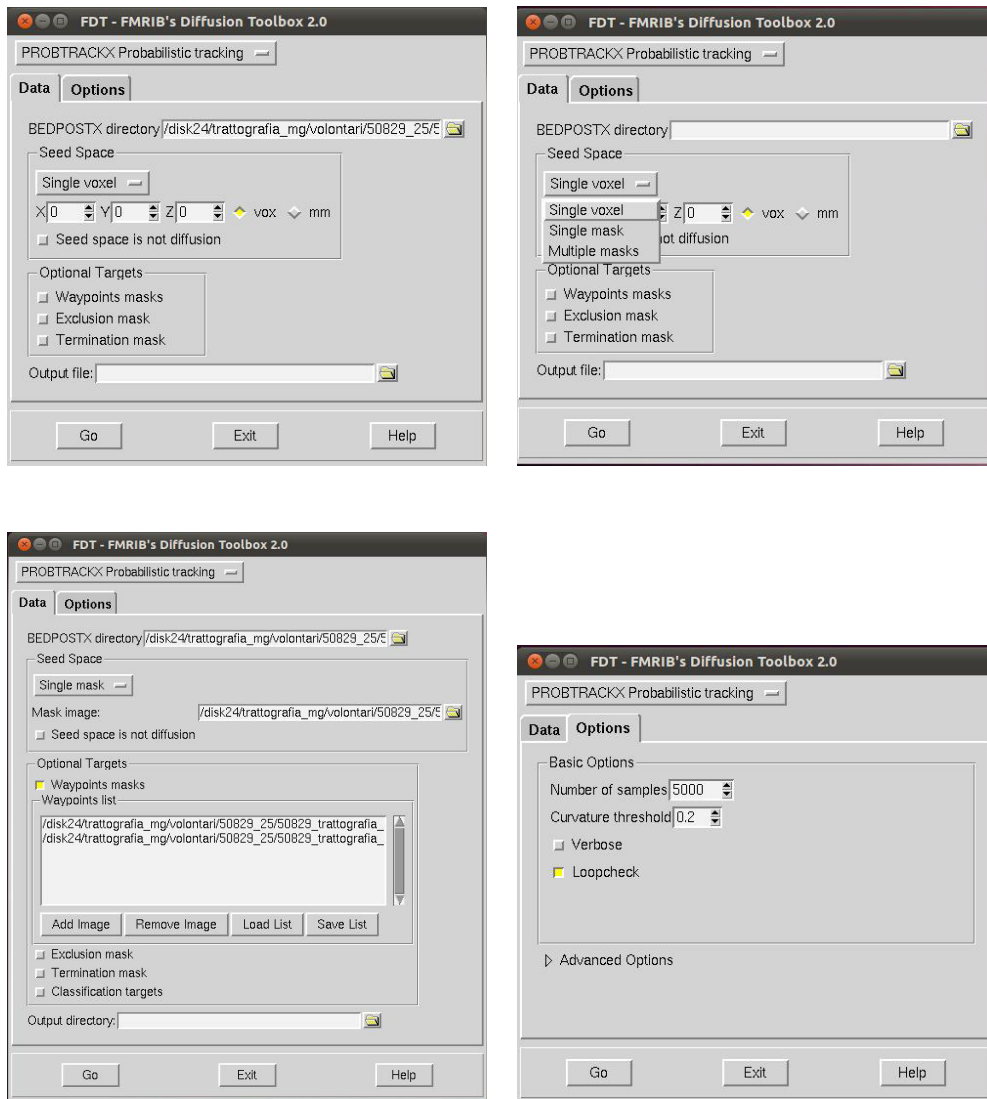


Figure 3.3: Grafical User Interface for FDT. The user can choose between Single Voxel, Single Mask or Multiple Mask and then he has to specify target masks. Some options are showed (at the bottom right). The curvature threshold indicates how sharply pathways can turn in order to exclude pathways. This number is the cosine of the minimum angle between two steps. *Loopcheck* is picked as we wanted to terminate pathways that loop back on themselves.

|                       | Cortical mask  |       |            |       |
|-----------------------|----------------|-------|------------|-------|
|                       | Manually drawn |       | Freesurfer |       |
|                       | right          | left  | right      | left  |
| Seed in pons mask     | 11652          | 6152  | 11709      | 7014  |
| Seed in cortical mask | 19348          | 24380 | 31295      | 50501 |

Table 3.3: Waytotal values for the specific healthy subject (N=1).

and analyzing brain data [53]. After obtaining the parcellation, masks of the precentral gyrus were registered to synthetic EPI created with *Uroboro2* (see Section 3.3) using the stored matrix  $T1_{tOD}TI$ . Masks were then subjected to the removing of zero pixels of the background. All the masks are shown in Figure 3.4.

The PROBTRACKX algorithm was applied combining setting options in various ways:

- Pons ROI as seed mask and manually drawn ROIs of the internal capsule and precentral gyrus as waypoint masks (see A in Figure 3.5);
- Manually drawn cortical mask as seed mask and ROIs located at the level of pons and internal capsule as waypoint masks (see B in Figure 3.5);
- Pons ROI as seed mask and ROIs of internal capsule and precentral gyrus (this latter obtained with Freesurfer) as waypoint masks (see C in Figure 3.5);
- Cortical mask obtained with Freesurfer segmentation as seed mask and ROIs located at the level of pons and internal capsule as waypoint masks (see D in Figure 3.5).

It was always used also the exclusion mask. We conducted a visual inspection of the obtained tracts and a comparison of the waytotal values. Results related to an healthy control (N=1) are reported in Table 3.3 and Figure 3.5.

Comparing A with C and B with D in Figure 3.5 it is evident, also at a visual inspection, that using a Freesurfer mask allows to obtain a tract with a greater volume: this result is emphasized in the entire sagittal view and focusing on the precentral gyrus in coronal views. The Freesurfer segmentation guarantees an accurate segmentation and

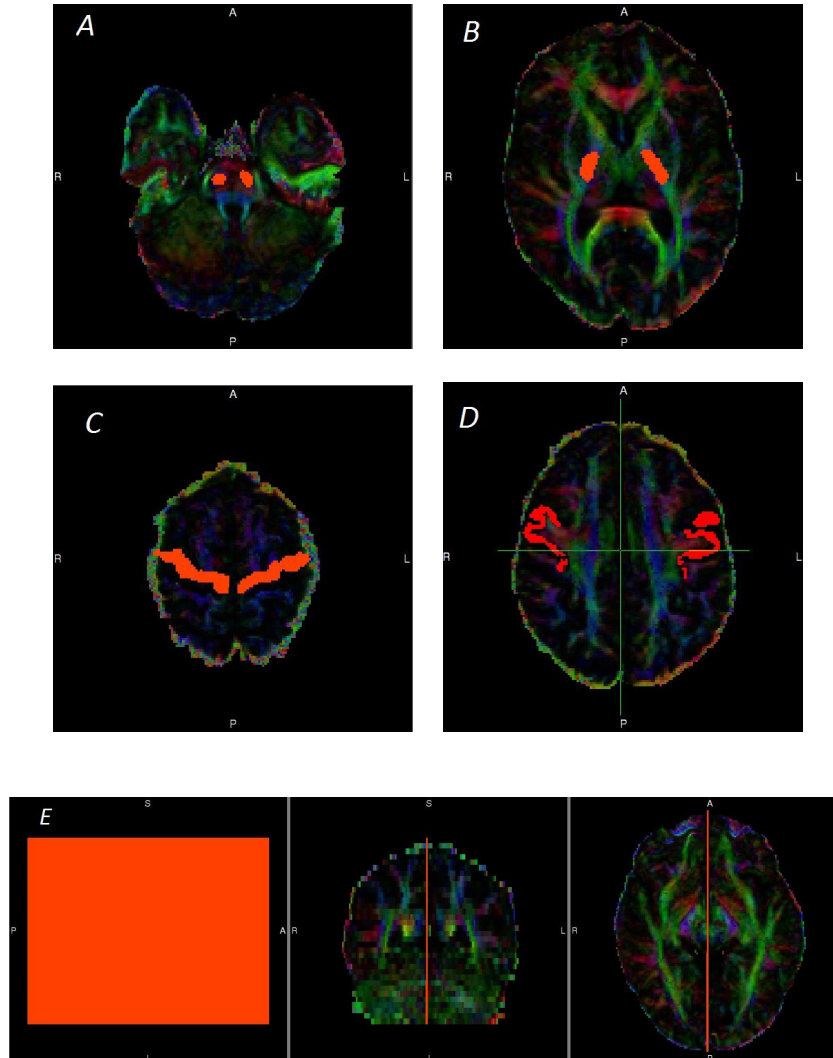
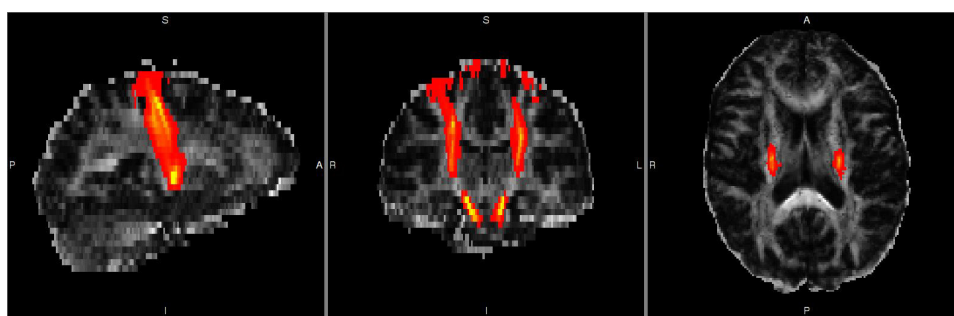
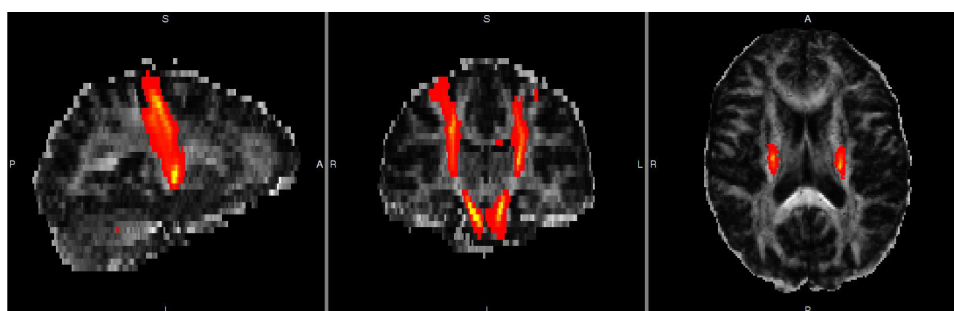


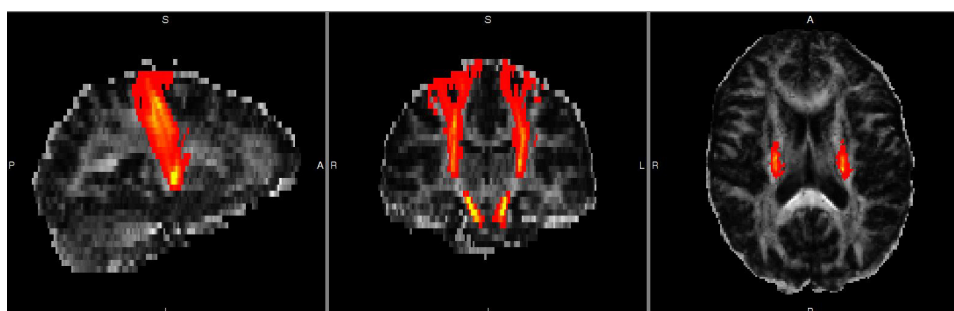
Figure 3.4: Axial views of the ROIs. Mask at the level of the pons (A), posterior limb of internal capsule (B), manually drawn precentral gyrus (C) and obtained with Freesurfer(D) are reported. Sagittal, coronal and axial views of the exclusion mask are shown in (E).



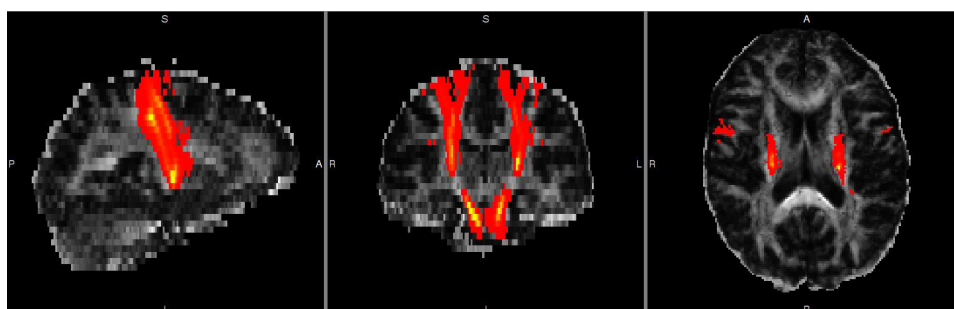
A. Seed mask: pons - one waypoint: manually drawn cortical mask



B. Seed mask: the manually drawn cortical mask



C. Seed mask: pons - one waypoint: Freesurfer cortical mask



D. Seed mask: Freesurfer cortical mask.

Figure 3.5: Sagittal, coronal and axial views of tracts obtained with various setting options of PROBTRACKX for one healthy subject (N=1).

waytotal values confirmed considerations of visual inspections, showing an higher number of detected fibers, in areas anatomically corresponding to the corticospinal bundle, using Freesurfer mask ( in the left side of brain the number is doubled). Furthermore, in order to define the best starting point, we compared waypoint values obtained with seed located at the level of the precentral gyrus with the other at the level of pons. The best results reached using the first option are validated by visual inspection; indeed, comparing C and D, it can be noted that, in the latter case, more white matter is detected at the level of the precentral gyrus (shown in axial view of D). This is probably due to the fact that we used masks with different size: the smaller the seed ROI is, the lower the number of samples drawn at the beginning will be (and the lower the resulting waytotal will be).

Finally, we decided to delineate CST for all subjects using a Freesurfer cortical mask as seed mask and ROIs located at the level of posterior limb of the internal capsule and of the pons as waypoint masks. Setting the starting point in the cortical areas also reflects the physiological direction of the white matter fibers. Moreover Freesurfer allows an automatic subject-specific segmentation and this procedure is more reliable with respect to a manually drawn mask. In addition, it is an original element of this work since to our knowledge in literature there are not any other studies that use Freesurfer cortical parcellation to reconstruct CST with a probabilistic tractography algorithm.

### **FA template**

In the previous stage of the work we delineated tracts in only four subjects. In order to determine a reproducible method also for the entire group of subjects, it is essential to develop an automatic process of ROIs definition. To do this, we created an FA template, a standardized space representative of FA maps of all subjects, on which we drew ROIs of interest. For this purpose, we used part of the TBSS algorithm (Tract-Based Spatial Statistics,[55]), developed to carry out voxelwise statistical analysis of the FA data. Briefly, TBSS projects all subjects' FA data onto a mean common space used to create a mean FA skeleton, which represents the centres of all tracts common to the group, in order to perform voxelwise cross-subject statistics. We were interested in creation of mean FA image, therefore we used only the first part of this algorithm. TBSS runs a nonlinear registration with FNIRT tool for nonlinear registration), aligning FA images

of healthy controls with 25 NDGD to a  $1 \times 1 \times 1$  mm standard space. To do this, it is necessary to individuate the target image for the registration, that can either be a pre-defined target<sup>2</sup>, or can be chosen to be the most representative subject in the study. We decided to use the latter option: every FA image is aligned to every other one, the most representative one is identified and used as the target image. TBSS is able to choose this image since it takes each FA image in turn and calculates the average number of nonlinear transformations necessary to align all other images to it; the one that has the smallest number of average warping is used as target. In our study, the subject corresponding to  $N=14$  coincides with the target image. This target image is then aligned into MNI152 standard space using an affine transformation, and every image is transformed into  $1 \times 1 \times 1$  mm atlas space combining the nonlinear transformation to the target FA image with the affine transform from the target to MNI152 space[56]. In this way, we obtained the transformation of subject's FA image into the MNI152 space. At this point, TBSS created the mean of all standard-space version of each subject's FA image acquired with 25 direction of diffusion gradient. In Figure 3.6 the mean FA template is reported.

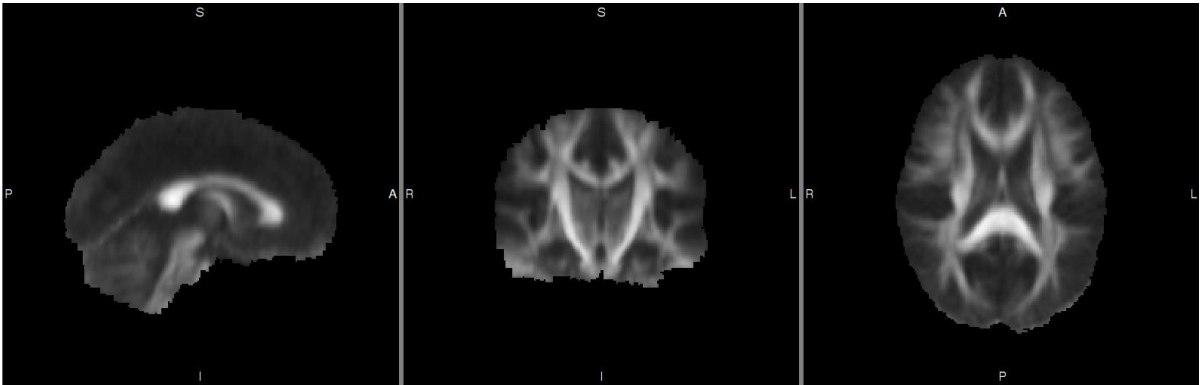


Figure 3.6: Mean FA template.

ROIs of the pons, posterior limb of the internal capsule and exclusion were drawn on the mean FA template, in collaboration with neurologists working at DIBINEM (see

<sup>2</sup>The pre-defined target image recommended by FSL (known as FMRIB58\_FA) is a high-resolution average of 58 well-aligned good quality FA images from Healthy male and female subjects aged between 20-50 ([www.http://fsl.fmrib.ox.ac.uk/fsl/fsl4.0/tbss/FMRIB58\\_FA.html](http://fsl.fmrib.ox.ac.uk/fsl/fsl4.0/tbss/FMRIB58_FA.html)).

Figure 3.7). Using the inverse of the transformation obtained with TBSS, we transferred back ROIs to the original FA maps at 25 directions. As the Freesurfer cortical parcellation had been previously registered to the space of 25 NDGD, we could delineate tract for the two sides of brain of each subject with FDT algorithm. In order to reconstruct CST also for images obtained with 64 NDGD, we applied the inverse transformation of linear registration performed in the earlier stage (inverse matrix of *64to25.mat*) to all ROIs and to Freesurfer parcellation. In this way, we determined a process partially independent from the operator and less susceptible to errors. It is important to specify, as highlighted by Thottakara et al. [57], that nearest neighbor interpolation has been used for every spatial transformation, in order to maintain ROIs intact.

## 3.5 Data analysis

### 3.5.1 State of art

To date, the large majority of the tractography analysis is conducted with a simple tract-averaged methodology. Therefore, the current approach is to average diffusion metrics for the entire fiber tracts, with a single mean and to estimate variance for each subject. As emphasized by Colby et al. [58], this method is not appropriate to detect the local changes of the diffusion properties along the tract because it ignores the rich anatomical variation. This can be understood observing the Figure 3.8, that explains how FA varies across the white matter. It assumes very low values (below 0.2) at the transition to the gray matter and very high values (above 0.8) in coherently dense white matter areas. Generally, using tract-average analysis, mean FA is estimated to assume values between 0.4 and 0.6. It is evident that potentially important information are lost.

We also have to considerate that great biological variation of the brain and complex fiber geometries, like crossing fibers, can locally alterate the FA measures. Moreover, a great detailed within-tract study can facilitate the comparison of results with similar voxel-based studies, like those conducted with TBSS. For all these reasons, methods of parameterization have been introduced to estimate diffusion properties within-subject and compare with a high precision the results between different groups. Few interesting studies focus on parameterization of the tract, subdividing it into segments and analyzing each of these parts individually [59] [60] [61]. Lin et al., for example, realizes an along-tract analysis of pyramidal tract (PYT) of relapsing neuromyelitis optica (RNMO)

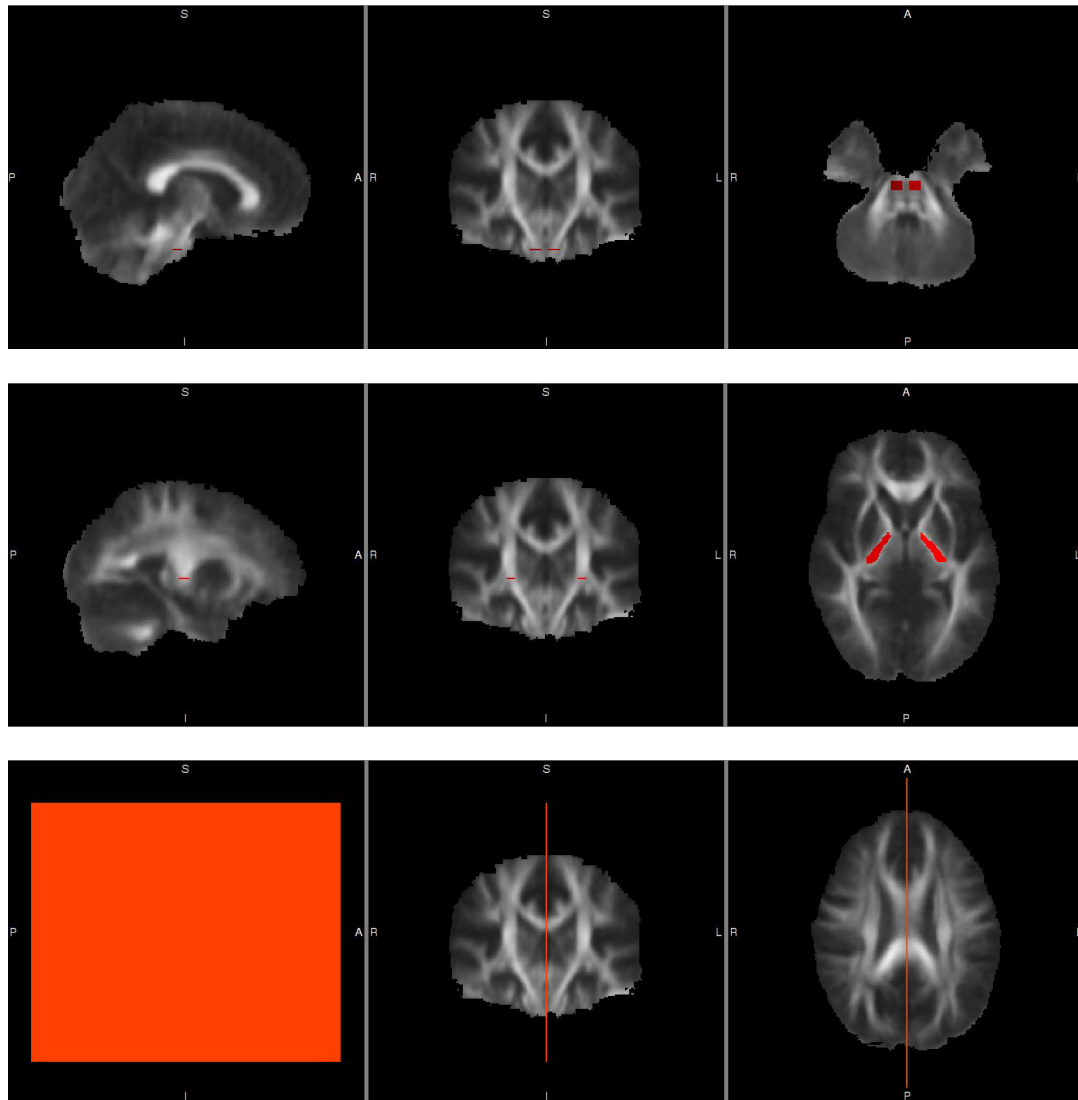


Figure 3.7: Sagittal, coronal and axial views of ROIs drawn on FA template. From the top, pons mask, internal capsule mask and exclusion mask are reported.

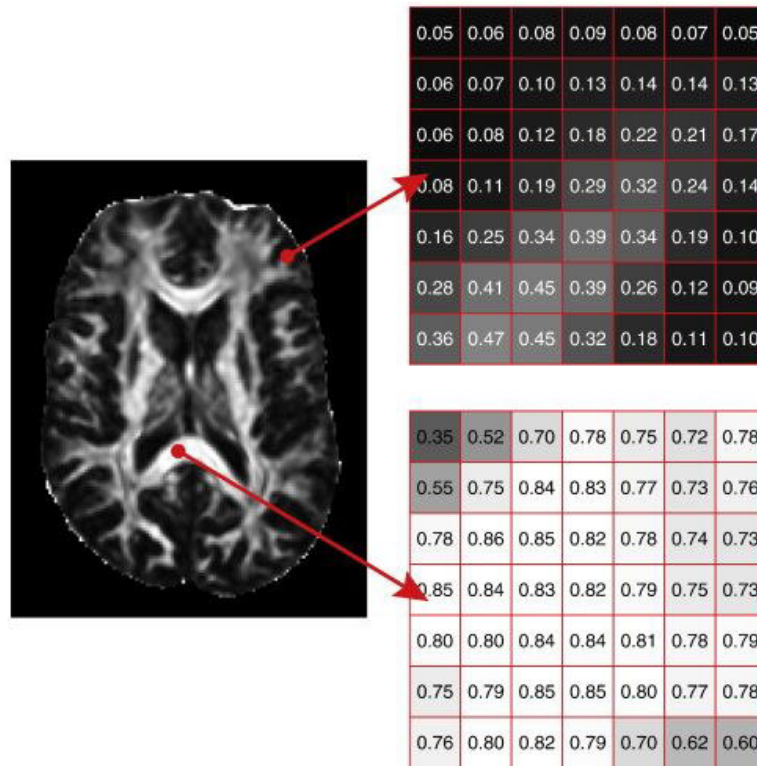


Figure 3.8: FA variations through the white matter. Top panel shows FA values at the transition to gray matter near the cortex while bottom panel focuses on values in coherent areas like the corpus callosum. *Image is taken from Colby et al. [58]*.

patients without brain lesions. They divide the tract into a certain number of segments, to compare diffusion metrics on each segment across subjects; however, the study reported several limitations due to crossing fibers and poor resolution of echo planar images. On the other hand, the study of Oh et al. suggests a static analysis of inter- and intra-subject variability along the tract, obtained with a deterministic algorithm and previously divided into 100 equal segments. In our study, we used a similar procedure implemented on CST delineated with probabilistic tractography.

### 3.5.2 Parameterization

Once corticospinal tracts were extracted, for each subject with 25 and 64 directions of diffusion gradient, we performed measurements on FA, MD and connectivity values. An overall aim of this work was to create a reliable standard process of tract-analysis, in order to obtain regional information along the length of the tract and conduct a within and between subjects analysis. This will be an important point for future valuations on patients, since the process will allow along-tract comparisons.

The first step was the thresholding of the obtained tract: we included in the further analyses only those voxels that are crossed by an established percentage of the total samples sent out from the seed mask. It is important to be sure of thresholding out the same proportion of voxels in all subjects. For this reason, the cropped tract of the right side was normalized by dividing values of connectivity by the total number of samples sent out (*waytotal* number) from the right side seed mask; the same process was applied to the left side. Normalization is useful for intersubject comparisons because it helps to deal with problems that arise when tracking performs very differently across different brains, sessions, or hemispheres [62]. We chose a threshold value of  $5 * 10^{-5}$  on images acquired with 25-NDGD; this threshold canceled few voxels, since we observed that a higher value counted out too many voxels at the risk of losing important information. On the other hand, images obtained with 64 NDGD were thresholded with a value of  $2.5 * 10^{-4}$ , higher with respect to the previous one because with a 64 directions the probabilistic algorithm intercepted other white matter bundles.

A visual inspection of reconstructed tracts, in different subjects, showed that the CST did not stop at the level of pons but wrongly flowed in cerebellum. This performance is likely due to the fact that other white matter, that is not part of corticospinal tract, is detected in cerebellum. Therefore, we decided to consider only the section of the bundle we were interested in: from the precentral gyrus to the pons. For this reason, we cut the excess, after having identified, for each subject, pons coordinates. To assure a perfect correspondence between reconstructed tract and underlying space, also FA and MD maps were cut with the same method. Figures 3.9 and 3.10 show original tract, the thresholded one and the final cut referred to subject N=3.

For both sides of brain, each tract in each subject was divided into 100 segments of

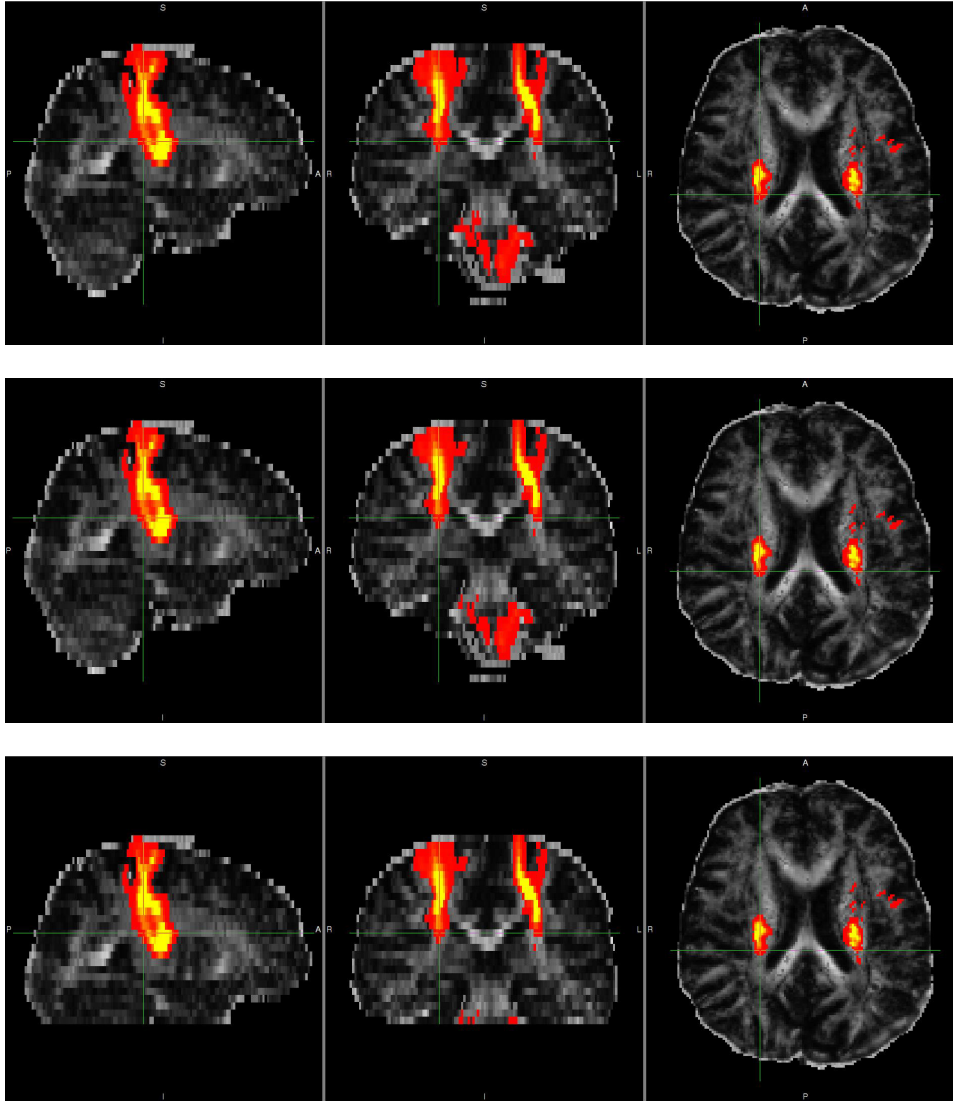


Figure 3.9: CST delineated in subject N=3, with 25 directions of diffusion gradient. From the top: original tract, thresholded tract, cropped tract.

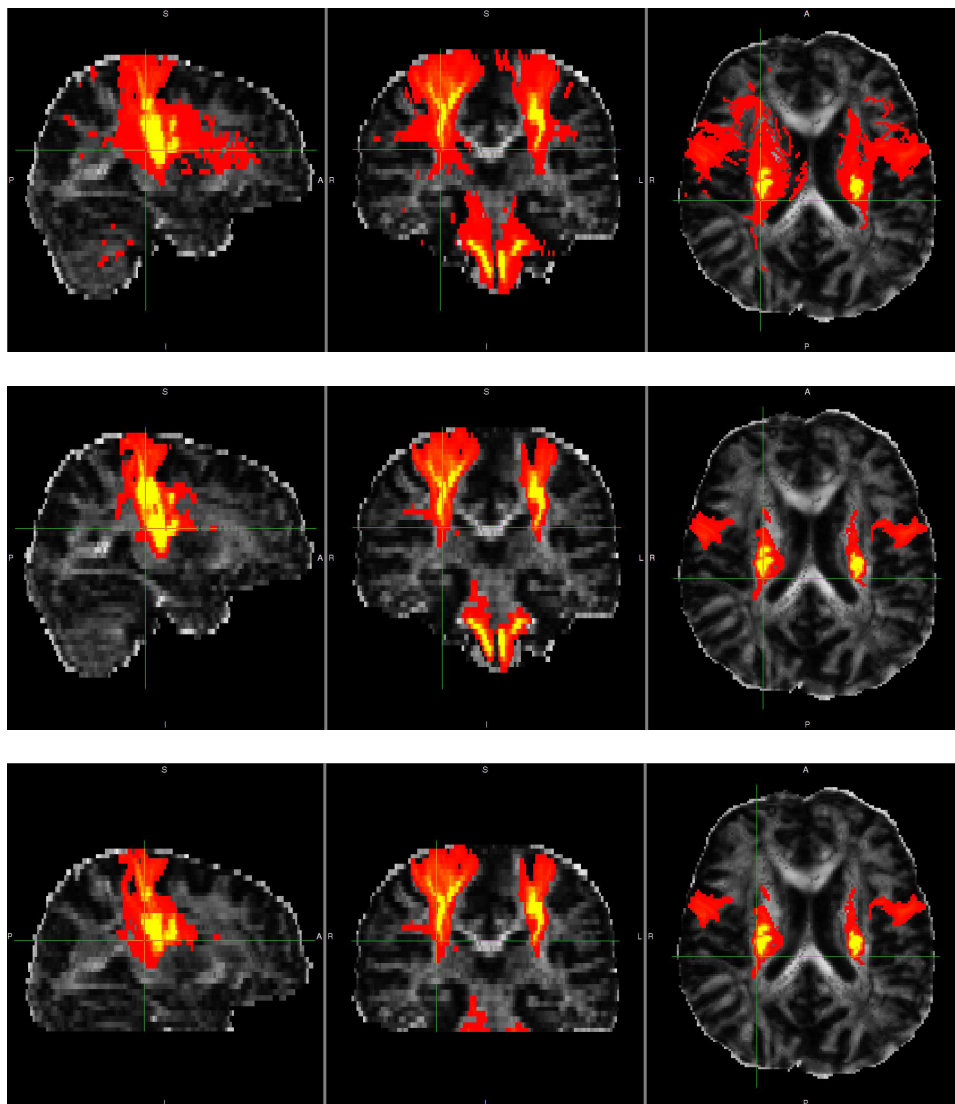


Figure 3.10: CST delineated in subject N=3, with 64 directions of diffusion gradient. From the top: original tract, thresholded tract, cropped tract.

equal length ( *percentiles*) from the pons to the precentral gyrus. To do this, we created a synthetic empty image characterized by the same dimension along x and y axis with respect to the original *fdt\_paths* image while the dimension along z axis was equal to 100. The in-plane resolution remained unvaried, but the resolution along z is calculated considering the different resolutions for the two NDGD: we calculated it as  $\frac{N_{cut} * r}{100}$ , where  $N_{cut}$  is the number of slices between pons and precentral gyrus in the original image and r is resolution along z axis (4 mm for 25-NDGD and 3 mm for 64-NDGD, see Table 3.2). This image was used to re-sample images in percentiles: we performed an affine linear registration of cropped FA, MD and *fdt\_paths* to the synthetic image, using an identity matrix of transformation. We referred to these new maps as *FA\_synt*, *MD\_synt*, *fdt\_synt*. The tract on FA map at different percentiles is shown in Figure 3.11.

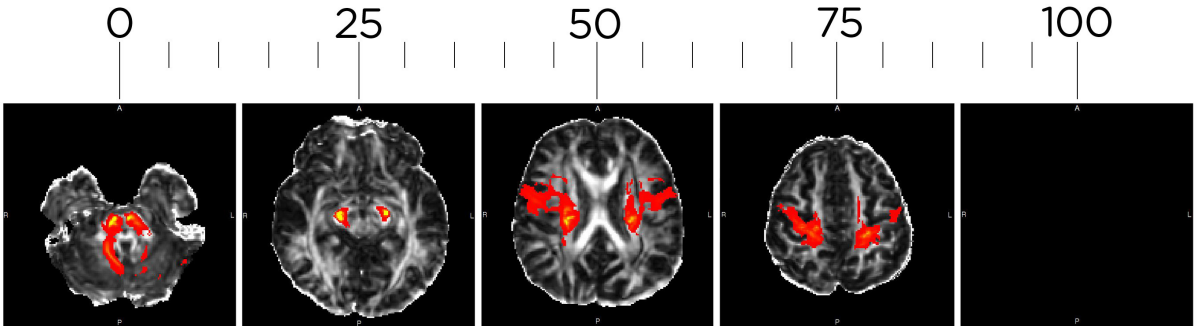


Figure 3.11: CST delineated with 64-NDGD is shown at different percentiles in subject N=3.

At this point, we used the result of registration of *fdt\_paths* to synthetic image, to mask *FA\_synt* and *MD\_synt*: in this way we had information regarding FA and MD values along the CST. We specifically divided each tract in 100 segments. Finally, we proceeded to calculate the median value of FA, MD and connectivity for each percentile; we chose median value instead of mean value, since we observed randomly that the distribution of FA, MD and connectivity distribution values along the segment had a non Gaussian distribution .

In a following step, after the previous statistical analysis, we considered necessary to perform the same analysis done for FA, MD and connectivity also for  $\lambda_1$ ,  $\lambda_2$ ,  $\lambda_3$ , RA, *mean\_f1* and *mean\_f2* indices, in order to deeply understand and validate some significant results.

The entire procedure was implemented in a bash script that automatically runs all the steps of registration and parameterization for the two acquisitions at different NDGD for each subject.

### 3.5.3 Statistical analysis

Intrasubject and intersubject variability were compared using the method proposed by Oh et al. [61]. We calculated two sets of variance: intrasubject (across-location) variances and intersubject (across-subject) variances. To evaluate intrasubject variability, we considered mean and variance ("intra-subject variance") of each parameter of interest for each subject:

$$\bar{F}_i = \sum_{s=1}^{100} F_i(s)/100 \quad (3.1)$$

$$\text{var}(F_i) = \sum_{s=1}^{100} [F_i(s) - \bar{F}_i]^2 / 100 \quad (3.2)$$

where  $s$  specifies the location in the 100 bin-parameterized tract and  $F_i(s)$  indicates the corresponding parameter for the  $i$ th subject.

To evaluate instead intersubject variability, we considered mean and variance ("inter-subject variance") of each parameter for each location:

$$\bar{F}(s) = \sum_{i=1}^{N_s} F_i(s)/N_s \quad (3.3)$$

$$\text{var}(F(s)) = \sum_{i=1}^{N_s} [F_i(s) - \bar{F}(s)]^2 / N_s \quad (3.4)$$

where  $N_s$  is the number of subjects examined.

All statistical analyses were conducted with SPSS (Statistical Package for the Social Sciences, version 21) and MATLAB (version 7.11).

First, to test if there were any significant differences between intrasubject and intersubject variances we performed the Mann-Whitney U-test for FA, MD and connectivity. Furthermore, we considered also cropped non-normalized and non-thresholded values

of connectivity distribution to understand the effect of the normalization using the way-total number. At this point, a correction to reduce the number of false positives is necessary. We chose to apply the Bonferroni correction, where the significance level is divided by the product of factors considered in the analysis. Dividing p-value by four (2 sides of brain x 2 NDGD) we obtained a new significance level value of 0.0125.

We employed two-ways repeated measures analysis of variance (RMANOVA), to determine side and NDGD effect on FA, MD, connectivity, cropped non-normalized and non-thresholded connectivity and waytotal. We previously performed the normality test, namely Kolmogorov-Smirnov test, to figure out if metrics of interest were normally distributed or not.

Since we noticed some significative differences (see Section 4.2.2), we performed paired t-test along the parameterized tracts for each subject, to individuate region-specific differences, focusing the study on side and NDGD differences. For *FA\_synt\_mask*, *MD\_synt\_mask* and *fdt\_synt* metrics we analyzed the following effects:

- side effect (right and left) on 25-NDGD;
- side effect (right and left) on 64-NDGD;
- NDGD effect (25- and 64-) on right side;
- NDGD effect (25- and 63-) on left side.

For each metric and each percentile of the coupled options, we performed a paired t-tests (1200 t-test in total). The False Discovery Rate method for multiple comparison correction was applied, less stringent than Bonferroni correction.

In order to understand some significant differences between specific percentiles, we performed paired t-test also on  $\lambda_1$ ,  $\lambda_2$ ,  $\lambda_3$ , RA and *mean\_f1* and *mean\_f2* values. Since we wanted to estimate the volume of the detected second fiber (if present), we added to the process the measurement of the volume of *mean\_f1* and *mean\_f2* for each percentile. Finally, we chose to investigate the spatial correlation between tracts with 25- and 64-NDGD. We considered the coordinates of the Centre of Gravity (COG) for the binarized tract. COG is an average of the coordinates (a concept that recalls the centre of gravity for an object with distributed mass). We studied separately x and y coordinates. To obtain further information about spatial distribution of the tract, we created an image of the sum of tract volumes of all subject: to do this we binarized each tract,

we registered tracts to mean FA template and superimposed every tract on it. The intensity (in a range between 0 and 25, which is the number of subjects) of the global tract obtained revealed quantitative information about spatial distribution of the tract between subjects. Moreover, a 2D Pearson Correlation was performed for each subject considering binarized *fdt\_synt* image with both NDGD for right side and then for left side (we performed binarization assigning value of 1 to the voxel if the tract is present, 0 otherwise).

All t-test (with the FDR corrections) and the Pearson Correlation were implemented in a MATLAB environment using *ttest.m*, *fdr\_bh.m* and *corr2.m* functions.



# Chapter 4

## Results

### 4.1 CST reconstruction

We reconstructed the corticospinal tract in both sides of brain for all subjects, with 25-NDGD and 64-NDGD data. The obtained CSTs are shown in Figures 4.1, 4.2, 4.3. We report a sample of 3 subjects (N=2, N=3, N=4 of Table in Section 3.1), randomly chosen. Visual inspection revealed evident differences between tracts obtained with the two NDGDs.

### 4.2 Statistical analysis

In the following Figures distributions of median value of FA, MD and connectivity, for each side of brain and for each NDGD, are shown. At visual inspection, it can be noted that FA median values vary along the tract, but they do not change in a considerable way between different subjects; a slightly higher variability along tract can be noted with 64-NDGD with respect to distribution with 25-NDGD (see Figures 4.4 and 4.5). MD values are constant until the 85th percentile, and over this point values show a great variability along the final part of the tract; the same behaviour is observed with both NDGDs (see Figures 4.6 and 4.7). On the other hand, connectivity distribution is characterized by a great variability along the tract and across different subjects; with 64-NDGD it is evident a lower variability in the second half of the tract (see Figures 4.8 and 4.9).

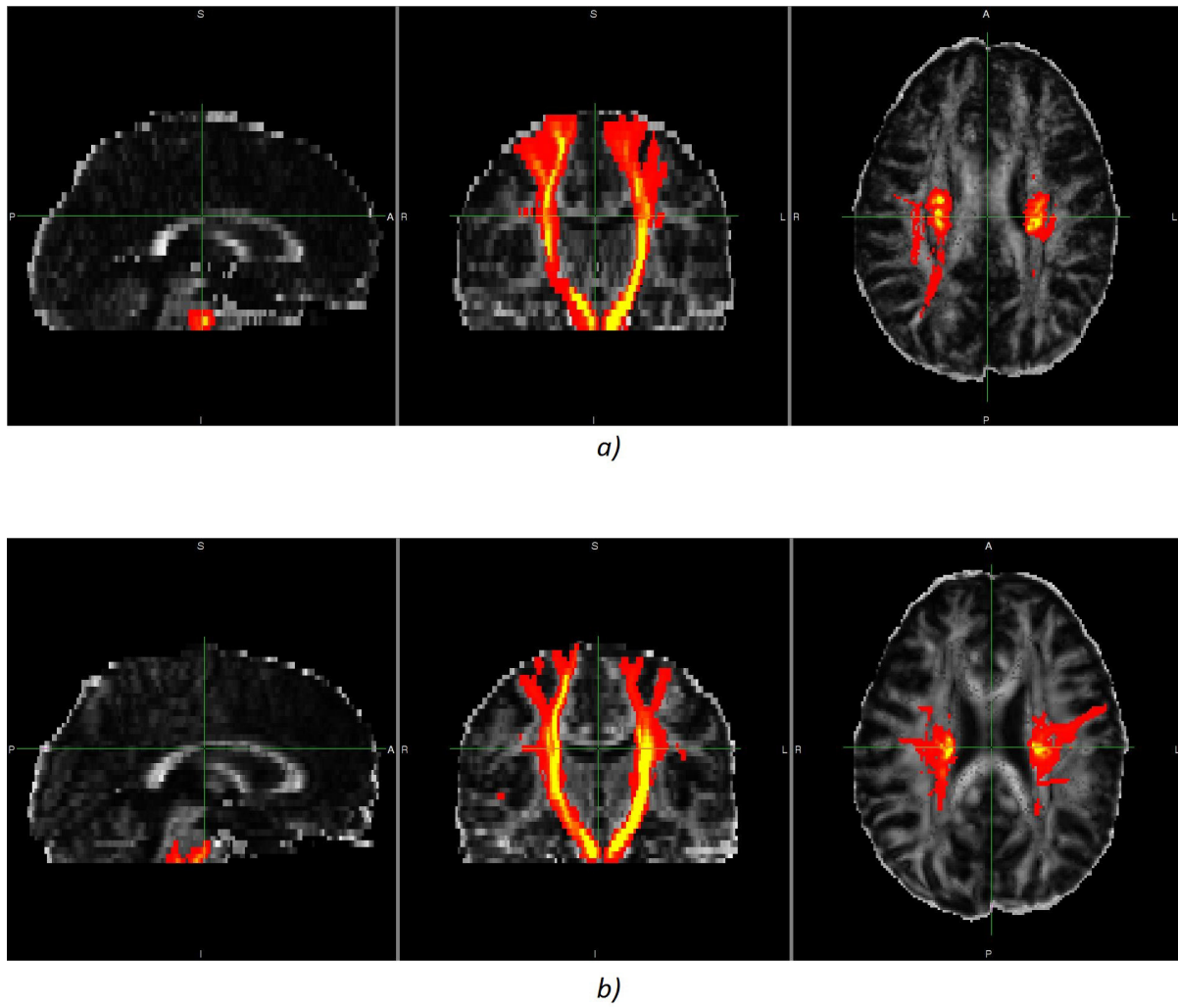
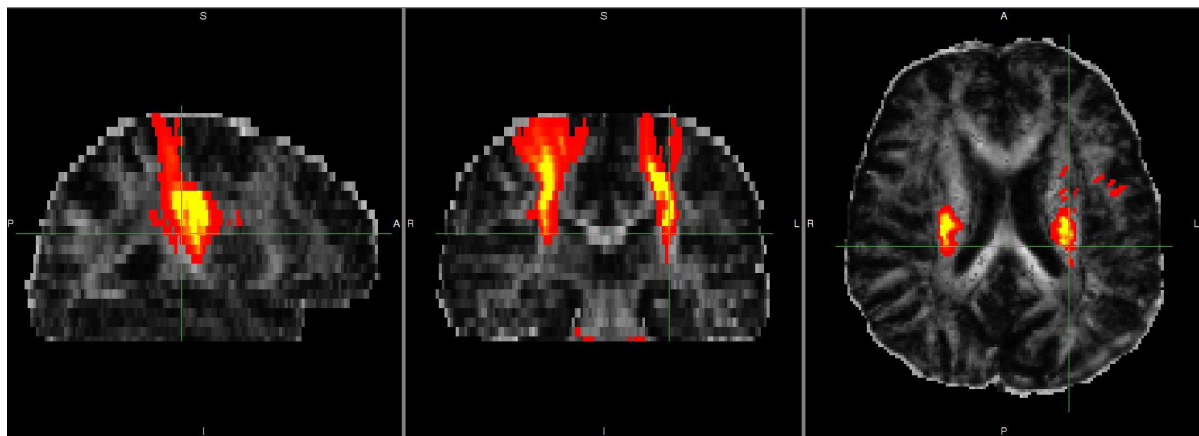
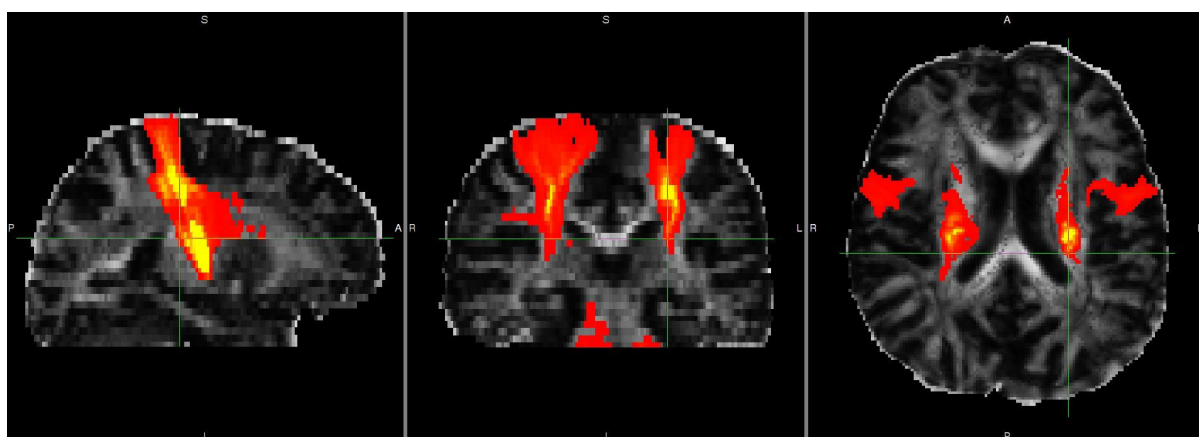


Figure 4.1: CST in subject N=2, with 25-NDGD (a) and 64-NDGD (b).



a)



b)

Figure 4.2: CST in subject N=3, with 25-NDGD (a) and 64-NDGD (b).

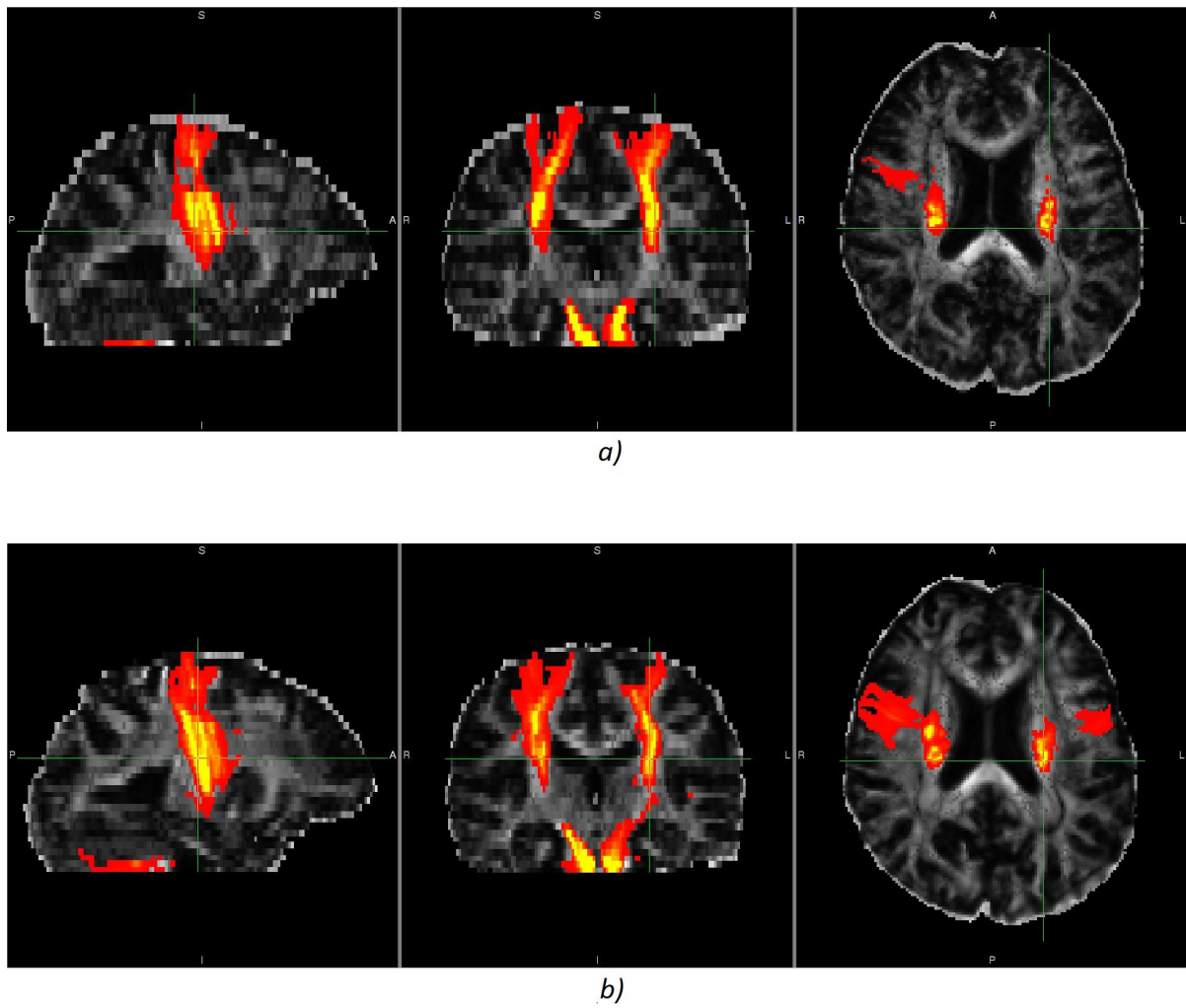


Figure 4.3: CST in subject N=4, with 25-NDGD (a) and 64-NDGD (b).

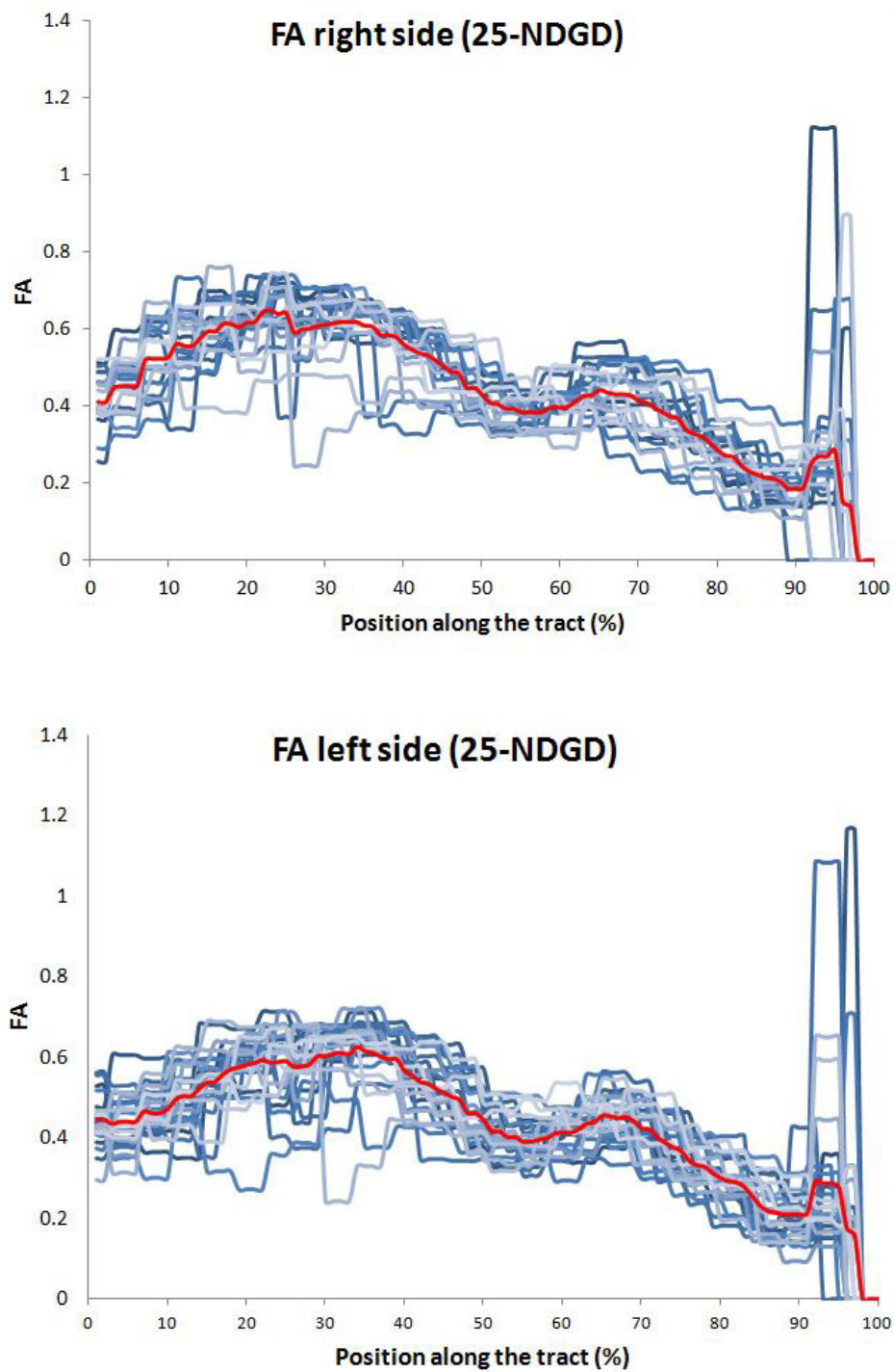


Figure 4.4: Plot of median value of FA with 25-NDGD for each percentile, in each subject (blu lines). Red line represents average values between subjects along the tract.

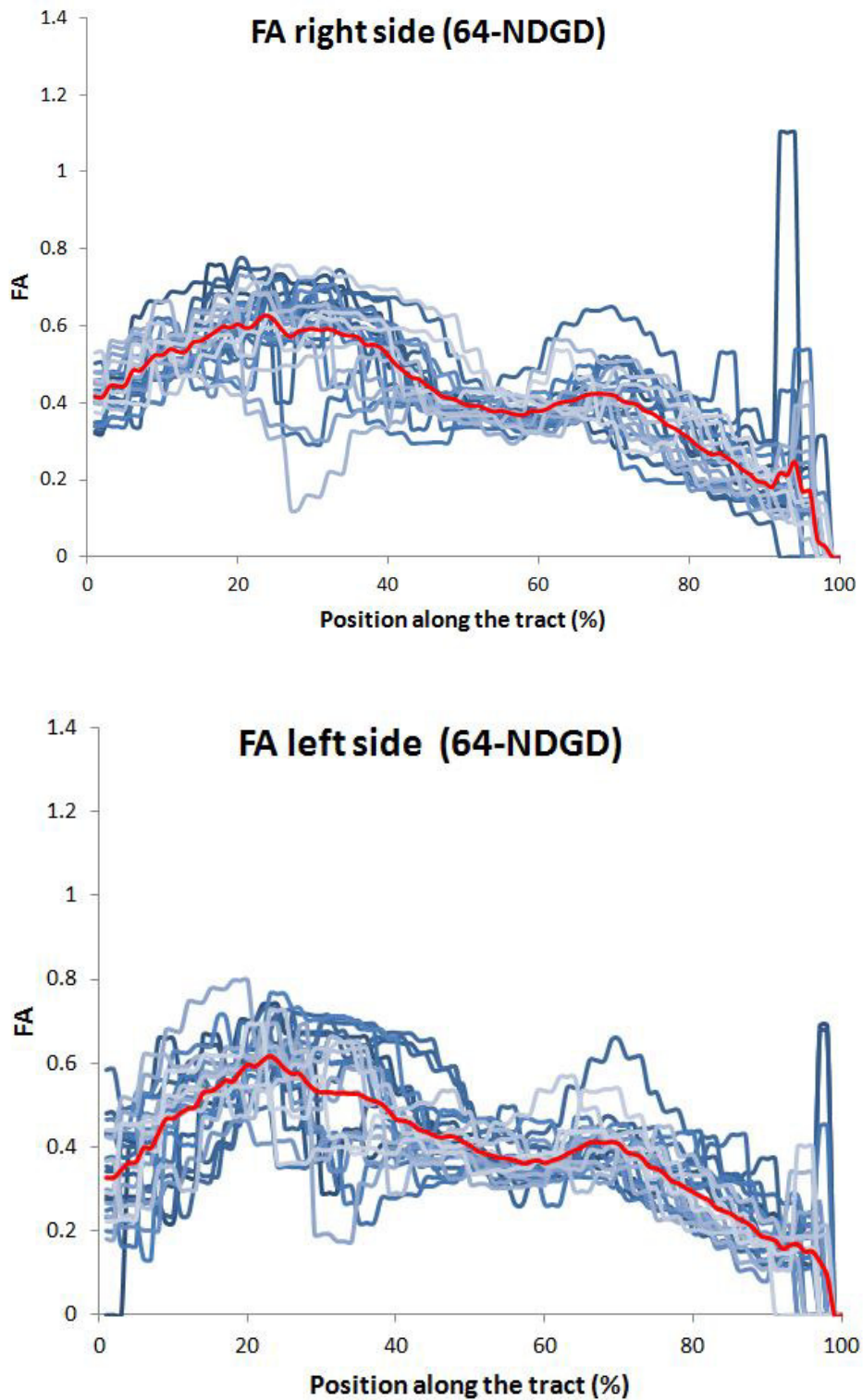


Figure 4.5: Plot of median value of FA with 64-NDGD for each percentile, in each subject (blue lines). Red line represents average values between subjects along the tract.

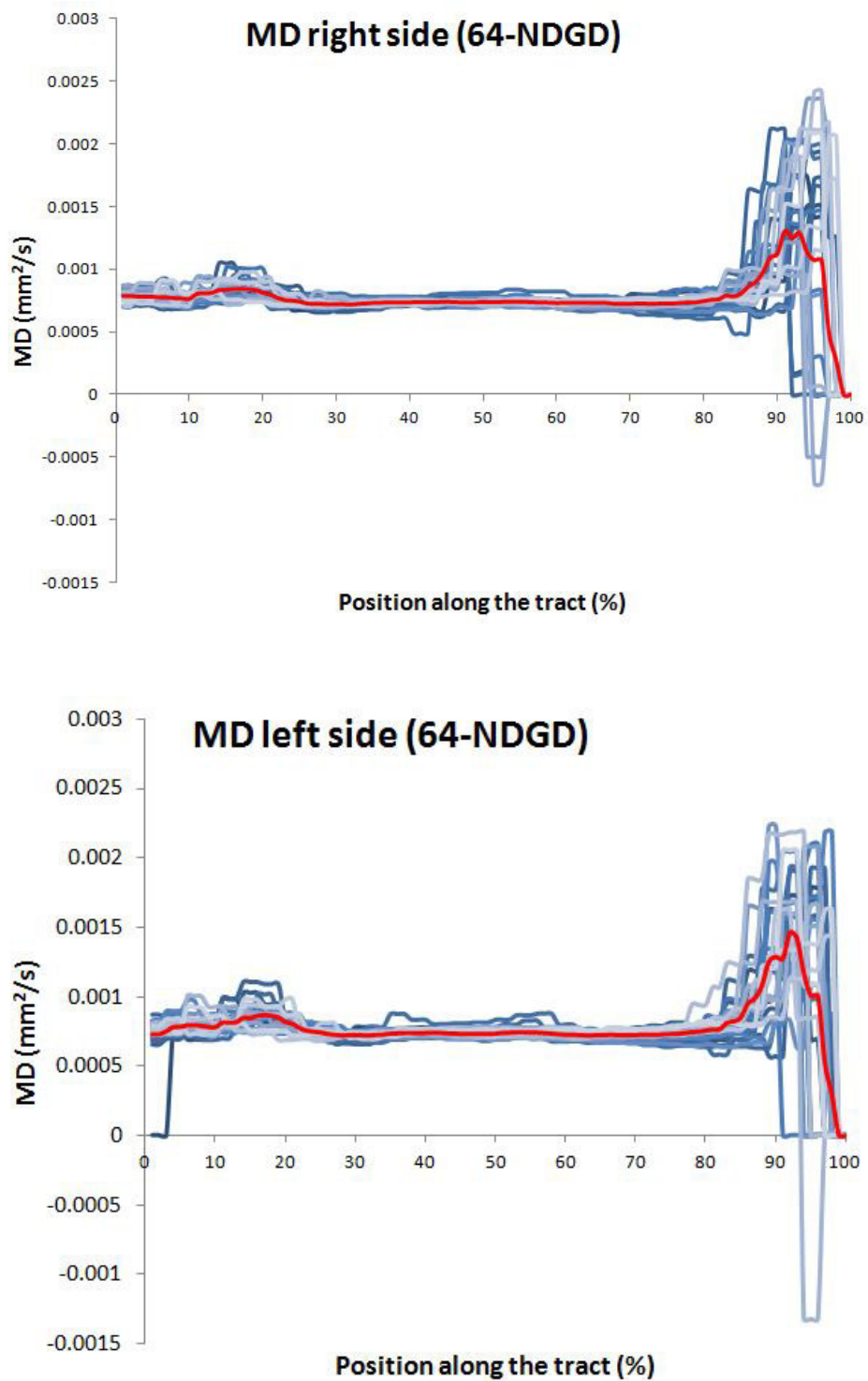


Figure 4.7: Plot of median value of MD with 64-NDGD for each percentile, in each subject (blue lines). Red line represents average values between subjects along the tract.

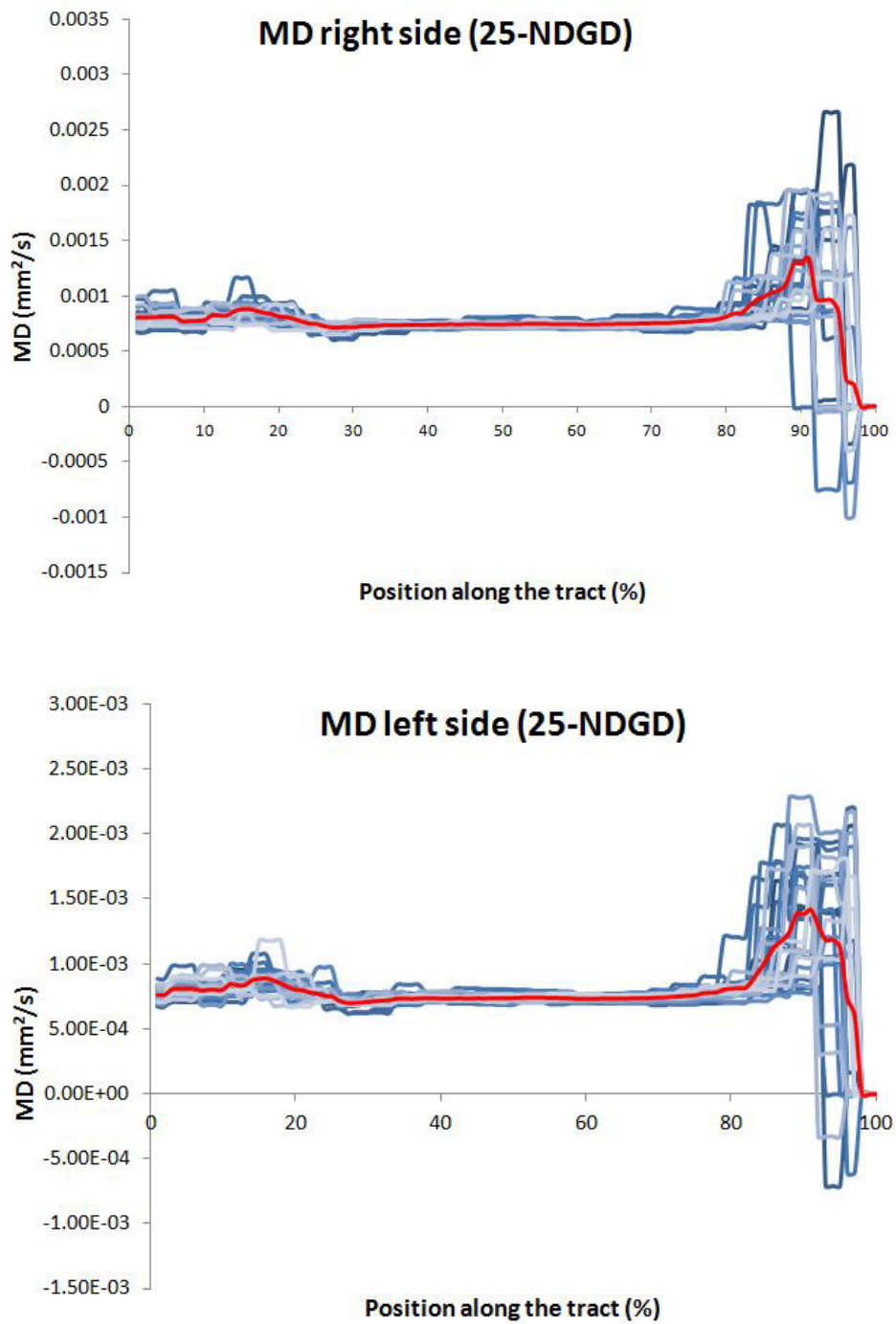


Figure 4.6: Plot of median value of MD with 25-NDGD for each percentile, in each subject (blue lines). Red line represents average values between subjects along the tract.

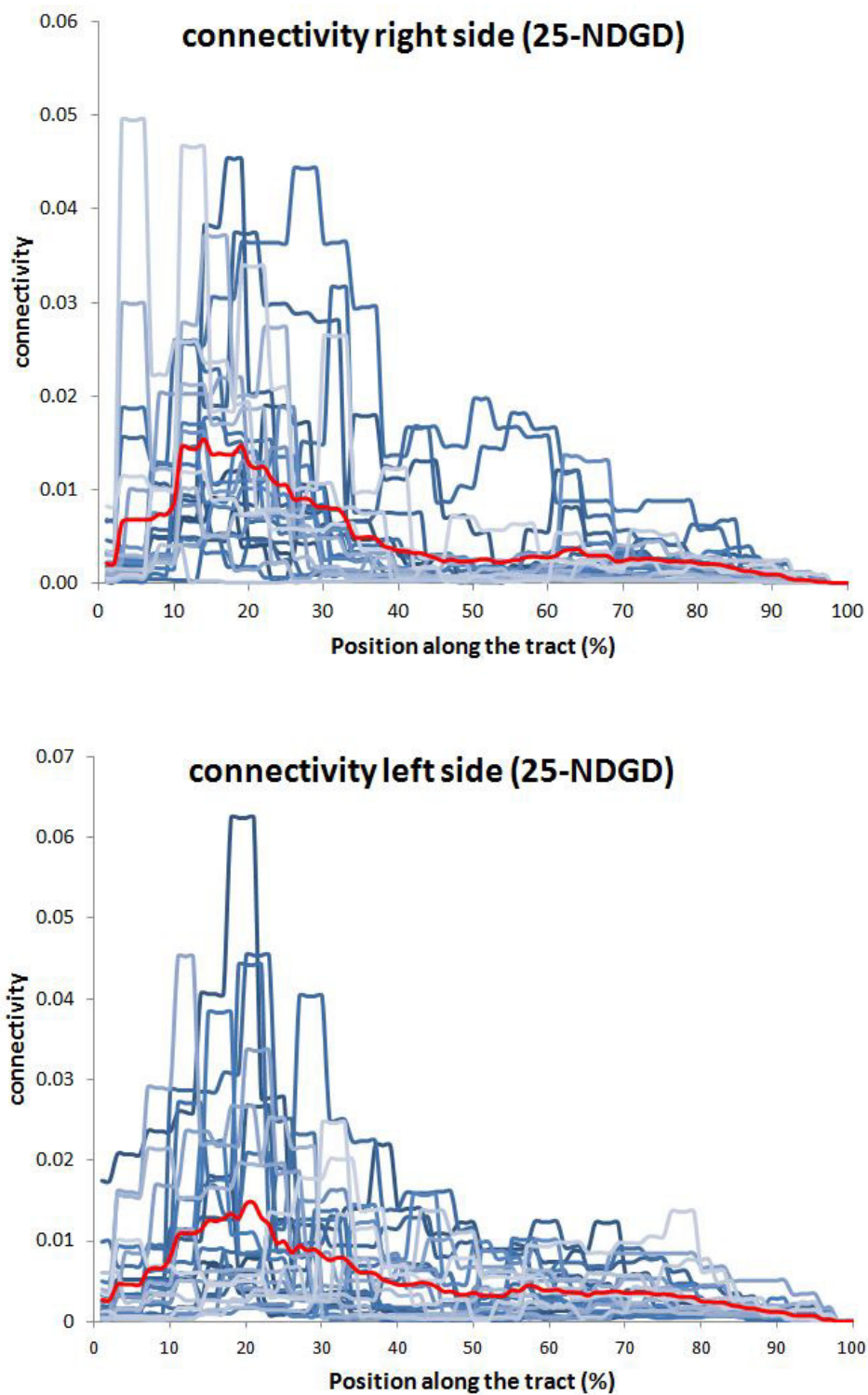


Figure 4.8: Plot of median value of connectivity with 25-NDGD for each percentile, in each subject (blu lines). Red line represents average values between subjects along the tract.

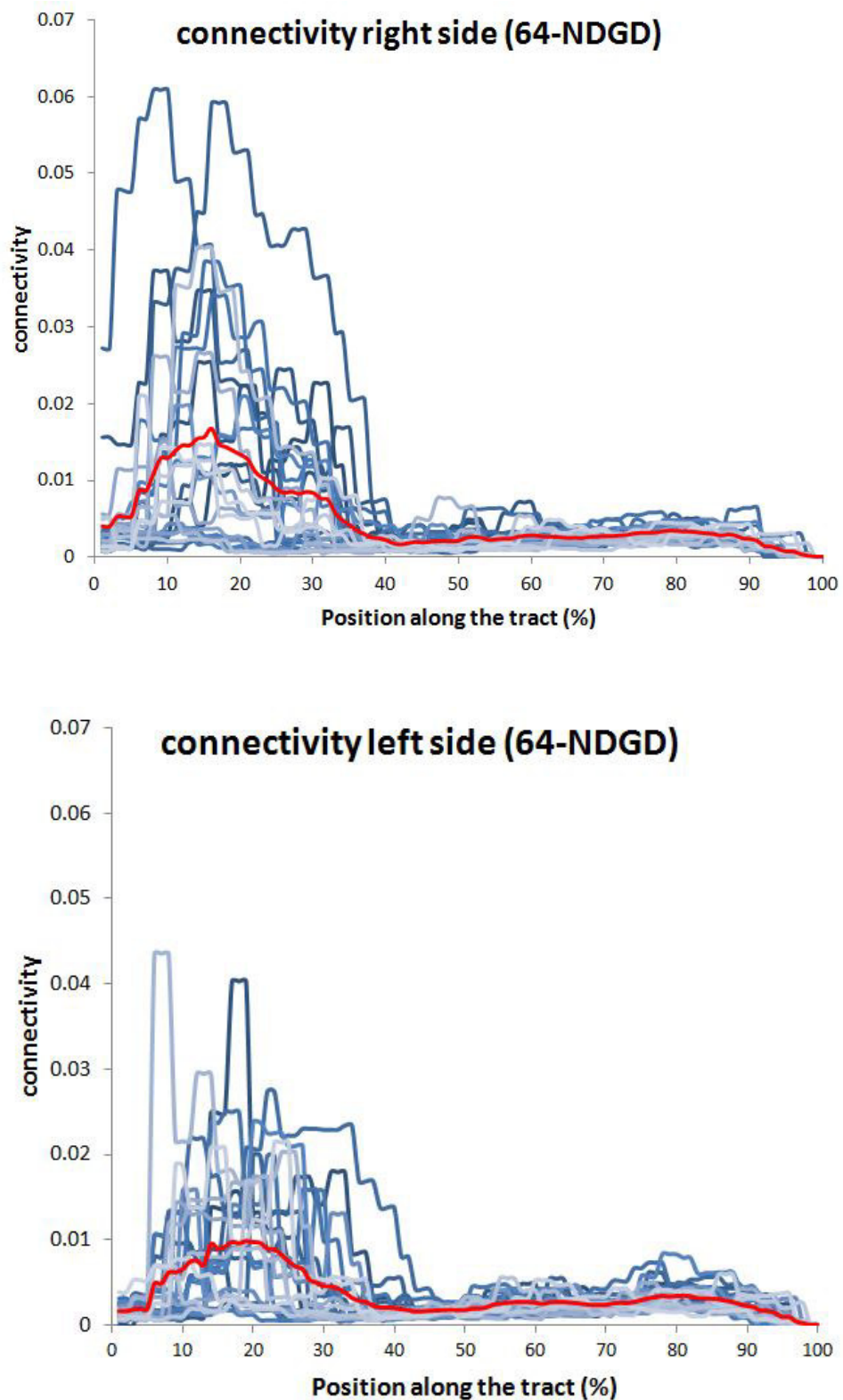


Figure 4.9: Plot of median value of connectivity with 64-NDGD for each percentile, in each subject (blu lines). Red line represents average values between subjects along the tract.

### 4.2.1 Intrsubject and intersubject variability

We firstly conducted analyses on FA, MD and connectivity values, considering intra- and inter-subject variability (Equations (3.2) and (3.4) in Section 3.5.3). In order to establish whether or not intrasubject variances were different from intersubject variances, we performed a Mann-Whitney test. In Table 4.1 side and NDGD significant main effects on metrics are reported. The Bonferroni method was used to correct for multiple comparisons (2 sides x 2 NDGD = 4 multiple comparisons); the new statistical significance level (0.0125) is considered as  $\frac{p}{m}$ , where m is number of tested hypotheses considered and p-value is fixed at 0.05.

| Indices      |         |       | Mann-Whitney statistics |               |               |
|--------------|---------|-------|-------------------------|---------------|---------------|
|              |         |       | <i>P</i> - values       | Intra-subject | Inter-subject |
| FA           | 25-NDGD | right | < <b>0.001</b>          | 107.12        | 51.97         |
|              |         | left  | < <b>0.001</b>          | 107.00        | 52.00         |
|              | 64-NDGD | right | < <b>0.001</b>          | 109.36        | 51.41         |
|              |         | left  | < <b>0.001</b>          | 109.12        | 51.47         |
| MD           | 25-NDGD | right | < <b>0.001</b>          | 101.52        | 53.37         |
|              |         | left  | < <b>0.001</b>          | 100.24        | 53.69         |
|              | 64-NDGD | right | < <b>0.001</b>          | 102.16        | 53.21         |
|              |         | left  | < <b>0.001</b>          | 100.88        | 53.53         |
| connectivity | 25-NDGD | right | 0.28                    | 70.04         | 61.24         |
|              |         | left  | 0.27                    | 70.16         | 61.21         |
|              | 64-NDGD | right | 0.02                    | 77.96         | 59.26         |
|              |         | left  | 0.02                    | 77.36         | 59.41         |

Table 4.1: Comparison between intra-subject variability and inter-subject variability of FA, MD and connectivity values. Mean ranks are reported.  $p < 0.0125$ , after Bonferroni correction. Significant results are reported in bold.

Intrasubject variances, for FA and MD values, resulted significantly higher than inter-subject ones. On the other hand, for connectivity values it was not noticed any significant

difference. To be sure that the latter result is not linked to the normalization, we did the same analysis on connectivity distribution before dividing by waytotal number and results are reported in Table 4.2. Again, the variances showed no differences.

|              |         |       | Mann-Whitney statistics |               |               |
|--------------|---------|-------|-------------------------|---------------|---------------|
| Indices      |         |       | <i>P</i> - values       | Intra-subject | Inter-subject |
| Connectivity | 25-NDGD | right | 0.19                    | 71.36         | 60.91         |
|              |         | left  | 0.69                    | 65.6          | 62.35         |
|              | 64-NDGD | right | 0.58                    | 66.56         | 62.11         |
|              |         | left  | 0.56                    | 66.76         | 62.06         |

Table 4.2: Comparison between intra-subject variability and inter-subject variability of connectivity before normalization.

#### 4.2.2 Side and number of diffusion gradient directions effects

In this part of the analysis, we considered FA, MD, connectivity distribution and waytotal. First we performed the non-parametric normality test of Kolmogorov- Smirnov to verify normality. FA, MD, non-normalized connectivity values and waytotal satisfied the null hypothesis of normality; connectivity values showed a non Gaussian distribution, but considering that few values drift from Gaussian distribution (data not shown) and the robustness of ANOVA under 20 degree of freedom, we evaluated all parameters performing a RMANOVA test. Results of RMANOVA test for side and NDGD, are reported in Tables 4.3, 4.4, 4.5, 4.6 and 4.7).

## A

|         | FA   | F     | P              |
|---------|------|-------|----------------|
| Effects | Side | 4.95  | <b>0.03</b>    |
|         | NDGD | 19.46 | < <b>0.001</b> |

## B

|      |    | Side  | Mean | Standard deviation |
|------|----|-------|------|--------------------|
| NDGD | 25 | Right | 0.43 | 0.04               |
|      |    | Left  | 0.43 | 0.03               |
|      | 64 | Right | 0.42 | 0.04               |
|      |    | Left  | 0.39 | 0.04               |

Table 4.3: A: side and NDGD significant main effects on FA values (significant results are reported in bold). B: descriptive statistics of FA.

We analyzed also non-normalized connectivity values (Table 4.6), to study the effect of normalization. We obtained significant differences for:

- FA values, considering different NDGDs and different sides of the brain;
- MD values, considering different sides;
- Non-normalized connectivity values for different NDGDs;
- Waytotal number for different NDGDs.

We observed no significant results for connectivity distribution, either for side or for NDGD.

## A

|         | MD   | F    | P            |
|---------|------|------|--------------|
| Effects | Side | 8.15 | <b>0.009</b> |
|         | NDGD | 1.18 | 0.288        |

## B

|      |    | Side  | Mean ( $\text{mm}^2/s$ ) | Standard deviation ( $\text{mm}^2/s$ ) |
|------|----|-------|--------------------------|--|
| NDGD | 25 | Right | $7.68 \cdot 10^{-3}$     | $4 \cdot 10^{-5}$                      |
|      |    | Left  | $7.96 \cdot 10^{-3}$     | $3 \cdot 10^{-5}$                      |
|      | 64 | Right | $7.67 \cdot 10^{-3}$     | $5 \cdot 10^{-5}$                      |
|      |    | Left  | $7.82 \cdot 10^{-3}$     | $4 \cdot 10^{-5}$                      |

Table 4.4: A: side and NDGD significant main effects on MD values (significant results are reported in bold). B: descriptive statistics of MD.

## A

|         | Connectivity | F    | P    |
|---------|--------------|------|------|
| Effects | Side         | 0.97 | 0.33 |
|         | NDGD         | 1.45 | 0.24 |

## B

|      |    | Side  | Mean  | Standard deviation |
|------|----|-------|-------|--------------------|
| NDGD | 25 | Right | 0.005 | 0.003              |
|      |    | Left  | 0.005 | 0.003              |
|      | 64 | Right | 0.005 | 0.003              |
|      |    | Left  | 0.004 | 0.002              |

Table 4.5: A: side and NDGD significant main effects on connectivity values. B: descriptive statistics of connectivity distribution.

## A

|         | Non-normalized connectivity | F     | P              |
|---------|-----------------------------|-------|----------------|
| Effects | Side                        | 0.16  | 0.69           |
|         | NDGD                        | 50.05 | < <b>0.001</b> |

## B

|      |    | Side  | Mean | Standard deviation |
|------|----|-------|------|--------------------|
| NDGD | 25 | Right | 36.7 | 25.5               |
|      |    | Left  | 45.3 | 27.2               |
|      | 64 | Right | 13.4 | 5.8                |
|      |    | Left  | 9.6  | 3.1                |

Table 4.6: A: side and NDGD significant main effects on non-normalized connectivity values (significant results are reported in bold). B: descriptive statistics of connectivity distribution.

## A

|         | Waytotal | F     | P              |
|---------|----------|-------|----------------|
| Effects | Side     | 0.60  | 0.44           |
|         | NDGD     | 49.46 | < <b>0.001</b> |

## B

|      |    | Side  | Mean  | Standard deviation |
|------|----|-------|-------|--------------------|
| NDGD | 25 | Right | 21484 | 21834              |
|      |    | Left  | 23420 | 19751              |
|      | 64 | Right | 98001 | 71799              |
|      |    | Left  | 89324 | 60429              |

Table 4.7: A: side and NDGD significant main effects on waytotal number (significant results in bold). B: descriptive statistics of waytotal.

### 4.2.3 Along-tract analysis

To determine region-specific differences between sides and NDGD, we performed paired t-test considering coupled parameters as explained previously in 4.2. First, we examined FA, MD and connectivity values of CST. Results are shown in Figures 4.10, 4.11 and 4.12. In each Figure, the first and the second panel from the top illustrate metric of interest distributions and differences between two NDGD (black line represents 25-, and grey line represents 64-) at fixed side (respectively right and left). Coloured segments represent significant differences at  $p < 0.05$  correcting using FDR: red line shows that values with 25-NDGD are higher than those with 64- and green line indicates the opposite. The last two panels illustrate differences between two sides (black line is the right side and grey line is the left side) at fixed NDGD (respectively 25 and 64). Red line shows that values in the right side are higher than in the left side and green line indicates the opposite. In our analysis, we considered not relevant differences concerning a number of consecutive percentiles lower than 3, since in that case we were under the spatial resolution of the original DWI data. Below, we list significant results:

- Considering FA metric at 25-NDGD, it was observed an increase in the right side from the 7th to 18th percentile, between the pons and the cerebral peduncle. Considering the same metric at 64-NDGD, the right side showed an increase from the 1st to the 7th percentile, at the level of the pons (Figure 4.10);
- Considering FA values for the right side, it was observed an increase at 25-NDGD values between 42nd and 51st segment, at the level of the posterior limb of the internal capsule. Fixing left side, FA values with 25 NDGD showed an increase along the central tract of the CST, from the 30th to the 65th percentile (Figure 4.10);
- Considering MD metric, it was observed in both sides at 25-NDGD an increase from 68th to 82st segment, in cortical sulci; on the other hand, no differences were observed between the two sides of brain at 25-and 64-NDGD (Figure 4.11);
- Considering the connectivity distribution, at the level of premotor cortex, it was observed that, in both sides, its values were higher at 64-NDGD; instead, no differences were observed between right and left side at fixed NDGD. (Figure 4.12).

To understand and explain significant results observed for FA, MD and connectivity, we performed the same analysis on  $\lambda_1$ ,  $\lambda_2$ ,  $\lambda_3$  and RA indices. Results are shown in Figures 4.13, 4.14, 4.15, 4.16.

#### 4.2.4 Spatial distribution of the tract

As outlined in section 4.2, we evaluated the 2D Pearson correlation coefficient of binarised tract, for both NDGD in each side of brain. As shown in Figure 4.17, we observed a global high level of correlation between tracts obtained with different NDGD ( $r$  between 0.5 and 0.7). Furthermore, the analysis revealed a drop of the spatial correlation in correspondence of posterior limb of the internal capsule (from about 30th to 50th percentile).

In order to investigate the spatial distribution of tracts volume, we superimposed each binarised tract to each other. We obtained, in this way, the images in Figure 4.18: intensity of the total tract varies from 1 to 25 (total number of subjects). Color legend indicates red for minimum value of intensity and yellow for maximum value.

Moreover, we performed a paired t-test for each percentile also for total volume and COG values, for x and y coordinates. Results are shown in Figures 4.19, 4.20 and 4.21. The color legend has been illustrated in Section 4.2.3.

#### 4.2.5 Crossing fibers analysis

Quantitative measures of the first and second fibers (where present) were conducted performing a paired t-test on mean.f1 and mean.f2 median values and mean.f1 and mean.f2 volume values (Figures 4.22 and 4.23): in this way we estimated how many voxels (and in which specific segment along the tract) were crossed by the second fiber. In particular, it can be noticed that for mean.f2 volume, measures obtained with 64-NDGD are always characterized by higher values along the entire tract. Moreover, it was observed that for both sides of brain first and second fibers values are higher with 64-NDGD along the entire tract (Figures 4.24 and 4.25).

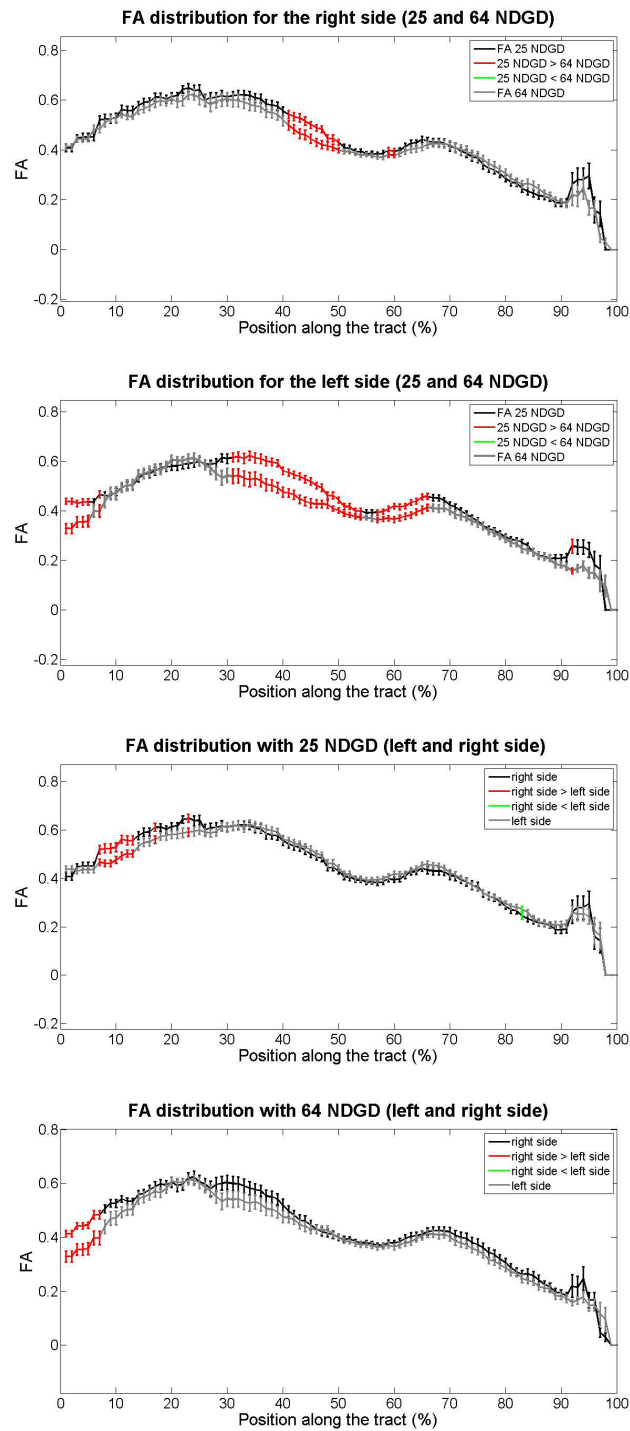


Figure 4.10: Paired t-test of FA. From the top, the first and the second panel illustrate FA distributions and differences between two NDGD (respectively 25- and 64-) at fixed side (right and left). The third and fourth panel show differences between sides of brain (right and left) at fixed NDGD (25- and 64-).

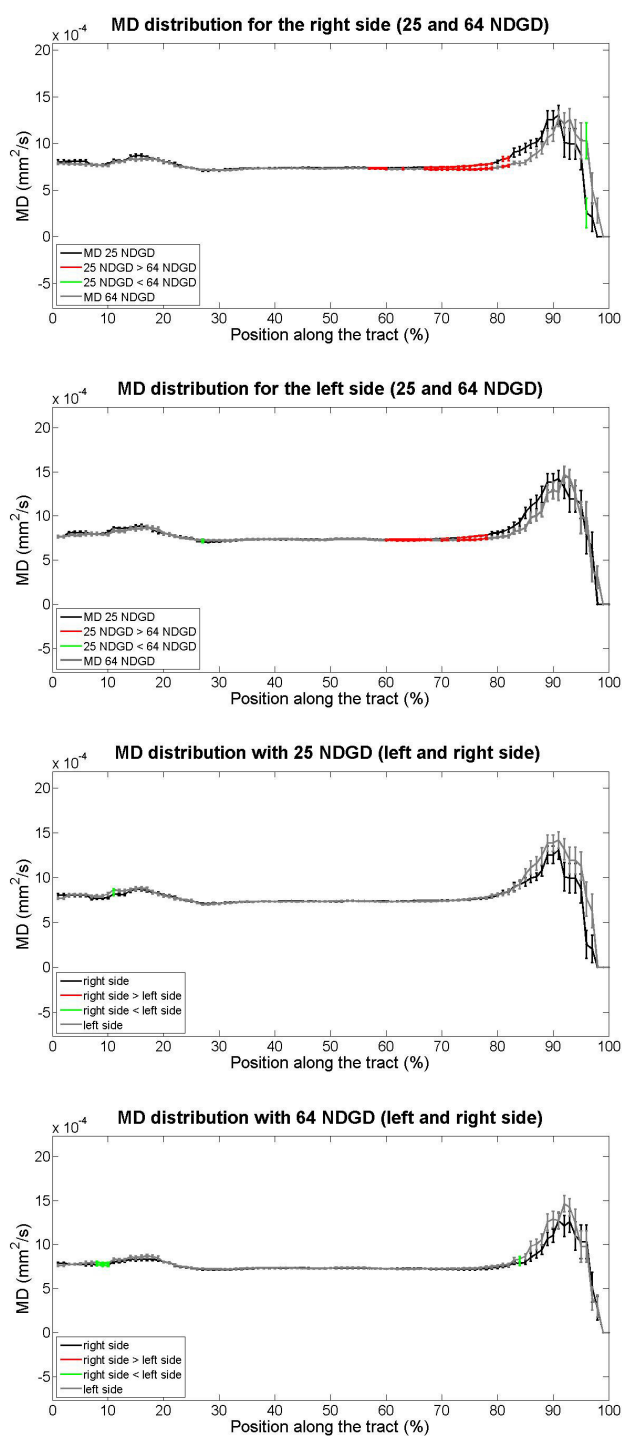


Figure 4.11: Paired t-test of MD values. From the top, the first and the second panel illustrate FA distributions and differences between two NDGD (respectively 25- and 64-) at fixed side (right and left). The third and fourth panel show differences between sides of brain (right and left) at fixed NDGD (25- and 64-).

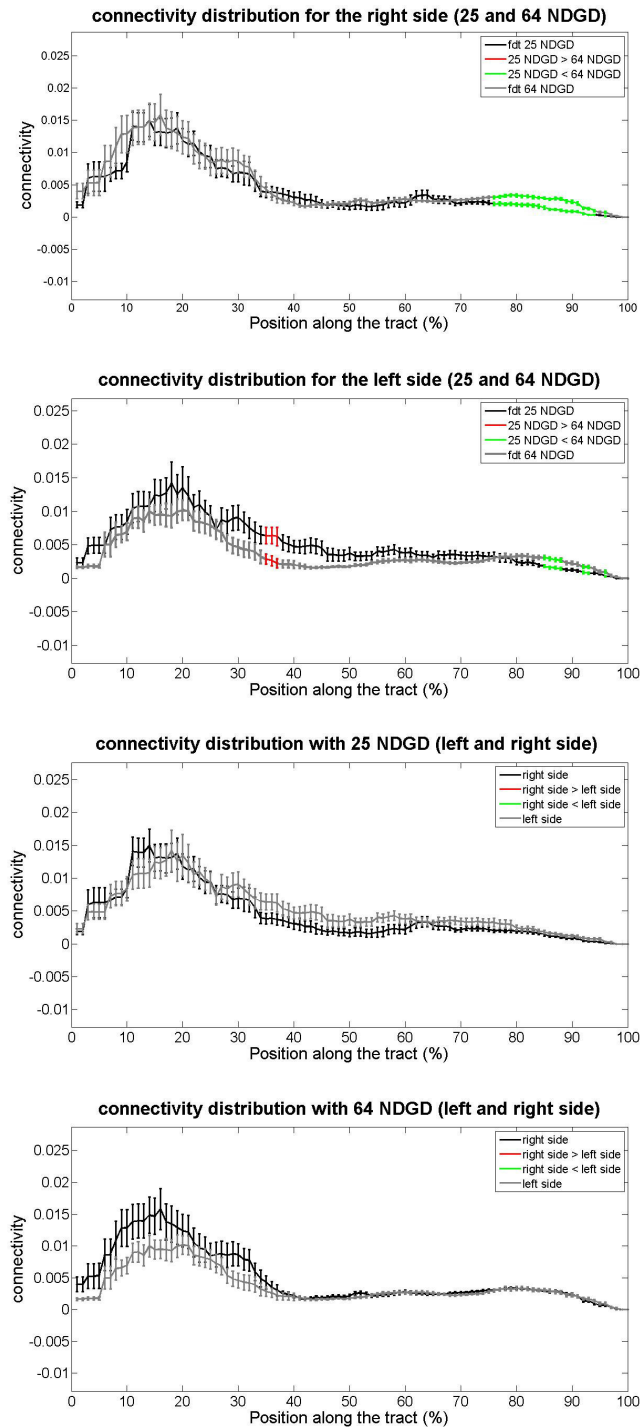


Figure 4.12: Paired t-test of connectivity (*fdt\_paths* images) distribution values. From the top, the first and the second panel illustrate FA distributions and differences between two NDGD (respectively 25- and 64-) at fixed side (right and left). The third and fourth panel show differences between sides of brain (right and left) at fixed NDGD (25- and 64-).

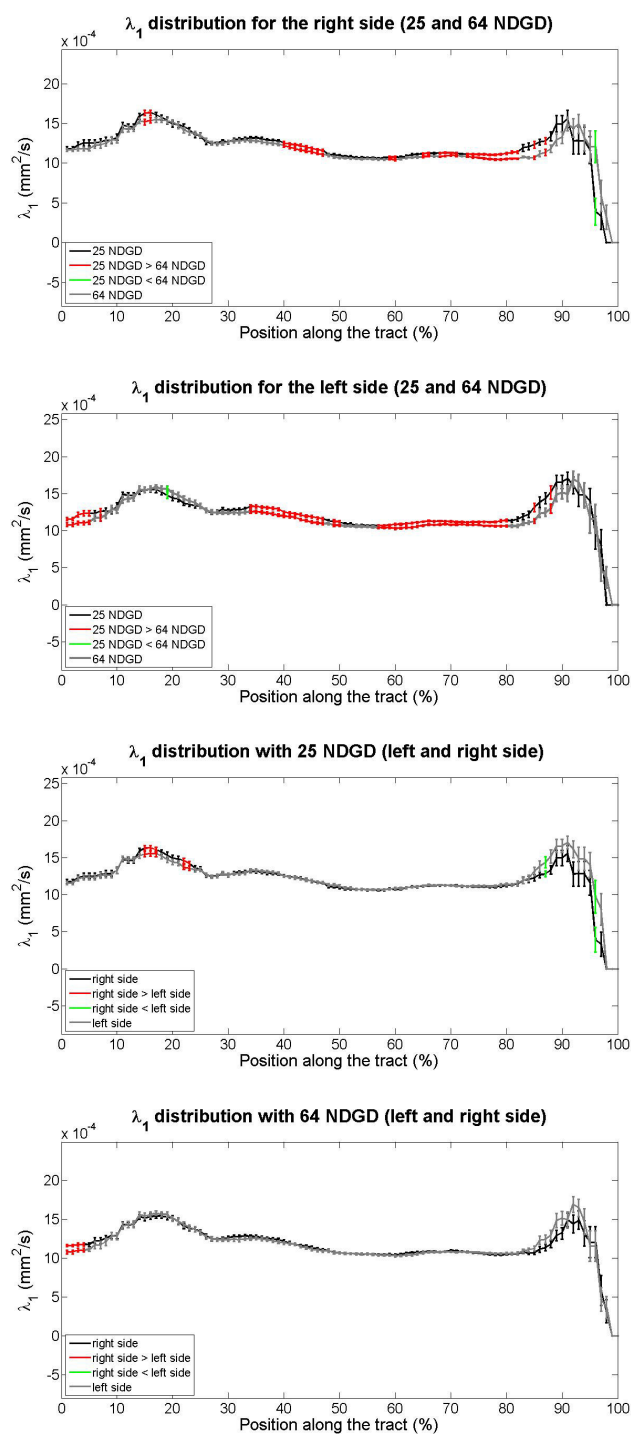


Figure 4.13: Paired t-test of  $\lambda_1$  values. From the top, the first and the second panel illustrate FA distributions and differences between two NDGD (respectively 25- and 64-) at fixed side (right and left). The third and fourth panel show differences between sides of brain (right and left) at fixed NDGD (25- and 64-).

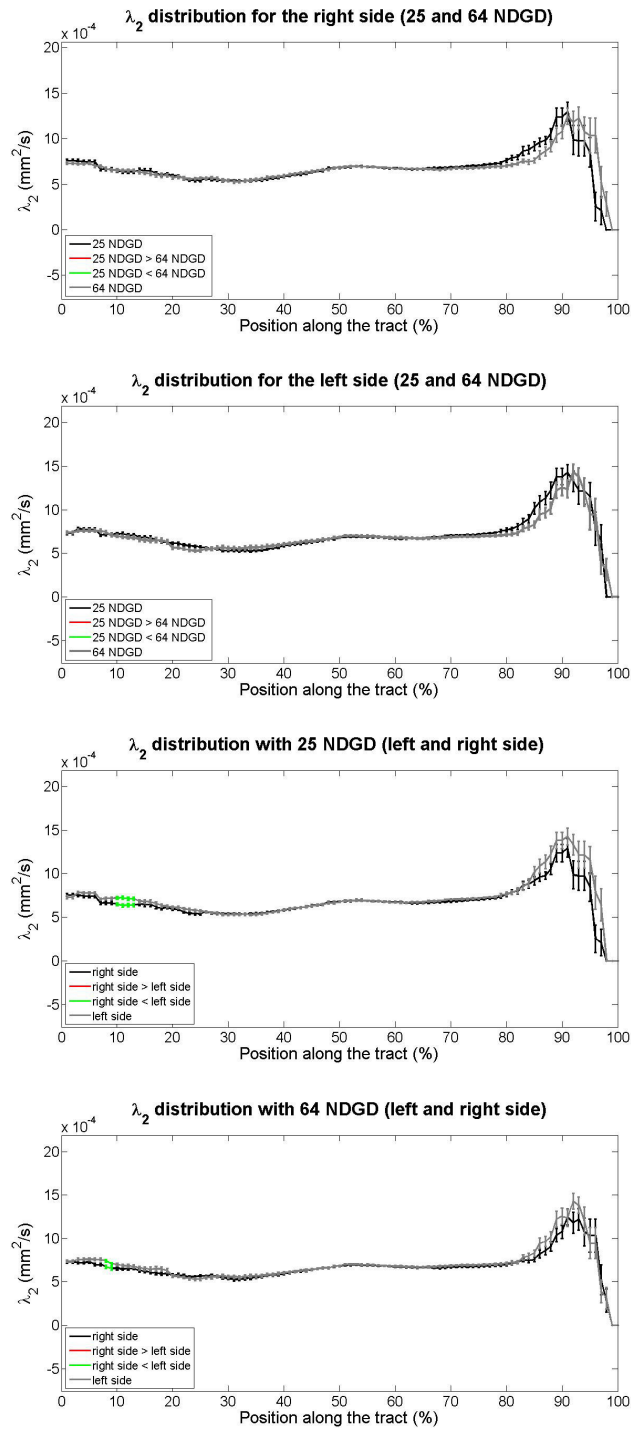


Figure 4.14: Paired t-test of  $\lambda_2$  values. From the top, the first and the second panel illustrate FA distributions and differences between two NDGD (respectively 25- and 64-) at fixed side (right and left). The third and fourth panel show differences between sides of brain (right and left) at fixed NDGD (25- and 64-).

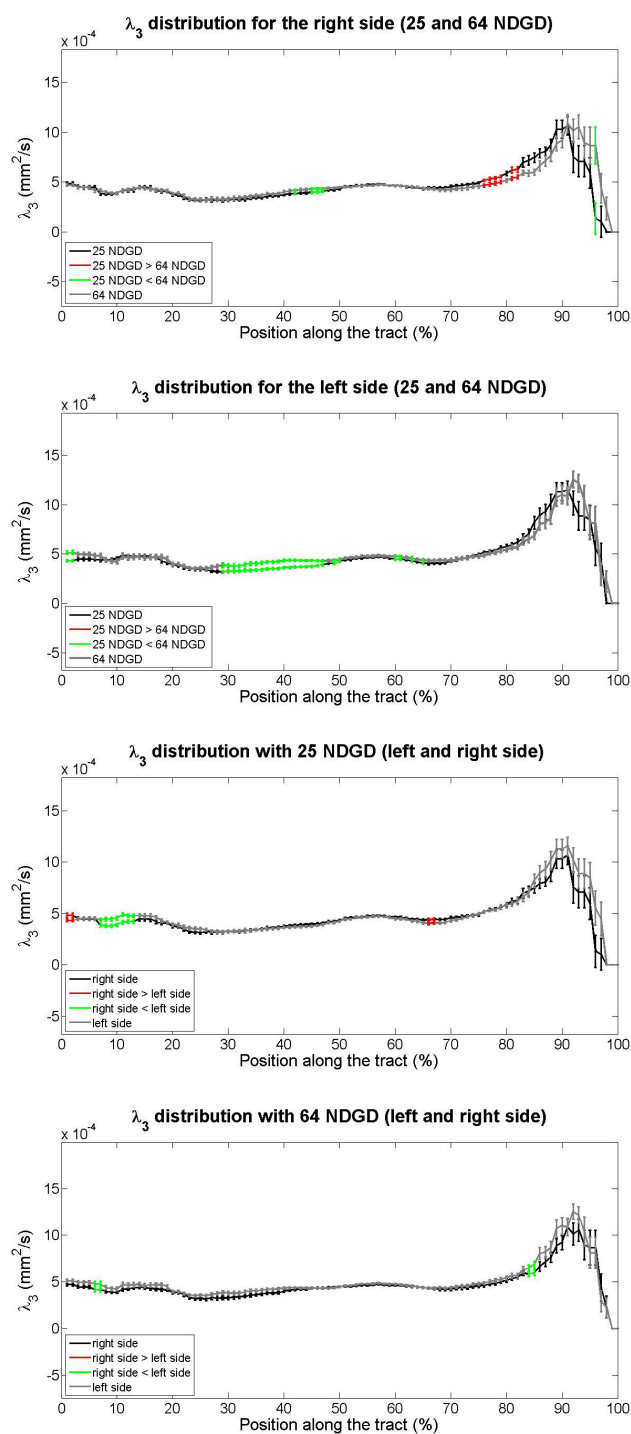


Figure 4.15: Paired t-test of  $\lambda_3$  values. From the top, the first and the second panel illustrate FA distributions and differences between two NDGD (respectively 25- and 64-) at fixed side (right and left). The third and fourth panel show differences between sides of brain (right and left) at fixed NDGD (25- and 64-).

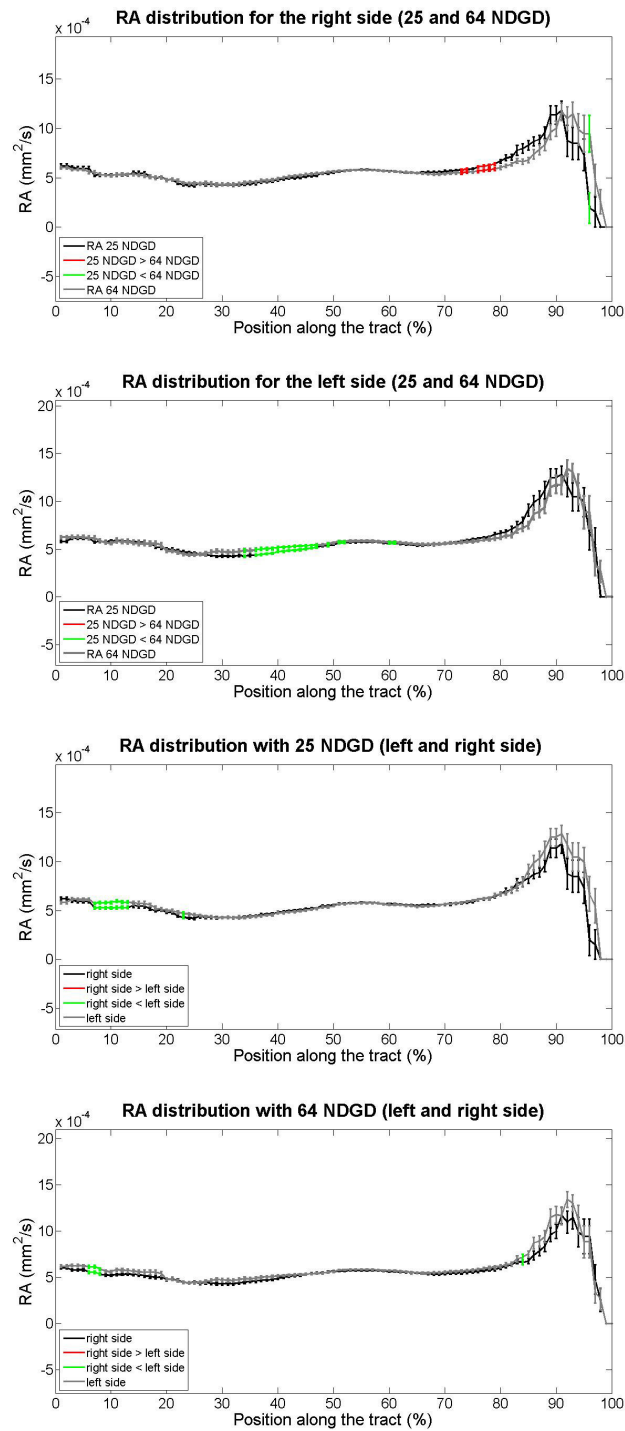


Figure 4.16: Paired t-test of RA values. From the top, the first and the second panel illustrate FA distributions and differences between two NDGD (respectively 25- and 64-) at fixed side (right and left). The third and fourth panel show differences between sides of brain (right and left) at fixed NDGD (25- and 64-).

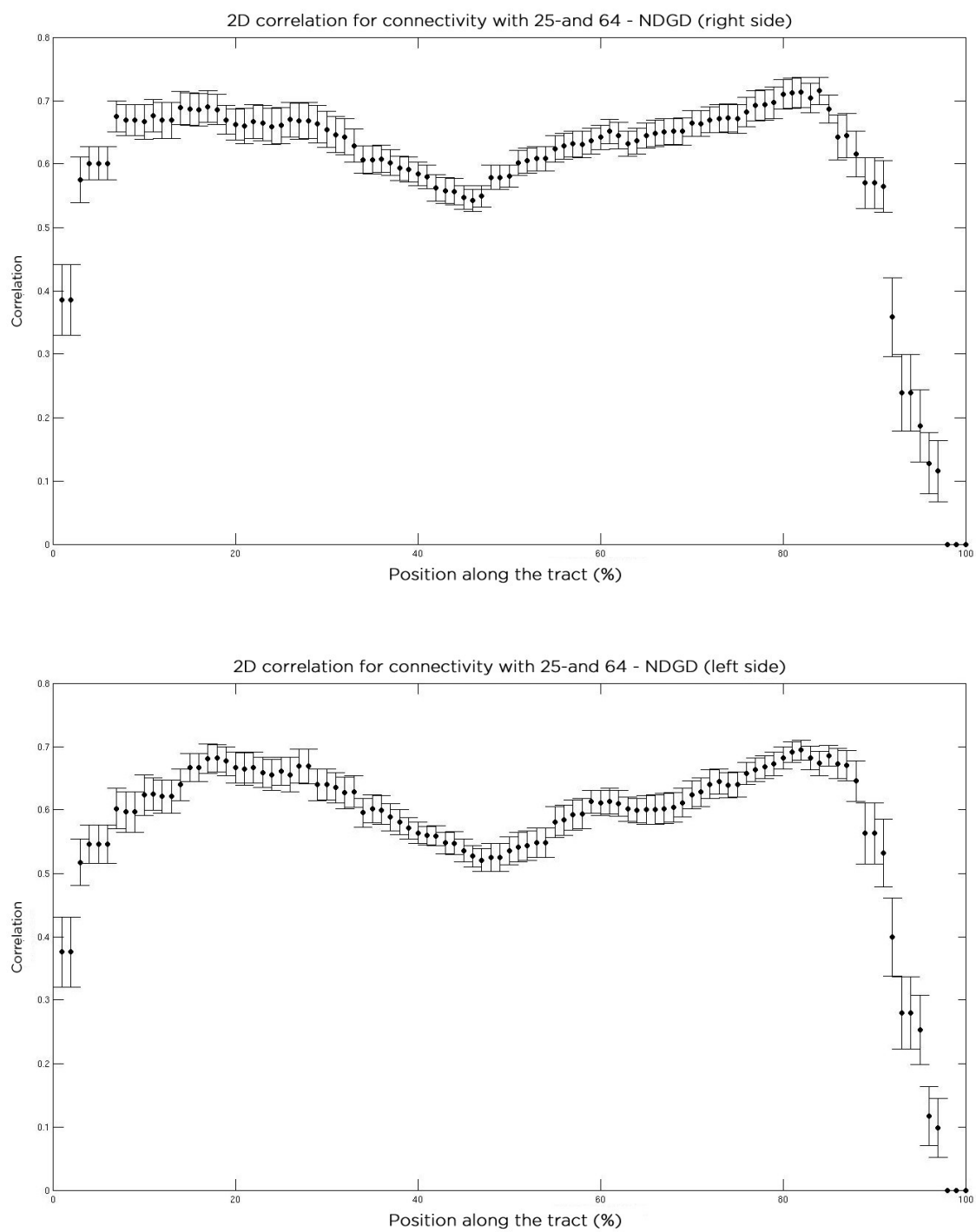


Figure 4.17: Distribution along the tract of the Pearson correlation coefficient for right side (superior panel) and left side.

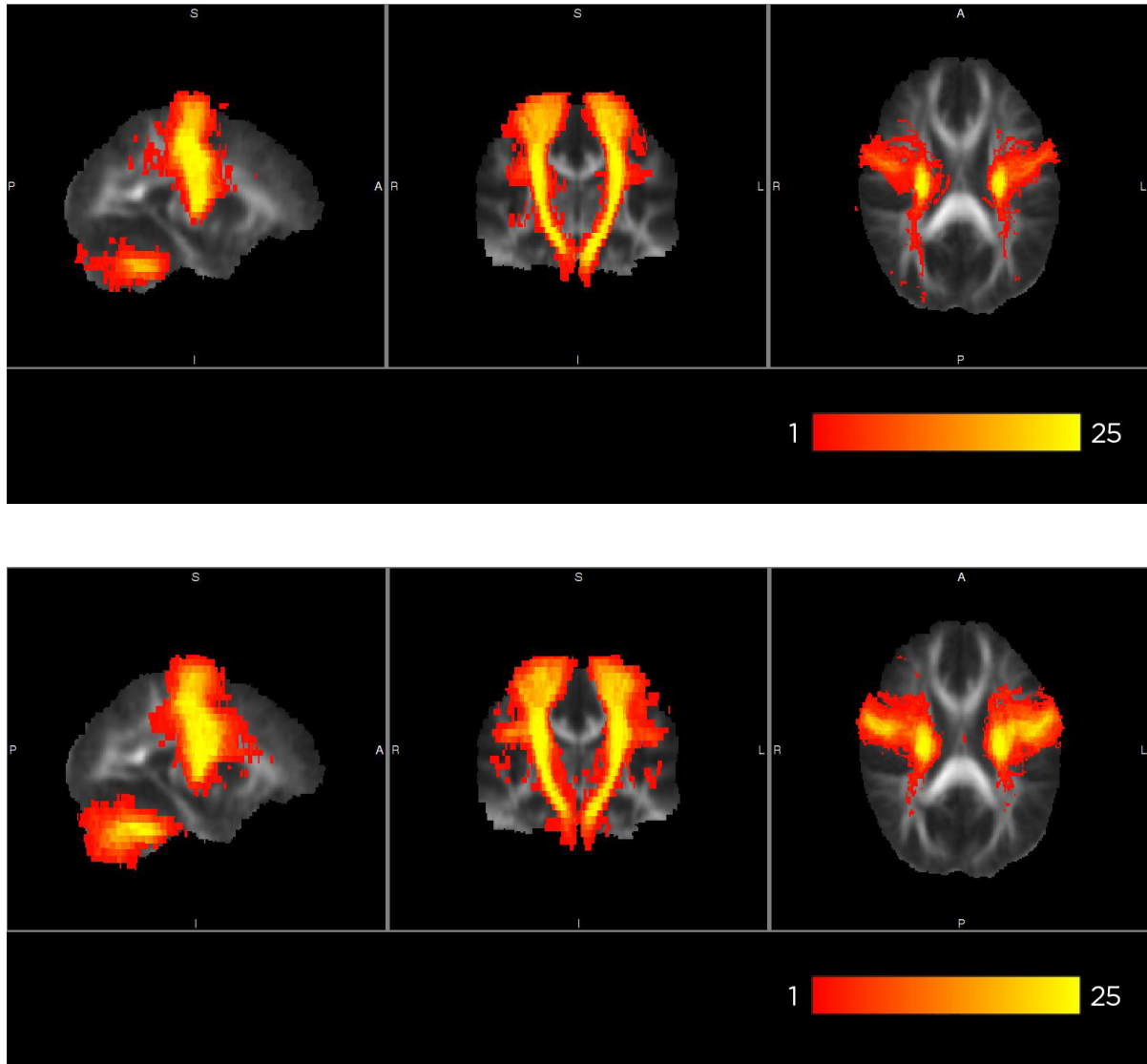


Figure 4.18: Sum of binarised tracts of all subjects at 25-NDGD (on the top) and 64-NDGD (on the bottom).

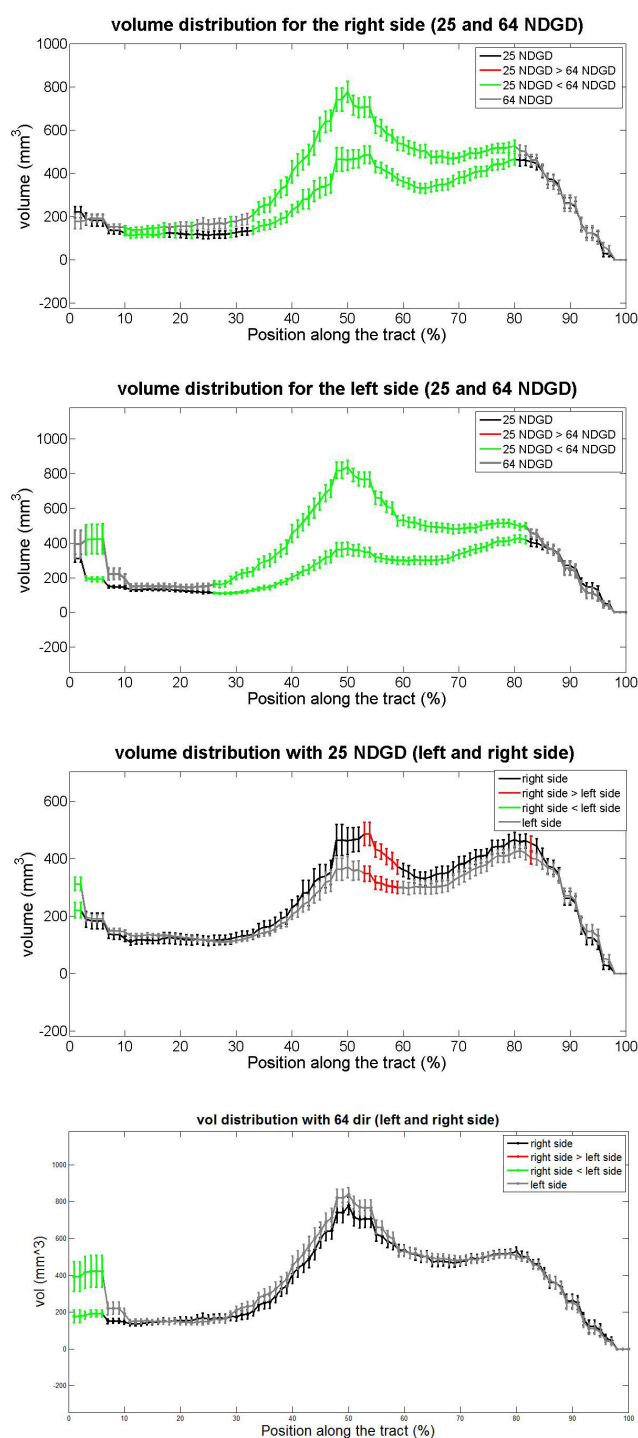


Figure 4.19: Paired t-test on total volume values. From the top, the first and the second panel illustrate volume distributions and differences between two NDGD (respectively 25- and 64-) at fixed side (right and left). The third and fourth panel show differences between sides of brain (right and left) at fixed NDGD (25- and 64-).

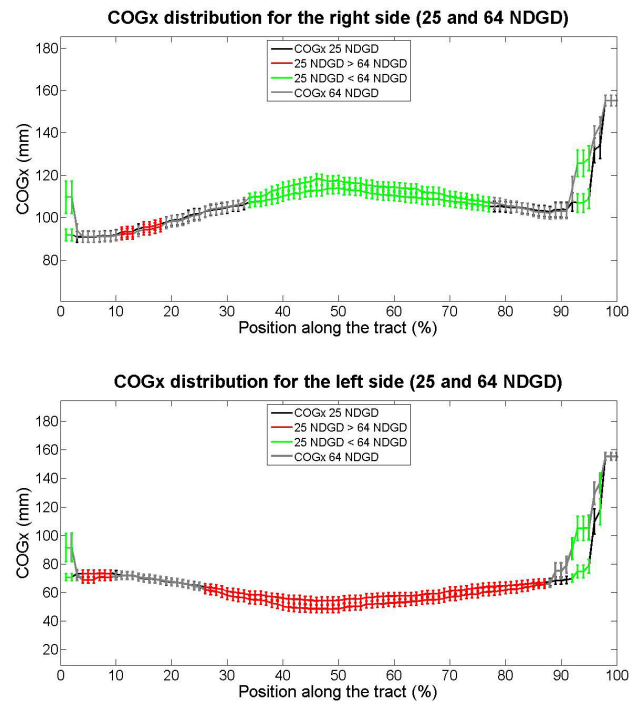


Figure 4.20: Paired t-test on COGx values. The first and the second panel illustrate COGx distributions and differences between two NDGD (respectively 25- and 64-) at fixed side (right and left).

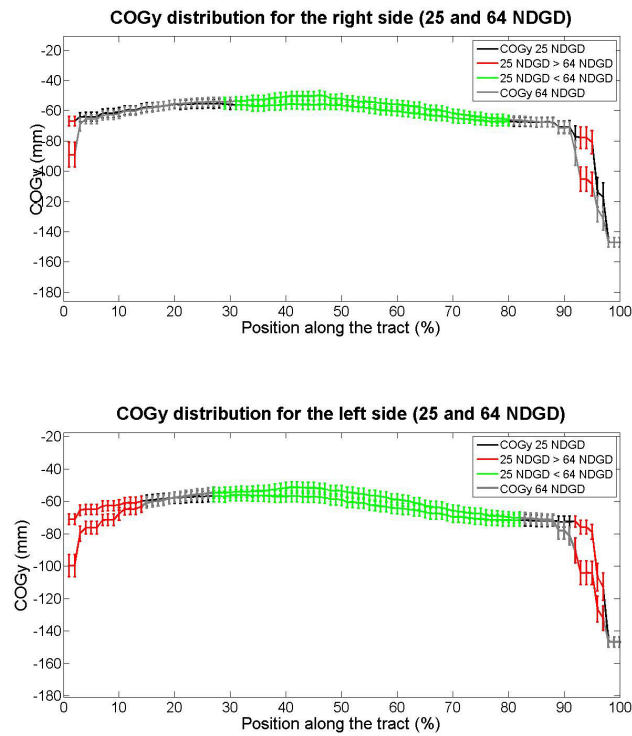


Figure 4.21: Paired t-test on COGy values. The first and the second panel illustrate COGy distributions and differences between two NDGD (respectively 25- and 64-) at fixed side (right and left).

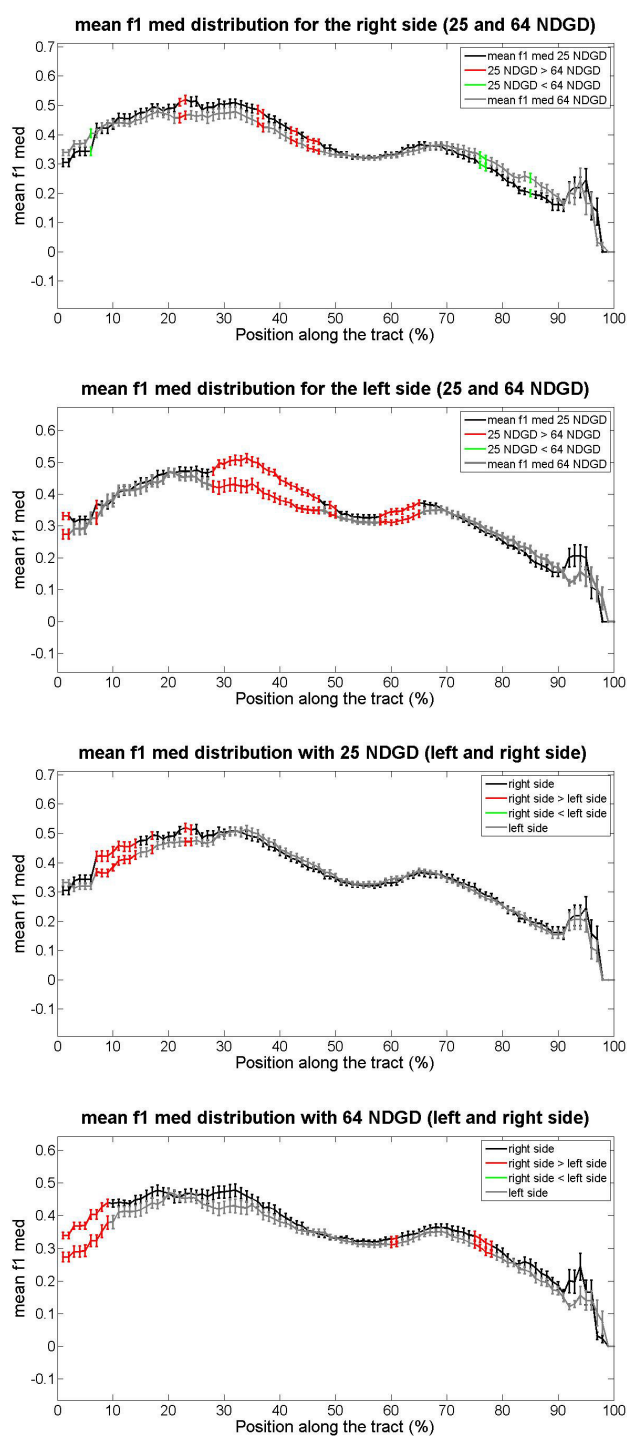


Figure 4.22: Paired t-test of mean\_f1 values. From the top, the first and the second panel illustrate FA distributions and differences between two NDGD (respectively 25- and 64-) at fixed side (right and left). The third and fourth panel show differences between sides of brain (right and left) at fixed NDGD (25- and 64-).

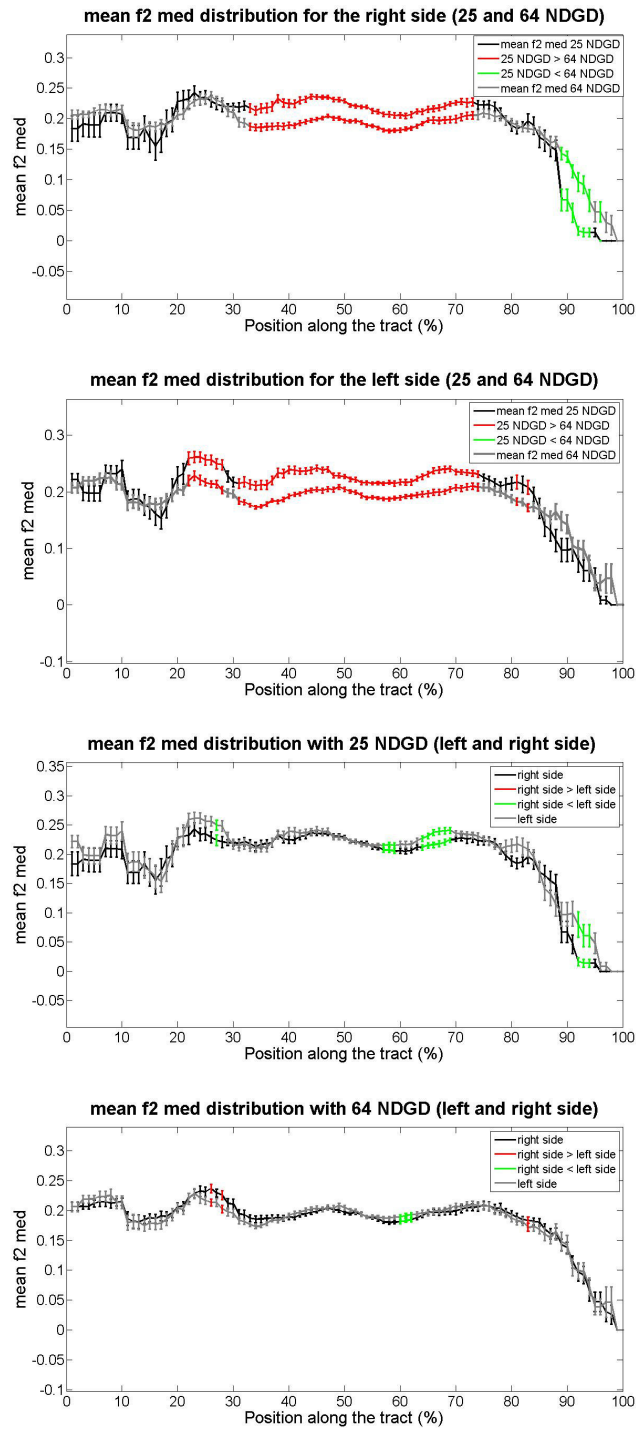


Figure 4.23: Paired t-test of mean  $f_2$  values. From the top, the first and the second panel illustrate FA distributions and differences between two NDGD (respectively 25- and 64-) at fixed side (right and left). The third and fourth panel show differences between sides of brain (right and left) at fixed NDGD (25- and 64-).

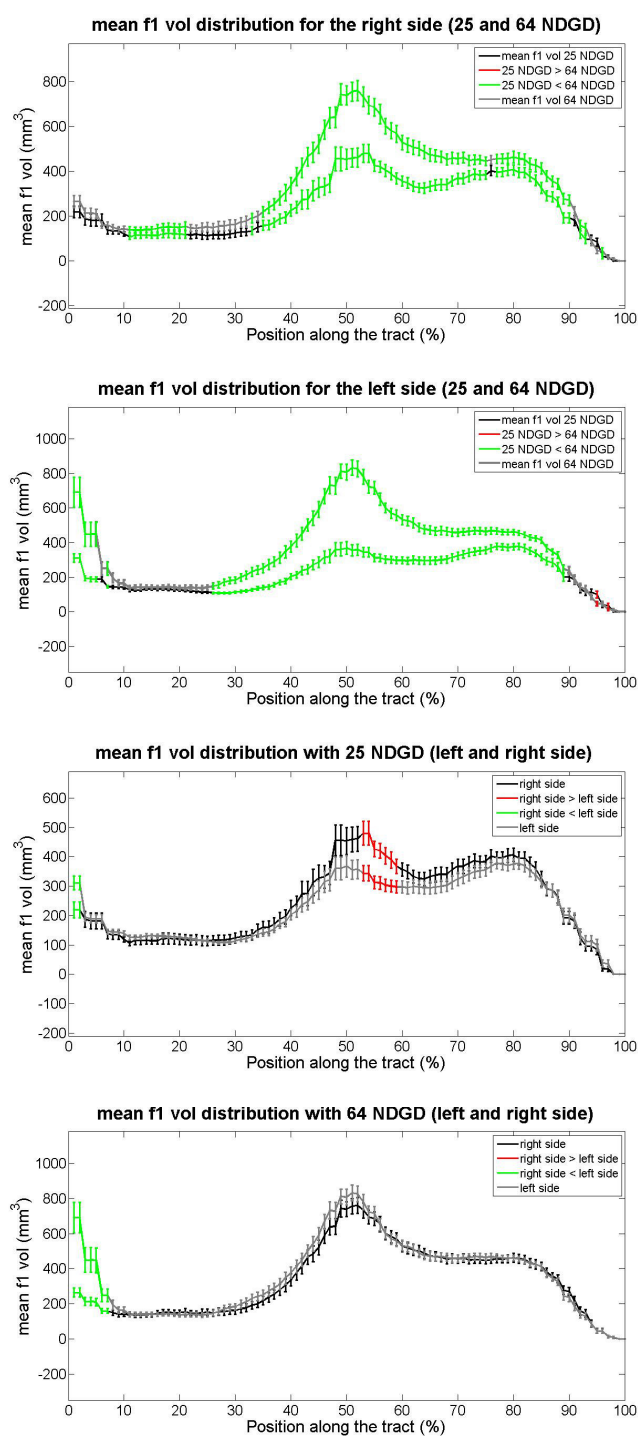


Figure 4.24: Paired t-test on mean.f1 volumes. From the top, the first and the second panel illustrate mean.f1 volumes distributions and differences between two NDGD (respectively 25- and 64-) at fixed side (right and left). The third and fourth panel show differences between sides of brain (right and left) at fixed NDGD (25- and 64-).

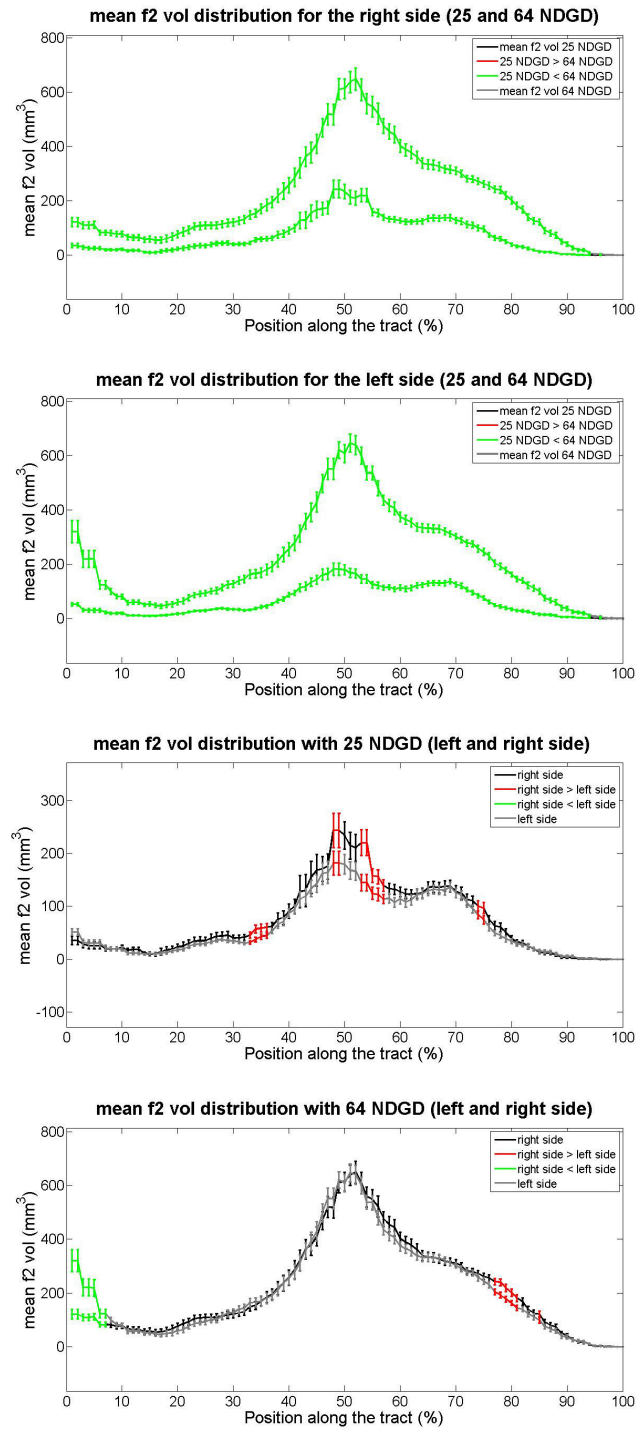


Figure 4.25: Paired t-test on mean\_f2 volume. From the top, the first and the second panel illustrate mean\_f2 volume distributions and differences between two NDGD (respectively 25- and 64-) at fixed side (right and left). The third and fourth panel show differences between sides of brain (right and left) at fixed NDGD (25- and 64-).

# Chapter 5

## Discussion

In the present study we investigated the distributions of various MR imaging parameters within the CSTs reconstructed from DWI data with probabilistic tractography, with 25 and 64 directions of diffusion gradient, obtained from healthy subjects. Tracts are delineated applying a probabilistic tractography algorithm [31], which tracked the CST from the primary motor cortex in the precentral gyrus to the pons. Other recent studies have already drawn the CST using similar ROIs ([47], [48] and [50]), but the novelty of our work is the development of a method that employed a subject-specific automatic segmentation mask and ROIs drawn on a FA template to performed an along-tract analysis on tracts delineated using probabilistic tractography. The automatic procedure for drawing of the ROIs assures an almost total independence from user's subjectivity approach and it is also useful for studies with an higher number of subjects than our and for studies on patients. Visual evaluation of the reconstructed tracts showed that the obtained CSTs passed through the anatomical landmark points and this confirmed the reliability of the method.

Previous studies investigated tract reconstruction variability using quantitative analyses along the tract with different approaches for parameterization [61] [60] [59]. In order to improve regional specificity of the spatial evaluation of the diffusion properties, we performed a division of each obtained CST in a 100 segments, whose size was the same in every subject. The results of the analysis on FA values, obtained for each percentile in each subject, confirmed the strong benefit to perform an along-tract analysis, as underlined by the study of Colby et al. [58]: FA plot showed a consistent variability through the entire tract and across different subjects (see Figures 4.4 and 4.5 in Section 4.2). This

highlights the evidence that conducting a tract-average study could hide local changes of the parameter. In addition, supporting the last remark, it was found that the intra-subject variability was significantly higher than inter-subject one for both FA and MD values.

It can be observed, from the 90th to 100th percentile, a sudden increase in the plot of FA that is due to fitting errors on the maps, which is frequent at the edge of the brain (see Figure 3.11 in Section 3.5.2). Also MD measurement cannot be ascribed to the brain parenchyma beyond the 90th percentile (see Figures 4.6 and 4.7 in Section 4.2). The presence of rising indicates percentiles in which liquor is detected, since the meninx are present, while the consecutive decrease is due to the evidence that, in the last three or four percentiles we usually did not have brain data.

Connectivity distribution showed a great variability in the same way along the tract as well as across subjects (see Figure 4.8 and 4.9 in Section 4.2): in this case, an along-tract analysis would not probably give any additional useful information respect to an average tract analysis. Effectively, no significant differences between intra- and inter-variability were found. It was interesting to note an increase of connectivity values in correspondence to the location of the posterior limb of the internal capsule; we suppose that maybe this can be explained considering that samples, after leaving the wide area of the motor cortex, pass in the small area of internal capsule: they are all condensed in few voxels and this leads the connectivity values to increase. The statistical analysis on connectivity have been performed on the normalized and thresholded *fdt\_paths* images. The effect of this procedure has been evaluated considering the results of RMANOVA: while connectivity values did not seem to be affected by choice of side or NDGD, non-normalized connectivity and waypoint values showed significant differences depending on the two NDGDs. Thus, it is evident that dividing connectivity values by the waytotal number is essential to conduct a good comparison between data obtained at different NDGDs.

In order to investigate specific regional differences along the tract, we compared each respective percentile between subjects, for different sides and at different NDGDs. In particular, FA showed a significant increase comparing the right with the left side of CST, in an area between the pons and the cerebral peduncle at 25-NDGD, from the 7th to 18th percentile, and at the level of the pons at 64-NDGD, from the 1st to the 7th percentile (see Figure 4.10 in Section 4.2.3). This observation may be linked to the asymmetry of the corticospinal tract. Few studies, for example that of Nathan et al. [38],

suggest that a greater number of corticospinal fibers crosses to the right side at the level of decussation: thus the right side of CST is larger than the left and the measurement of the parameter can be affected by this evidence. Observing the plot of the volume of the second fiber at 64-NDGD (see Figure 4.25 in Section 4.2.5), it can be noted that, exactly at the level of pons, the distribution for the two different sides of the brain showed very different values: it can be observed a behaviour similar to a fork. These two similar behaviours could be linked and the evidence that at 64-NDGD a second fiber is detected in the left side could justify the FA plot. In addition, in our procedure, we observed that the delineated tract wrongly ended into the cerebellum, and this is more evident at 64-NDGD than 25-NDGD; for this reason we decided to cut the tract at the level of the pons, excluding parts below it. Thus, we hypothesized that just before pons, the algorithm started to consider fibers that belong to cortico-ponto-cerebellar tract.

MD and connectivity distributions did not show any differences between right and left sides at each NDGD.

One of the most interesting result comes from the comparison of the FA values between 25- and 64-NDGD. For the right side, values at 25-NDGD showed an increase at the level of the posterior limb of the internal capsule, while for the left side FA values at 25-NDGD resulted higher along the entire central portion of the CST. In order to understand the origin of this behaviour, we considered the volume of the first and second detected fibers. In this way, we tested the hypothesis that FA differences could be due to the presence of the second fiber. This is a great advantage of using a probabilistic algorithm instead of the deterministic tractography. For example, Lin et al. [59] conducted a very similar study: they investigated the presence of abnormal diffusion along the pyramidal tract (PYT) of relapsing neuromyelitis optica (RNMO) patients with a length-normalized parameterization method in order to realized specific comparisons across the subjects. They divided equally the normalized length into a certain number of segments and obtained diffusion indices (including FA and RA) from each segment. However, they admitted that it was not possible to trace the whole tract due to the limitations of the streamline tractography for crossing fibers. In the present study we tried to overcome this problem. It can be noted that for both sides along almost the tract for the first fiber, and along the entire CST for the second fiber, the volume distributions at 64-NDGD were higher respect to distribution at 25-NDGD. In particular, they resulted strongly different at the level of pons and in correspondence of the 50th percentile, where the first distribution was tripled respect to that at 25-NDGD. Differences in volume depend on the fact that

algorithm at 64-NDGD is more able to detect more than one dominant direction of the fibers respect to at 25-NDGD. Observing the results of paired t-test on the first fiber at different NDGD we can note correspondence, with respect to FA, between percentiles affected by significative differences, in particular on the left side. The distribution of the median of the second fiber showed a larger area interested by significant differences, along the central part of the CST, with an increase for values at 25-NDGD (see Figure 4.23 in Section 4.2.5). This can be explained considering the work of Bastin et al [64], which found that the measured anisotropy of an inhomogeneous medium becomes progressively greater as the signal-to-noise ratio (SNR) decreases.

A comparison between different NDGDs for MD values showed significative differences in cortical sulci area, revealing an increase for values at 25-NDGD in the same way for both sides of brain. This can be due to the fact that in this area the algorithm was not able to correctly discern white and grey matter. This result is in agreement with Jones [63] who found that a robust estimation of mean diffusivity requires at least 30 sampling orientations. The measure of eigenvalues in each percentile validated results obtained for MD. In more detail, it was observed an increase for values at 25-NDGD in  $\lambda_1$  distribution, approximately from 40th to 50th percentile and from 70th to 85th percentile in the right side while for left side we registered an increase at the same NDGD at the level of the pons and in the most part of the central area of CST, from 35th to 50th and from 60th to 80th percentile;  $\lambda_2$  distribution did not show any significative difference between different NDGDs; for the left side of  $\lambda_3$  distribution it was observed an increase for values at 64-NDGD from 30th to 50th percentile (see Figures 4.13, 4.14 and 4.15 in Section 4.2.3). We deduced that in the first interested part of the CST the opposite tendency of  $\lambda_1$  and  $\lambda_3$  produced a balance of the differences and the MD significative results are due only to the differences in the last part of  $\lambda_1$  distribution. Plot of  $\lambda_1$ ,  $\lambda_2$  and  $\lambda_3$  did not show any differences between different sides and this was in accord with the analogous MD distribution.

The similarity of RA distribution respect to  $\lambda_3$  plot was evident: indeed RA depends on both  $\lambda_2$  (no differences, as specified above) and  $\lambda_3$ .

To understand deeply the different results at 25-NDGD respect to 64-NDGD and to observe where the different tracts diverge, we investigate the spatial correlation of the respective obtained tracts (see Figure 4.17 in Section 4.2.4). A visual evaluation of the total volume distribution showed, for both NDGDs, a good correspondence of the tracts: the great quantity of yellow areas (tract of 25 subjects) in the right anatomical reference

points was a validation of the reliability of the used procedure. Performing a 2D spatial comparison between tracts obtained with different NDGDs, we observed a Pearson correlation coefficient in a range between 0.5 and 0.7 on average, with a decrease in correspondence of the 50th percentile and in the last percentiles (over the 90th percentile). Observing the total volume distribution, that showed higher value at 64-NDGD along the most part of CST, we noted that in correspondence of the 50th percentile plot of values at 25- and 64-NDGD showed a great difference (the maximum at 64-NDGD is almost four times respect to 25-NDGD). The Pearson analyses supported the hypothesis of good reliability for algorithm with 25-NDGD for acquisitions and volume distribution confirmed the evidence of a greater number of detected fibers at 64-NDGD. In particular, this is evident in the lateral portion of the cortico-spinal tract that is a big pathway not completely described with the first fiber. This is in line with the study of Behrens et al. [31] that found that a multi-fiber probabilistic algorithm is able to describe in a better way this area of the CST, characterized by more than a single fiber.

Further spatial analyses were performed: the COG for x and y showed that the tracts delineated at 64-NDGD were more mesial (significant differences in COGx distribution) and more anterior (significant differences for COGy) respect to those at 25-NDGD.



# Conclusions and future directions

In conclusion, in this study we developed a procedure to reconstruct the corticospinal tract with a probabilistic tractography algorithm using an automatic segmentation of the motor cortex and a common space for all subjects to draw masks onto the FA map. In this way the reproducibility of the process is assured. We calculated diffusion parameters values for the corticospinal tract from data obtained at 25 and 64 directions of the diffusion gradient.

A central aim of this study was the validation of a parameterization procedure along the tract, in order to obtain specific local diffusion parameters and to establish correspondence of white matter fiber segments across different subjects. In each subject, the drawn tract was divided in 100 equal segments (percentiles). Statistical analyses showed that intrasubject variability of FA and MD values was significantly higher than intersubject variability: this confirmed the importance to perform a quantitative study in order to obtain localized information on behaviour of parameters, with respect to the most common studies which evaluate mean diffusion parameters values of the tract. In particular, the effects of different sides of the brain and different numbers of diffusion gradient direction on metrics of interest were investigated in each percentile of the delineated tract. One of the most relevant result is the significant difference between FA values at 25 with respect to 64 NDGD in the central part of the CST, above the posterior limb of the internal capsule. The capability of the probabilistic algorithm to detect multiple-dominant fibers direction permitted to understand the plot of FA. A further analysis on spatial correlation between tracts obtained with the two NDGDs provided awareness about the reliability of the tractography at 25-NDGD, observing a good 2D correlation coefficient. This is an important finding as acquisitions at lower NDGD are more feasible and comfortable in a clinical setting. However, the analysis highlighted the great advantage of using a 64-NDGD acquisition, since it allowed to describe in a more detailed way the CST, in particular the lateral portion of the tract, because it detected

fibers that at 25-NDGD were hidden.

We suppose that the difference of diffusion parameters values corresponding to the right and left CST, can be explained considering the anatomical asymmetries of CST.

Development and future applications can be suggested by the results obtained. First of all, it could be interesting to investigate the relation between asymmetries of the CST with handedness of subjects: it is a pivotal point in modern literature and the results could help also to deeply explain behaviour of some parameters in this study. The next step could be an along-tract analysis of other tracts of interest, like the corpus callosum and cingulum. In fact, it could be fascinating to employ this method on groups of patients; in particular, our goal is the study of changes of diffusion parameters along selected white matter tracts in subjects with neurodegenerative diseases with motor symptoms such as parkinsonism disorders or other neurodegenerative disorders.

# Bibliography

- [1] Fick A. On liquid diffusion. *Philosophical Magazine*, 10(63):30-39, 1855.
- [2] Johansen-Berg H, Behrens T. Diffusion MRI. From a quantitative measurement to in vivo neuroanatomy. *Elsevier-Academic Press*, 2009.
- [3] Jeurissen B. Improved analysis of brain connectivity using high angular resolution diffusion MRI. PhD thesis, *University of Antwerp, Belgium*.
- [4] Mori S, Wakana S, Nagae-Poetscher L, van Zijl P. MRI Atlas of Human White Matter. *Elsevier*, 2005.
- [5] Callaghan P. Principles of nuclear magnetic resonance microscopy. *Oxford University Press*, 1994.
- [6] Hornak JP. The basics of MRI. Interactive Learning Software, 2011.
- [7] Carr HY and Purcell EM. Effects of diffusion on free precession in nuclear magnetic resonance experiments. *Physical Review*, 94(3):630, 1954.
- [8] Stejskal E and Tanner J. Spin diffusion measurements: spin echoes in the presence of a time-dependent field gradient. *The Journal of Chemical Physics*, 42(1):288, 1965.
- [9] Le Bihan D, Breton E, Lallemand D, Grenier P, Cabanis E, Laval-Jeantet M. MR Imaging of Intravoxel Incoherent Motions: application to diffusion and perfusion in Neurologic Disorders. *Radiology* 161:401-407, 1986.
- [10] Le Bihan D, Mangin JF, Poupon C, Clark C, Pappata S, Molko N, Chabriat H. Diffusion Tensor Imaging: concepts and applications. *Journal of magnetic resonance imaging* 13:534-546, 2001.

- [11] Mori S and Zhang J. Diffusion Tensor Imaging (DTI). *elsevier*, 2009.
- [12] Basser P, Pierpaoli C. Microstructural and physiological features of tissues elucidated by quantitative-diffusion-tensor MRI. *Journal of magnetic resonance Series B* 111, 209-219, 1996.
- [13] Pajevic S and Pierpaoli C. Color schemes to represent the orientation of anisotropic tissues from diffusion tensor data: application to white matter fiber tract mapping in the human brain. *Magn Reson Med* 43(6):921, 2000.
- [14] Wheeler-Kingshott C and Cercignani M. About "Axial" and "Radial" Diffusivities. *Magnetic Resonance in Medicine* 61:1255-1260, 2009.
- [15] Lebel C, Benner T, Beaulieu C. Six is enough? Comparison of diffusion parameters measured using six or more diffusion-encoding Gradient Directions With Deterministic Tractography. *Magnetic Resonance in Medicine* 68:474-483, 2012.
- [16] Giannelli M, Cosottini M, Michelassi MC, Lazzarotti G, Belmonte G, Bartolozzi C, Lazzeri M. Dependence of brain DTI maps of fractional anisotropy and mean diffusivity on the number of diffusion weighting directions. *Journal of applied clinical medical physics*, Vol.1 11, No. 1, 2010.
- [17] Papadakis N, Murrillsa C, Halla L, Huangb C, Carpenterc T. Minimal gradient encoding for robust estimation of diffusion anisotropy *Magnetic Resonance Imaging* 18 671-679, 2000.
- [18] Papadakis N, Xing D, Huang C, Hall L, Carpenter TA. A comparative study of acquisition schemes for diffusion tensor imaging using MRI *Journal of Magnetic Resonance* 137, 67-82, 1999.
- [19] Jezzard P, Matthews PM and Smiths SM. *Functional MRI: an introduction to methods*. Oxford University Press, 2001.
- [20] Mori s and van Zijil P. Fiber tracking: principles and strategies-atechnical review. *NMR Biomed.*, 15:468-480, 2002.
- [21] Sporns O. The human connectome: a complex network. *Ann NY Acad Sci* 1224:109-125, 2011.

- [22] [www.humanconnectome.org](http://www.humanconnectome.org)
- [23] Ciccarelli O, Catani M, Johansen-Berg H, Clark C, Thompson A. Diffusion-based tractography in neurological disorders: concepts, applications, and future developments. *Lancet Neurol* 7:715-27, 2008.
- [24] Mori S, Crain B, Chacko VP, van Zijl P. Three-dimensional tracking of axonal projections in the brain by magnetic resonance imaging. *Ann Neurol* 45:265-269, 1999.
- [25] Catani M, Howard R, Pajevic S, Jones D. Virtual in vivo interactive dissection of white matter fasciculi in the human brain. *NeuroImage* 17, 77-94, 2002.
- [26] Lazar M., Mapping brain anatomical connectivity using white matter tractography. *NMR Biomed.* 23:821-835, 2010.
- [27] Parker G and Alexander D., Probabilistic Monte Carlo based mapping of cerebral connections utilising whole-brain crossing fibre information. In Proceedings of the International Conference on Information Processing in Medical Imaging, pages 684-695, Lake District, United Kingdom, 2003.
- [28] Jones D. Determining and visualizing uncertainty in estimates of fiber orientation from diffusion tensor MRI *Magnetic Resonance in Medicine* 49:7-12, 2003.
- [29] Jones D. Tractography gone wild: probabilistic fibre tracking using the wild bootstrap with diffusion tensor MRI. *IEEE Trans Med Imaging* 27(9):1268-74, 2008.
- [30] Behrens T, Woolrich MW, Jenkinson M, Johansen-Berg H, Nunes RG, Clare S, Matthews PM, Brady JM, Smith SM. Characterization and propagation of uncertainty in Diffusion-Weighted MR imaging *Magnetic Resonance in Medicine* 50:1077-1088, 2003.
- [31] Behrens T, Johansen Berg H, Jbabdi S, Rushworth M, Woolrich M. Probabilistic diffusion tractography with multiple fibre orientations: What can we gain? *NeuroImage* 34 144-155, 2007.
- [32] Jbabdi S, Johansen-Berg H. Tractography: where do we go from here? *Brain Connectivity* Vol.1, No. 3, 2011.

- [33] Hagmann P, Cammoun L, Gigandet X, Meuli R, Honey CJ, Wedeen VJ, Sporns O. Mapping the structural core of human cerebral cortex. *PLoS Biol.* 6: e159, 2008.
- [34] Langkammer C, Krebs N, Goessler W, Scheurer E, Ebner F, Yen K, Fazekas F, Ropele S. Quantitative MR Imaging of Brain Iron: A Postmortem Validation Study *Radiology* 257, 455-462, 2010.
- [35] Al Masri O. An Essay on the human corticospinal tract: history, development, anatomy, and connections. *Neuroanatomy* 10: 1-4, 2011.
- [36] Hong JH, Son SM, Jang SH. Somatotopic location of corticospinal tract at pons in human brain: a diffusion tensor tractography study. *Neuroimage* 51: 952-955, 2010.
- [37] Lemon RN. Descending pathways in motor control. *Annu. Rev. Neurosci.* 31: 195-218, 2008.
- [38] Nathan PW, Smith MC, Deacon P. The corticospinal tracts in man. Course and location of fibres at different segmental levels. *Brain* 113: 303-324, 1990.
- [39] Herve PY, Leonard G, Perron M, Pike B, Pitiot A, Richer L, Veillette S, Pausova Z, Paus T. Handedness, motor skills and maturation of the corticospinal tract in the adolescent brain. *Hum. Brain Mapp.* 30: 3151-3162, 2009.
- [40] Westerhausen R, Huster RJ, Kreuder F, Wittling W, Schweiger E. Corticospinal tract asymmetries at the level of the internal capsule: is there an association with handedness? *Neuroimage* 37: 379-386, 2007
- [41] Garey LJ. Brodmann's Localisation in the Cerebral Cortex. *Springer*, 2006.
- [?] Crichton P, Crichton PJ. Penfield's homunculus. *J Neurol Neurosurg Psychiatry*, 57(4):525, 1994.
- [42] Jenkinson M, Beckmann CF, Behrens TE, Woolrich MW, Smith SM. FSL. *Neuroimage* 62(2):782-90, 2012.
- [43] Woolrich MW, Jbabdi S, Patenaude B, Chappell M, Makni S, Behrens T, Beckmann C, Jenkinson M, Smith SM. Bayesian analysis of neuroimaging data in FSL. *NeuroImage* 45:S173-86, 2009.

- [44] Jenkinson M, Smith S. A global optimisation method for robust affine registration of brain images. *Medical Image Analysis 5 (2001)* 143-156, 2001.
- [45] Behrens TE, Johansen-Berg H, Woolrich MW, Smith SM, Wheeler- Kingshott CA, Boulby PA, et al. Non-invasive mapping of connections between human thalamus and cortex using diffusion imaging. *Nat Neurosci 2003a*; 6: 750-7, 2003.
- [46] Behrens TE, Woolrich MW, Jenkinson M, Johansen-Berg H, Nunes RG, Clare S, et al. Characterization and propagation of uncertainty in diffusionweighted MR imaging. *Magn Reson Med 2003b*; 50: 1077-88, 2003.
- [47] Ciccarelli O, Behrens TE, Altmann DR, Orrell RW, Howard RS, Johansen-Berg H, Miller DH, Matthews5 PM and Thompson AJ. Probabilistic diffusion tractography: a potential tool to assess the rate of disease progression in amyotrophic lateral sclerosis. *Brain*, 129, 1859-1871, 2006.
- [48] Hasina Y, Shigeki A, Osamu A, Yasuhiro N, Naoto H, Yoshitaka M, Masami G, Kuni O. Tract-specific analysis of white matter pathways in healthy subjects: a pilot study using diffusion tensor MRI. *Neuroradiology* 51:831-840, 2009.
- [49] Huang H, Zhang J, van Zijl P, Mori S. Analysis of noise effects on DTI-based tractography using the Brute-Force and Multi-ROI approach *Magnetic Resonance in Medicine*, 52:559-565, 2004.
- [50] Hattori T, Yuasa T, Aoki S, Sato R, Sawaura H, Mori T, Mizusawa H. Altered microstructure in corticospinal tract in idiopathic normal pressure hydrocephalus: comparison with Alzheimer Disease and Parkinson Disease with dementia *AJNR Am J Neuroradiol* 32:1681- 87, 2011.
- [51] <http://fsl.fmrib.ox.ac.uk/> FDT User Guide
- [52] Masutani Y, Aoki S, Abe O, Hayashi N, Otomo K. MR diffusion tensor imaging: recent advance and new techniques for diffusion tensor visualization. *Eur J Radiol.*, 46(1):53-66, 2003.
- [53] Fischl B. FreeSurfer. *NeuroImage* 62(2): 774-781, 2012.

- [54] Destrieux C, Fischl B, Dale A, Halgren E. Automatic parcellation of human cortical gyri and sulci using standard anatomical nomenclature. *NeuroImage* 53(1): 1-15, 2010.
- [55] Smith SM, Jenkinson M, Johansen-Berg H, Rueckert D, Nichols TE, Mackay CE, Watkins KE, Ciccarelli O, Cader MZ, Matthews PM, and Behrens TEJ. Tract-based spatial statistics: Voxelwise analysis of multi-subject diffusion data. *NeuroImage*, 31:1487-1505, 2006.
- [56] <http://fsl.fmrib.ox.ac.uk/fsl/fsl4.0/tbss/index>
- [57] Thottakaraa P, Lazara M, Johnsonc S, Alexandera A. Application of Brodmann's area templates for ROI selection in white matter tractography studies *NeuroImage* 29 868 -878, 2006.
- [58] Colby J, Soderbergc L, Lebelc C, Dinova I, Thompson P, Sowel E. Along-tract statistics allow for enhanced tractography analysis. *NeuroImage* Volume 59, Issue 4, Pages 3227-3242, 2012.
- [59] Lin F, Yu C, Jiang T, Li K, Li X, Qin W, Sun H, Chanc P. Quantitative analysis along the pyramidal tract by length-normalized parameterization based on diffusion tensor tractography: application to patients with relapsing neuromyelitis optica *NeuroImage* 33 154-160, 2006.
- [60] Reich DS, Smith SA, Jones CK, Zackowski KM, van Zijl PC, Calabresi PA, Mori S. Quantitative characterization of the corticospinal tract at 3T. *AJNR Am J Neuro-radiol.* 27(10):2168-78, 2006.
- [61] Oh JS, Kubicki M, Rosenberger G, Bouix S, Levitt JJ, McCarley RW, Westin CF, Shenton ME. Thalamo-frontal white matter alterations in chronic schizophrenia: a quantitative diffusion tractography study. *Hum Brain Mapp.*30(11):3812-25, 2009.
- [62] Johansen-Berg, Behrens T. Diffusion MRI. *Chapter 19* 434-436
- [63] Jones D. The Effect of gradient sampling schemes on measures derived from diffusion tensor MRI: a Monte Carlo study. *Magnetic Resonance in Medicine*, 51:807-815, 2004.

- [64] Bastin M, Armitage P, Marshall I. A theoretical study of the effect of experimental noise on the measurement of anisotropy in diffusion imaging. *Magnetic Resonance Imaging* Vol. 16, No. 7, pp. 773-785, 1998.